Diplomarbeit

Transport through quantum wires with surface disorder

ausgeführt am

Institut für Theoretische Physik
der Technischen Universität Wien

Institute for Theoretical Physics
Vienna University of Technology

unter der Anleitung von
O.Univ.-Prof. Dipl.-Phys. Dr.rer.nat. Joachim Burgdörfer
und
Univ.Ass. Dipl.-Ing. Dr.techn. Stefan Rotter

durch

Johannes Feist
Leitermayergasse 35/9
A-1180 Wien
johannes.feist@tuwien.ac.at

Contents

Chapter 1

Introduction

Nature and nature's laws lay hid in night;
God said "Let Newton be" and all was light.
Alexander Pope

It did not last: the devil, shouting "Ho,
Let Einstein be" restored the status quo.
John Collings Squire

The transport of particles and waves through a disordered medium is a long-standing problem which comprises countless applications in (micro-)electronics, optics and acoustics [1–5].

In a perfectly ordered medium, such as a semiconductor crystal without any defects at zero temperature, transport would also proceed perfectly. For example, a wire without disorder would show zero resistance. It is only the ubiquitous presence of disorder, such as imperfections and impurities in the crystal, or crystal vibrations (phonons), that leads to well known behavior such as Ohm's law for macroscopic wires. The presence of disorder thus governs the behavior of the transport coefficients of a material and leads to effects such as the metal-insulator transition, also known as the Anderson transition [6].

Ohm's law is valid for macroscopic conductors, where all relevant length scales are large enough that quantum effects do not play a role. However, the rapid advances in semiconductor manufacturing technology allow for ever smaller devices to be constructed, such that the quantum nature of the electrons starts to play a role [7–9]. The attention to disordered media has recently witnessed a revival due to new experimental possibilities to study the 'mesoscopic' regime where a classical-to-quantum crossover of transport gives rise to a whole new class of interesting phenomena, such as (weak) localization or universal conductance fluctuations. In this mesoscopic regime, the systems are still large enough to be able to ignore the atomic (microscopic) scale, but too small to be accurately represented in a classical (macroscopic) description.

In most investigations of transport through a disordered medium, the disorder is assumed to be static and present in the *bulk* of the material through which particles or waves are transported. This disorder can then be described by a disorder potential that the particles (waves) are subject to. The strength and distribution of this disorder potential determine, amongst other things, whether transport will be ballistic, diffusive, or even absent by way of localization [1–5, 7, 8].

For the transport of charged particles through systems with bulk disorder, the introduction of a magnetic field applied perpendicular to the disordered scattering region leads to the emergence of new phenomena such as the quantum Hall effect [7, 8, 10] and the doubling of the localization length ξ [11].

Further advances in semiconductor manufacturing and the accompanying reduction of system sizes lead, however, to an increased surface-to-volume ratio in mesoscopic devices, for which *surface roughness* can turn out to be the dominant source of disorder scattering. The properties of transport are then determined by scattering at the rough boundaries of the wire, while there is almost no scattering in the bulk, where transport can be assumed to be ballistic. While random matrix theory (RMT) [11] is successful in describing bulk disordered systems, its application to wires with surface disorder is not straightforward [12–17].

In this thesis, we study electronic transport through wires with surface disorder, where we concentrate in particular on the case of wires with *one-sided* surface disorder subject to a perpendicular magnetic field. This means that we restrict the disorder to one of the boundaries, while assuming the other side completely smooth and free of corrugation on an appropriate length scale. This special geometry introduces a new aspect into the description: The phase space of the system, which is chaotic in the case of bulk disorder, two-sided surface disorder (regardless of the magnetic field), and one-sided surface disorder without a magnetic field, transforms into a mixed phase space consisting of a regular island of "skipping" orbits and a chaotic sea surrounding this island [18]. Similar systems have been treated in the context of dynamical tunneling and quantum chaos [19–28].

Utilising the Modular Recursive Green's Function Method [29, 30], we are able to numerically simulate wires of sufficient length to observe the asymptotic behavior of transport, in particular localized behavior. In addition to the numerical simulation, we derive an analytical expression for the localization length by performing wave function matching without fit parameters that is found to agree with the observed results very well.

This thesis is organised as follows. First, we describe mesoscopic systems in more detail in chapter 2, including methods to calculate the conductance through such systems by employing scattering theory. We then utilise these considerations for the study of quantum wires, with the emphasis on the case of surface disorder, and especially one-sided surface disorder with a magnetic field. We present the Modular Recursive Green's Function Method used to calculate the scattering matrix of our systems in chapter 3. In chapter 4 we describe how we apply this method for

constructing long quantum wires with surface disorder by using an "exponentiation" algorithm.

We then present the numerical results of our calculations (chapter 5). We find that wires with two-sided surface disorder behave as predicted by random matrix theory (RMT). For wires with one-sided surface disorder (where RMT is not applicable) we show that we can perform a quantum-to-classical crossover that leads to exponentially diverging localization lengths. The numerical result for the localization length ξ is found to agree very well with the result from an analytical calculation utilising wave function matching. We then analyse the transmission probabilities of the single modes and argue that their behavior can be explained by tunneling between the regular island and the chaotic sea. In chapter 6, we show the analytical calculation of the localization length ξ.

Chapter 2

Mesoscopic structures

Electron transport through the bulk of a semiconductor is usually studied by means of the classical Boltzmann transport equation. This amounts to assuming that the relevant length and time scales of potential changes are slow compared to the electron wavelength and the temporal scale of the scattering process [7]. While these used to be perfectly valid assumptions for semiconductors at room temperature (in contrast to, e.g., superconductors, where quantum effects determine the transport properties), the continuous improvement of semiconductor fabrication techniques in the past decades requires an extension of this purely classical picture of transport. It is now possible to fabricate devices where the mean free path of electrons is of the order of $10\,\mu m$, with an inelastic (phase-breaking) mean free path that is even larger. At the same time it is easily possible to create structures with characteristic dimensions that are much smaller than these mean free paths.

Such structures are usually called *mesoscopic devices*, indicating that they are still large compared to the microscopic (atomic) scale, but small compared to the macroscopic scale at which the Boltzmann transport equation is valid. To describe transport on the mesoscopic scale therefore requires a theory that takes phase coherence into account. The method we use to achieve this is quantum mechanical *scattering theory*.

2.1 Scattering in mesoscopic structures

In correspondence to the common experimental situation of a two-dimensional electron gas at a heterojunction [7, 8], we model the system as a two-dimensional cavity to which two semi-infinite leads are attached, as shown in Fig. 2.1. Inside the cavity, the potential $V(\mathbf{r})$ can be arbitrary, while there are some constraints on the potential inside the leads: First, we assume hard-wall boundary conditions, i.e. an infinite potential outside the leads. Additionally, the potential is assumed to be separable at large distances away from the scattering region, so that incoming and

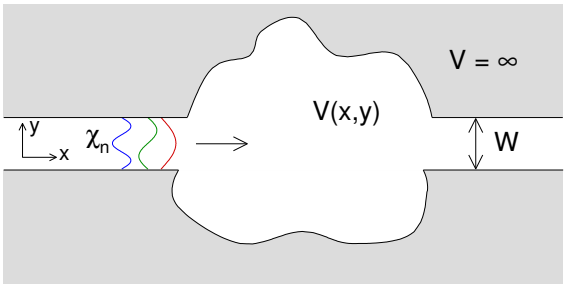

Figure 2.1: *A quantum cavity*

outgoing waves can be distinguished, turning this into a well defined scattering problem.

From this assumption follows that the wave function ϕ of an electron in the asymptotic regime is separable into a longitudinal and a transverse part, such that

$$\phi_n^{\pm}(\mathbf{r}) = \frac{1}{\sqrt{\theta_n}}\chi_n^{\pm}(y)\exp(\pm ik_{x,n}x). \tag{2.1}$$

The mode index n runs from 1 to N, with N the number of open modes (also called scattering channels) in the leads (we assume identical leads for simplicity). We define *open* modes as those having a real wave number $k_{x,n}$. These modes can propagate inside the leads and carry an electrical current. For $n > N$, $k_{x,n}$ contains an imaginary part. Such modes either decay exponentially away from the scattering region or are forbidden by the boundary conditions, as they would grow exponentially in the leads. These modes are thus negligible except near the disordered region. The normalization factors θ_n are obtained from a normalization condition that ensures that the open channels carry unit flux.

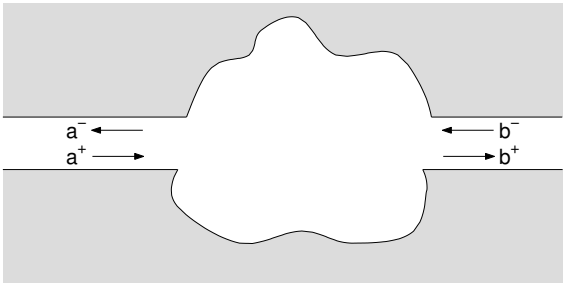

Figure 2.2: *A quantum cavity. The right-moving (left-moving) states in the leads are labelled by* a^+, b^+ (a^-, b^-).

Using these conventions, an incoming wave can be described in the basis of the lead states by (cf. Fig. 2.2)

$$c^{in} \equiv (a_1^+, a_2^+, \ldots, a_N^+, b_1^-, b_2^-, \ldots, b_N^-). \tag{2.2}$$

The N coefficients a_n^+ (b_n^-) expand the incoming wave in the left (right) lead of Fig. 2.1, such that the incoming wave is

$$\Psi^{in}(\mathbf{r}) = \begin{cases} \sum_{n=1}^{N} a_n^+ \phi_n^+(\mathbf{r}) & \text{for } \mathbf{r} \text{ in the left lead} \\ \sum_{n=1}^{N} b_n^- \phi_n^-(\mathbf{r}) & \text{for } \mathbf{r} \text{ in the right lead} \end{cases} \tag{2.3}$$

with the $\phi_n^\pm$ as defined in Eq. (2.1).

Similarly, the outgoing (reflected and transmitted) wave is described by

$$c^{out} \equiv (b_1^+, b_2^+, \ldots, b_N^+, a_1^-, a_2^-, \ldots, a_N^-). \tag{2.4}$$

With these ingredients we can define the scattering matrix S as the $2N \times 2N$ matrix that relates the two vectors c^{in} and c^{out} by

$$c^{out} = S c^{in} \tag{2.5}$$

The scattering matrix has the block structure

$$S = \begin{pmatrix} t & r' \\ r & t' \end{pmatrix} \tag{2.6}$$

with the transmission matrix t (t') for transport from left to right (right to left) and the reflection matrix r (r') for reflection in the left (right) lead. The $N \times N$ elements t_{nm} (r_{nm}) of the transmission (reflection) matrix are called transmission (reflection) *amplitudes* from incoming mode m to outgoing mode n. The transmission (reflection) *probabilities* are then given by

$$T_{nm} = |t_{nm}|^2 \qquad R_{nm} = |r_{nm}|^2 \tag{2.7}$$

$$T_m = \sum_{n=1}^{N} |t_{nm}|^2 \qquad R_m = \sum_{n=1}^{N} |r_{nm}|^2 , \tag{2.8}$$

where T_m (R_m) is the total transmission (reflection) probability of mode m.

Using the transmission amplitudes as defined above, we can write the scattering wave function in the two leads as

$$\Psi(\mathbf{r}) = \begin{cases} \phi_1^{L+}(x,y) + \sum_{m=1}^{N_L} r_{m1} \phi_m^{L-}(x,y) & \text{for } \mathbf{r} \text{ in the left lead,} \\ \sum_{m=1}^{N_R} t_{m1} \phi_m^{R+}(x,y) & \text{for } \mathbf{r} \text{ in the right lead,} \end{cases} \tag{2.9}$$

where we have assumed for notational simplicity that the incoming wave is coming from the left lead in the first mode, i.e. $c^{in} = (1, 0, \ldots, 0)$. The generalization to arbitrary c^{in} is straightforward.

Since we normalized our wavefunctions to unit flux, current conservation implies that the scattering matrix is unitary, i.e. $S^\dagger S = \mathbb{1}_{2N}$, where $\mathbb{1}_{2N}$ is the identity matrix of dimension $2N \times 2N$. From the unitarity of the scattering matrix follows, amongst other things,

$$T_m + R_m = 1, \tag{2.10}$$

i.e., the transmission and reflection probabilities of each mode have to add up to one, or simply put, the electron can not disappear.

2.1.1 Onsager-Casimir symmetry relations

In addition to unitarity, the scattering matrix has to fulfill the *Onsager-Casimir* symmetry relations [31–33], which follow from time-reversal symmetry. For non-vanishing magnetic field, this also demands reversal of the magnetic field. In our simple case of a structure with two leads, they are given by

$$t_{mn}(B) = t'_{nm}(-B) \tag{2.11a}$$
$$r_{mn}(B) = r_{nm}(-B) \tag{2.11b}$$
$$r'_{mn}(B) = r'_{nm}(-B) \tag{2.11c}$$

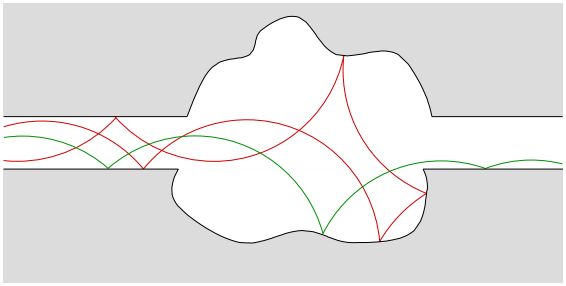

Figure 2.3: *A quantum cavity with classical trajectories to illustrate the Onsager-Casimir symmetry relations.*

These symmetry relations can be most easily understood by looking at classical trajectories. The green path sketched in Fig. 2.3 is one possible trajectory of an electron injected into the left lead if there is a magnetic field into the page. If the magnetic field switches sign (i.e. $B \to -B$) and we inject the electron from the right along the same path, it will retrace its trajectory exactly, but in the opposite direction. As the mode number m corresponds to the angle with which the electron

is injected, it is thus easy to conclude that the transmission from mode n in the left lead to mode m in the right lead with magnetic field B will be the same as the transmission from mode m in the right lead to mode n in the left lead with the opposite magnetic field $-B$. This explains Eq. (2.11a). The same argument holds true for the reflection, the only difference is that the electron enters the cavity from the same side as it leaves it. This explains Eq. (2.11b) for injection from the left and Eq. (2.11c) for injection from the right. The red path in Fig. 2.3 shows one possible trajectory for injection from the left and subsequent reflection. Reversal of the magnetic field again makes it possible to follow the exact same path in the opposite direction.

2.2 Conductance

Once we know the scattering matrix of our structure, we can calculate the conductance g in our 2-dimensional system, which is defined as the ratio of the current I and the voltage difference V across the system in the limit of vanishing voltage, $g = \lim_{V\to 0} I/V$. This limit ensures that we are in the regime of linear response.

The Landauer formula states that at zero temperature this limit results in the following relation for the conductance:

$$g = \frac{2e^2}{h}\mathrm{Tr}(t^\dagger t) = \frac{2e^2}{h}\sum_{m=1}^{N} T_m = \frac{2e^2}{h}\left(N - \sum_{m=1}^{N} R_m\right), \tag{2.12}$$

where t is the transmission matrix from the left lead to the right lead, as defined in Eq. (2.6). The prefactor $2e^2/h$ is the fundamental unit of conductance or *conductance quantum*, which includes a factor of 2 owing to the twofold spin degeneracy that arises because we neglect all spin interactions. We will always give the conductance in units of this fundamental conductance, such that $g = \mathrm{Tr}(t^\dagger t)$. Eq. (2.12) was first found in slightly different form by Landauer [34] for the case of a single open channel in the leads, and first written down in this form (generalized to the multi-channel case) by Fisher and Lee [35]. Its validity at arbitrary magnetic fields was shown by Baranger and Stone [36], where a generalization to non-zero temperatures was also introduced. As an aside, we note that the generalization of the Landauer formula to a system with an arbitrary number of leads is trivial, the reduction to the case of two leads was done here merely for notational simplicity.

The appeal of the Landauer formula (2.12) is that it directly connects the conductance, a measurable quantity, with the simple theoretical concept of the scattering matrix. At first sight, it might seem surprising that for a system without scattering (i.e. $S = \mathbb{1}$) the conductance is finite ($g = N$) – a fact that led to some controversy surrounding the Landauer formula. On closer inspection, it is found that this property follows from the assumptions made in deriving the formula. A

complete description can be found in chapter two of reference [8]. In short, the finite conductance for a "perfect" conductor stems from the fact that the leads are assumed to be connected to macroscopic contacts or *electron reservoirs*. Consequently, the minimum resistance $g_C^{-1} = 1/N$ of a conductor with N modes is called the "contact" resistance.

By combining the Onsager-Casimir relations (2.11) with the unitarity condition (2.10), we can derive an additional property for the conductance

$$N - \sum_{m,n} |r_{mn}(B)|^2 = N - \sum_{m,n} |r_{nm}(-B)|^2 \tag{2.13}$$

from which follows that

$$g(B) = g(-B). \tag{2.14}$$

We thus find that the conductance does not change if we reverse the magnetic field. Note that this only applies to the total conductance, *not* the transmission probabilities of the single modes.

It should be noted that the Landauer formula does not necessarily demand phase coherence throughout the sample, although we should use the formulation in terms of the transmission probabilities instead of the transmission amplitudes in such a case. In this thesis, transport is always assumed to be fully phase coherent, with all inelastic processes (necessary to achieve thermal equilibrium) taking place in the reservoirs (at chemical potential or Fermi energy E_F) to which the leads are connected.

The potential $V(\mathbf{r})$ inside the cavity leads to elastic scattering and thus determines the elastic mean free path l^e of the electron, where the mean free path is defined as the average distance an electron can travel without undergoing elastic scattering. Depending on the magnitude of l^e compared to some characteristic dimension L of the sample, we can distinguish between different transport regimes: As long as $L \gg l^e$, the electron is scattered (phase coherently!) many times inside the cavity, and thus transport can be thought of as a slow diffusion process. Contrary to this *diffusive* regime of transport, we enter the *quasi-ballistic* regime when the sample is much smaller than the mean free path of the electron, i.e. $L \ll l^e$. In that case, the electron propagates almost freely inside the cavity and the transport properties are determined by scattering at the boundaries of the cavity. Such a system is often called a quantum dot [37]. Note that the essential difference between the *quasi-ballistic* and the *diffusive* regime is the amount of scattering that the electron undergoes in the *bulk* of the cavity. If the disorder is strong enough and the system is sufficiently large ($L \gg \xi$), the conductance will decay exponentially with system size. This effect is called Anderson localization [6], and consequently, the system is then said to be in the *localized* regime, with localization length ξ. Depending on the dimensionality of the system, localization occurs only for large

enough disorder (three dimensions) or for any disorder strength (one dimension). For two dimensions, the conductance will always go to zero for large L, but not necessarily with an exponential decay [2, 11].

2.3 Quantum wires

We now apply the general considerations on transport through a phase coherent quantum system to the case of a wire. In particular, we will use the term *quantum wire* for a quantum dot where the aspect ratio of length L to width W is much greater than one ($L/W \gg 1$).

For the case of a one-dimensional chain with disorder (which corresponds to a wire with only one open mode), Anderson *et al.* [38, 39] found that the transmission decays exponentially as a function of the wire length (i.e. $g \propto \exp(-L/\xi)$) even for arbitrarily weak disorder. Quantum wires with disorder will therefore always enter the *localized* regime, with localization length ξ. For a 1D system, ξ is about the same as the mean free path l^e. The generalization of the theory of localization to the multi-mode case (i.e., a wire with bulk disorder and N open modes, sometimes called a quasi-1D system) shows that there is still localization, but the localization length increases by a factor of about N, i.e. $\xi \sim Nl^e$ ([11] and references therein). Since in the limit of large L essentially no transport takes place, the localized regime is often also referred to as the *insulating* regime.

The prediction that every wire shows localization once $L \sim Nl^e$ seems surprising at first. Does it mean that copper wires become insulators if they are made long enough? This obviously does not happen. The prediction is only valid if the system is phase coherent over scales as large as the localization length. For normal metal wires, Nl^e will be much larger than the phase coherence length (or inelastic mean free path), as N is very large. As soon as phase coherence is destroyed, there is no localization and the wire follows Ohm's law [8].

To extract the localization length from the numerical data for the phase-coherent systems studied in this thesis we employ the following relation [11, 38, 39],

$$\langle \ln g \rangle \propto -\frac{L}{\xi} \qquad L \gg \xi. \tag{2.15}$$

The localization length ξ enters as a fit parameter and the brackets $\langle \dots \rangle$ indicate that we average over different realizations of the disorder and/or a small range of energies (the two types of averaging are equal under the assumption of ergodicity). It is important to take the average of the logarithm of the conductance and *not* the logarithm of the average conductance here. The reason for this is that in the localized regime, the distribution of g is not self-averaging (which it is for shorter wire lengths) so that $\Delta g/\langle g \rangle$ actually diverges with increasing wire length. This makes $\langle g \rangle$ unusable for characterizing the system. As g is *log-normally* distributed,

the logarithm $\ln g$ of the conductance follows a Gaussian distribution in this regime (when $g \ll 1$), and its average is thus a valid quantity [38, 39].

For wires shorter than the localization length, but still longer than the elastic mean free path, the resistance increases linearly with the wire length, such that g is well described by Ohm's Law ($g \propto W/L$). In this *diffusive* regime, the wire behaves like a normal metal wire without phase coherence. More exactly, the following behavior is predicted [38–40]:

$$\left\langle \frac{1}{g} \right\rangle = \frac{1}{N} + \frac{L}{Nl^e} \qquad l^e \ll L \ll \xi \tag{2.16}$$

where the first term is the "contact" resistance $g_C^{-1} = 1/N$ mentioned above, while the second term is sometimes called the "actual" resistance g_A^{-1}, since it is the system-specific part of the resistance. For details we refer to chapter 2 of Ref. [8]. Note that the configuration average is taken over the inverse conductance, i.e. the resistance of the wire. Below, we will use the above relation to extract the elastic mean free path l^e from the data.

Historically, the research on electron transport through disordered wires was largely focused on wires with bulk disorder. The predictions stated above are well understood and follow from *random matrix theory* (RMT) [11, 41, 42]. This theory was originally developed by Wigner for the study of the statistics of energy levels in heavy nuclei in the 1950's (for a review see [43]). It was later discovered that it can be applied generally to systems that are classically *chaotic* and specifically to wires with bulk disorder. For example, Ericson fluctuations in nuclear cross-sections [44] correspond to universal conductance fluctuations in mesoscopic systems [11].

In the case of scattering problems, the scattering matrix is assumed to be randomly distributed, where the exact distribution depends on the symmetries of the problem. Starting with this approach, it is possible to derive the Dorokhov-Mello-Pereyra-Kumar equation ([11] and references therein), which describes the evolution of the distribution of transmission eigenvalues of a bulk disordered wire. The only system-specific information that enters into this equation is the symmetry class of the system. If there is no magnetic field, the motion of the electrons will obey time-reversal symmetry. On the other hand, inclusion of a magnetic field breaks this symmetry since the Lorentz force depends on the velocity and thus changes sign under time-reversal.

In the case of broken time reversal symmetry, the Dorokhov-Mello-Pereyra-Kumar equation can be solved analytically, so that the full distribution function of the eigenvalues of a bulk disordered wire in a magnetic field is known within the framework of random matrix theory.

2.4 Wires with surface disorder

The improvements in fabrication techniques of semiconductors in the last decades have led to structures with ever less defects. The less defects there are, the longer the mean free path in the semiconductor. If the mean free path is larger than any dimension of the system, the electrons are only scattered at the boundaries of the scattering region and the *quasi-ballistic* regime is entered. Evidently, if the surface of the wire was completely smooth, we would have the case of an ideal lead as described above and there would be no scattering at all. This has even been realized experimentally [45]. For wire walls which are not perfectly smooth, though, we have an entirely new class of systems, the *wires with surface disorder*. Such quantum wires have only recently been studied.

For a wire with surface disorder, we can not expect the predictions for bulk disorder to hold since the isotropy assumption made in deriving these predictions is violated. This assumption states that the transmission probability is, on average, independent of the incoming or outgoing mode, such that the magnitude of all elements of the transmission matrix is the same. The isotropy assumption works very well when the main sources of scattering are bulk defects, but breaks down in the case of surface disorder. This can be understood by considering the correspondence of quantum modes in the wire to classical trajectories, as shown in Fig. 2.4.

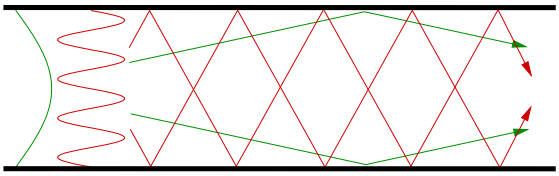

Figure 2.4: *Quantum modes and corresponding classical trajectories. The first mode (green) corresponds to injection at a low angle, while a higher mode (red) corresponds to injection at a higher angle.*

The higher modes have high transverse momentum and thus correspond to electrons entering the wires at steep angles, while the low modes correspond to trajectories with shallow angles. Higher modes visit the disordered surface region more often and are thus more strongly affected by the disorder, introducing a mode dependence for the disorder. This mode dependence of scattering at the surfaces necessitates that all the predictions previously given have to be reexamined to see whether they can be applied for wires with surface disorder.

There are a number of numerical studies of transport through wires with surface disorder. It should be noted that waveguides for optical waves, acoustic waves, and microwaves behave similarly to electronic (quantum mechanical) wires with respect to their transport properties. For example, in two dimensions, the Helmholtz

equation for the electric field component of transverse magnetic modes in a microwave cavity is equivalent to the Schrödinger equation with hard wall boundary conditions. Consequently, some of the literature discusses optical waveguides (e.g. [12, 14, 17, 46, 47]) and some electronic structures (e.q. [15, 16, 48]). Although there is sizable number of papers studying wires with surface disorder, no complete theoretical model to describe and predict their behavior seems to exist. Consequently, the existing (numerical and experimental) results are mostly compared to the predictions for bulk disorder. The resulting discrepancies are typically explained by the mode-dependent behavior of surface scattering.

One of the main results of these studies is that generally no well-defined diffusive regime exists for wires with surface disorder, while a quasi-ballistic (localized) regime can still be identified for very short (long) wire lengths. Between these two extremes, there is an intermediate regime where the T_{nm} all behave differently, preventing a classification in terms of a global parameter regime. Still, for each incoming mode one can specify whether it is in the ballistic, diffusive, or localized regime [12, 14].

When the various parameters of the system are chosen in such a way that intermode mixing is strong, the behavior of the system is again independent of the incoming mode. In that case, a global diffusive regime can still emerge.

2.4.1 One-sided surface disorder with magnetic field

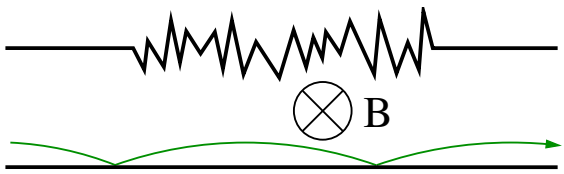

Figure 2.5: *A wire with one-sided surface disorder in a magnetic field and a "skipping" trajectory (green).*

If surface disorder is only present on one side of the wire, the other being perfectly flat, and we add a magnetic field, as in Fig. 2.5, we have the special case of the *wire with one-sided surface disorder in a magnetic field*. In the classical description of such a wire, there are regular "skipping" orbits that never reach the disorder (shown in red in Fig. 2.5). Because of these regular trajectories, the system is not completely chaotic, but possesses a mixed phase space [18].

The phase space consists of a regular island, inhabited by the skipping orbits, and a chaotic sea, inhabited by the trajectories that are scattered by the disorder. Note that this depends crucially on both the restriction of the disorder to one side

and the magnetic field. If we add disorder on both sides or turn off the magnetic field, no skipping orbits can exist and the system is completely chaotic (under the condition that it is long enough that there are almost no direct paths).

It is only the wire with one-sided surface disorder in a magnetic field that has a large regular island. This fundamental difference to the quantum wire with bulk disorder or two-sided surface disorder suggests that random matrix theory should not be applicable to a wire with one-sided surface disorder in a magnetic field. Nevertheless, García-Martín *et al.* [49] found that for low energies and magnetic fields some predictions from RMT still hold.

Even though there are classical states that do not suffer scattering at the rough surface, we are *not* in the regime of the *quantum Hall effect* [7,8,10]. In the quantum Hall regime the magnetic field is strong enough that the propagating states on the two sides of the lead decouple completely. This happens when the cyclotron radius is significantly smaller than the width of the wire. There are then two possible types of trajectory: Edge states at the boundaries of the lead that propagate in opposite directions for the two sides of the lead and states in the middle of the lead that never touch any boundary, but instead perform circular orbits in the absence of a random potential in the interior. These states do not carry any flux. In this regime of very strong magnetic field (small cyclotron radius), there is almost no scattering from the flux-carrying modes on one side of the lead to the modes carrying flux in the other direction on the other side. This even applies if there is bulk disorder.

In contrast, the absence of scattering in a wire with one-sided surface disorder for the skipping modes depends crucially on the specific geometry. As soon as disorder is introduced on both sides of the wire, the skipping orbits are scattered and the regular island disappears.

Chapter 3

Method

We simulate transport through a ballistic cavity with surface disorder as described above (section 2.1). Our system is characterized by hard-wall boundary conditions and an electrostatic potential which we set to zero in the whole system (lead-cavity-lead). We include a constant magnetic field, oriented perpendicular to the scattering plane. In the two semi-infinite leads of width W, we impose scattering boundary conditions at asymptotic distances, i.e. far away from the disordered region. The transverse part $\chi_n^{\pm}(y)$ of the wave function

$$\phi_n^{\pm}(\mathbf{r}) = \frac{1}{\sqrt{\theta_n}} \chi_n^{\pm}(y) \exp(\pm i k_{x,n} x) \tag{3.1}$$

is sinusoidal in the field-free case, and a combination of Kummer functions in the presence of the magnetic field [50, 51]. Atomic units ($\hbar = |e| = m_{\text{eff}} = 1$) will be used from now on, unless explicitly stated otherwise. We construct our system by decomposing it into modules and employing the *Modular Recursive Green's Function Method* (MRGM) developed by S. Rotter [29, 30]. This method is used to calculate the Green's function of the system on a discretized grid. The scattering matrix S can then be extracted by projecting the modes in the leads onto the Green's function. We do not include any phase-breaking mechanism in our method, i.e. we assume phase coherence throughout the sample.

3.1 Brief review of the MRGM[1]

We start by briefly reviewing the MRGM for the case of no magnetic field. Starting point is the observation that a large class of geometries with non-separable boundaries can be decomposed into separable two-dimensional substructures, referred to in the following as modules. For each of these modules the discretization of the

[1] Parts of this section go back to [30]

corresponding tight-binding (tb) Hamiltonian can be performed on a symmetry-adapted grid. The grid for each module is chosen such that the eigenfunctions of the tb Hamiltonian

$$\hat{H}^{\mathrm{tb}} = \sum_i \varepsilon_i \,|\, i \,\rangle\langle\, i \,|\, + \sum_{i,j} V_{i,j} \,|\, i \,\rangle\langle\, j \,|\, \tag{3.2}$$

separate into two generalized coordinates. In the wires studied in this thesis, we only use rectangular modules, for which the two coordinates are just the Cartesian x and y. $\hat{H}^{\mathrm{tb}}$ contains hopping potentials $V_{i,j}$ for nearest-neighbor coupling and site energies ε_i. Both quantities are chosen such that the Schrödinger equation, $\hat{H}^{\mathrm{tb}}|\phi_m\rangle = E_m|\phi_m\rangle$, converges towards the continuum Schrödinger equation in the limit of high grid point density. For the Cartesian coordinate system we have at $B = 0$ [29]

$$V^x_{i,i\pm1} = \frac{-1}{2\Delta x^2}, \qquad V^y_{j,j\pm1} = \frac{-1}{2\Delta y^2}, \qquad \varepsilon_i = \frac{1}{\Delta x^2} + \frac{1}{\Delta y^2}. \tag{3.3}$$

For separable energy eigenfunctions of the general form $|E_m\rangle = |E_k\rangle \otimes |E_{k,n}\rangle$ the spectral representation of the retarded $(+)$ and advanced $(-)$ Green's function $G^{\pm}(\mathbf{r}, \mathbf{r}', B, E_F)$ of the module is simply given by

$$G^{\pm}(\mathbf{r}, \mathbf{r}', B, E_F) = \sum_k \langle x|E_k\rangle\langle E_k|x'\rangle \sum_n \frac{\langle y|E_{kn}\rangle\langle E_{kn}|y'\rangle}{E_F \pm i\epsilon - E_{kn}}. \tag{3.4}$$

The indices (k, n) represent the quantum numbers of the separable eigenfunctions $|E_k\rangle$, $|E_{k,m}\rangle$ associated with the degrees of freedom x and y respectively.

The Green's functions of the separate modules are joined by solving a matrix Dyson equation,

$$G = G^0 + G^0 \bar{V} G, \tag{3.5}$$

where G^0 and G denote Green's functions of the disconnected and the connected modules, respectively. The matrix $\bar{V}$ denotes the hopping potential V multiplied by the size of the unit cell $\bar{V} = V\Delta_R$, which in a Cartesian grid is $\Delta_R = \Delta x \Delta y$. The complete scattering structure can thus be assembled from the individual modules (much like a jigsaw puzzle). The number of necessary recursions [i.e. solutions of (3.5)] is (approximately) equal to the number of modules.

Once the Green's function G^+ for the combination of all modules is assembled, the transmission amplitudes t_{nm} from entrance lead mode m into exit lead mode n can be calculated by projecting G^+ onto the transverse wavefunctions in the leads $\chi_n(y_i)$,

$$t_{nm}(E_F) = -i\sqrt{k_{x_2,n} k_{x_1,m}} \int_{-W/2}^{W/2} dy_2 \int_{-W/2}^{W/2} dy_1 \; \chi_n^*(y_2)\, G^+(y_2, y_1, E_F)\, \chi_m(y_1)\,. \tag{3.6}$$

where $k_{x_i,n}$ denotes the corresponding longitudinal wave numbers, which are given by

$$k_{x_i,n} = \sqrt{k_F^2 - \left(\frac{n\pi}{W}\right)^2} \tag{3.7}$$

Note that (3.6) and (3.7) are only valid for $B = 0$. The number of open modes can be easily calculated from Eq. (3.7). With the following expression

$$k_F = \eta \frac{\pi}{W}, \tag{3.8}$$

the number of open modes N in the leads is simply given by $[\eta]$ ($[\ldots]$ denoting the integer part) provided that no magnetic field is present.

3.2 Inclusion of the magnetic field

Incorporation of the magnetic field into the MRGM poses a number of complications. The solutions of these difficulties will be presented in this section. At the core of the problem is the preservation of separability of the Schrödinger equation. The usage of gauge transformations as well as of Dyson equations for decomposing non-separable structures into separable substructures plays a key role in accomplishing this goal. We use a magnetic field in the negative z-direction, $\mathbf{B} = (0, 0, -B)$, which enters the tb Hamiltonian (3.2) by means of a Peierls phase factor [7, 52],

$$V_{\mathbf{r},\mathbf{r}'} \longrightarrow V_{\mathbf{r},\mathbf{r}'} \cdot \exp\left[(i/c)\int_{\mathbf{r}}^{\mathbf{r}'} \mathbf{A}(\mathbf{r})\mathbf{dr}\right], \tag{3.9}$$

with which the field-free hopping potential $V_{\mathbf{r},\mathbf{r}'}$ is multiplied. The vector potential $\mathbf{A}(\mathbf{r})$ satisfies $\nabla \times \mathbf{A}(\mathbf{r}) = \mathbf{B}$. The Peierls phase will, of course, in most cases destroy the separability of the eigenfunctions of $\hat{H}^{\mathrm{tb}}$. The difficulties can be, in part, circumvented by exploiting the gauge freedom of the vector potential, i.e.,

$$\mathbf{A} \rightarrow \mathbf{A}' = \mathbf{A} + \nabla\lambda\,, \tag{3.10}$$

where $\lambda(\mathbf{r})$ is a scalar function. By an appropriate choice of λ the wavefunction remains separable on a given symmetry adapted grid. Specifically, to preserve separability we employ the Landau gauge for a Cartesian grid

$$\mathbf{A} = By\,\hat{\mathbf{x}}, \tag{3.11}$$

A major complication results from the fact that, in the presence of the magnetic field, the separability on an unrestricted grid of a given symmetry does not imply the separability in the presence of boundary conditions of the same symmetry. We

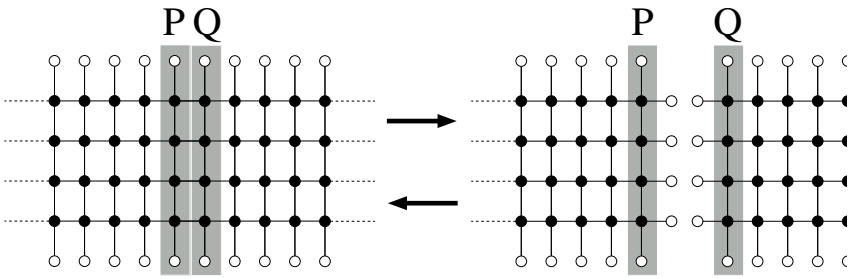

Figure 3.1: *Joining and disconnecting of modules by application of a Dyson equation: two semi-infinite leads. The hard wall boundary conditions at the sites on the border of the modules are represented by empty circles (accessible space by full circles). The gray shaded areas P and Q are those grid slices at which the Green's functions are evaluated (see text).*

illustrate this problem with the help of one typical example, the *semi-infinite* quantum wire with lead width W (Fig. 3.1). We impose hard-wall boundary conditions $\phi(x, y = \pm W/2) = 0$ and consider first the *infinite* quantum wire along the x direction. Because of the Cartesian boundary conditions, the symmetry adapted gauge is the Landau gauge $\mathbf{A} = By\,\hat{\mathbf{x}}$. Consider, for notational simplicity, the Schrödinger equation in the continuum limit,

$$\begin{aligned} H\phi(y,x) &= \frac{1}{2}\left(\mathbf{p} + \frac{1}{c}\mathbf{A}\right)^2 \phi(x,y) \\ &= \frac{1}{2}\left(-\frac{\partial^2}{\partial x^2} - \frac{\partial^2}{\partial y^2} - \frac{i2B}{c} y \frac{\partial}{\partial x} + \frac{B^2 y^2}{c^2}\right)\phi(x,y) = E_F \phi(x,y). \end{aligned} \tag{3.12}$$

Since the longitudinal momentum $p_x = -i\partial/\partial x$ commutes with H, the separability of the wavefunction persists in the presence of the magnetic field: $\phi(x, y) = f_k(x)\chi(y)$ with $f_k(x) = e^{ikx}$. If, however, one introduces an additional Cartesian boundary condition along the y-axis [i.e. $\phi(x = 0, y) = 0$ for a semi-infinite lead] the situation changes. In the absence of the magnetic field, $B = 0$, the linear term in p_x vanishes and thus the choice $f(x) = \sin(kx)$ [i.e. a linear combination of $f_{\pm k}(x)$] satisfies the boundary condition and preserves the separability, even though p_x is no longer conserved in the semi-infinite lead. However, for $B \neq 0$ and the same boundary condition $\phi(x = 0, y) = 0$, the term linear in B and p_x destroys the separability. The wavefunction takes now the general form

$$\phi(x,y) = \sum_m e^{ik_m x} \sum_n c_{mn}\chi_{mn}(y). \tag{3.13}$$

The breakdown of separability by the introduction of an additional boundary condition indicates that the Green's function of confined modules will be more

complex than for extended systems for the same symmetry adapted grid and the same gauge. Therefore, the program of the modular method of building up extended complex structures by "welding together" smaller modules of higher symmetry will be executed in reverse: non-separable confined modules will be generated by "cutting in pieces" larger separable modules. Confining boundary conditions will be introduced rather than removed by the matrix Dyson equation. In the example above, the *semi-infinite* quantum wire is generated by cutting the *infinite* wire at the line $x = 0$, thereby imposing the additional boundary condition. Just as connecting modules, so is disconnecting a given module equivalent to the solution of a matrix Dyson equation,

$$G^E = G^C + G^C \bar{V} G^E. \tag{3.14}$$

In this context G^E (G^C) is the Green's function of the extended (confined) module and $\bar{V}$ is the hopping potential that connects the modules. Solving (3.14) *in reversed mode* (i.e. for G^C rather than for G^E) amounts to dissecting the larger module.

Provided that the Green's functions of all the necessary modules are available, we have to link them with each other to assemble the entire scattering geometry. However, in the presence of a magnetic field we have to take into account that the different modules will be calculated in different gauges. Joining different modules requires, therefore, in general a gauge transformation. For the Green's function on the grid $G(\mathbf{r}_i, \mathbf{r}'_j)$ this transformation is simplified by the fact that the matrix of gauge transformations

$$[\Lambda(\mathbf{r}_j)]_{jk} = \exp\left[-i\lambda(\mathbf{r}_j)/c\right] \delta_{jk} \tag{3.15}$$

is diagonal in the grid representation. Correspondingly, the transformation of both the hopping potential $\bar{V}$ and the Green's function is local, i.e.

$$\bar{V}(\mathbf{r}_i, \mathbf{r}'_j) \to \bar{V}'(\mathbf{r}_i, \mathbf{r}'_j) = \Lambda(\mathbf{r}_i)\, \bar{V}(\mathbf{r}_i, \mathbf{r}'_j) \Lambda^*(\mathbf{r}'_j) \tag{3.16a}$$

$$G(\mathbf{r}_i, \mathbf{r}'_j) \to G'(\mathbf{r}_i, \mathbf{r}'_j) = \Lambda(\mathbf{r}_i)\, G(\mathbf{r}_i, \mathbf{r}'_j) \Lambda^*(\mathbf{r}'_j)\,. \tag{3.16b}$$

It is thus not necessary to transform gauges of different modules to one global gauge. Instead, it is sufficient to perform a local gauge transformation at the points of the junctions $\{\mathbf{r}_i\}$, such that the gauges of the two modules to be joined agree *at these points*.

Finally, in order to extract the S-matrix, i.e. the amplitudes t_{nm} and r_{nm}, matrix elements of the current operator must be of gauge-invariant form. This requirement can be fulfilled by employing a double-sided gradient operator which is defined as [36]

$$f \overleftrightarrow{\mathbf{D}} g = f(\mathbf{x}) \mathbf{D} g(\mathbf{x}) - g(\mathbf{x}) \mathbf{D}^* f(\mathbf{x}) = -g \overleftrightarrow{\mathbf{D}} f \quad \text{with} \quad \mathbf{D} = \nabla - \frac{i}{c} \mathbf{A}(\mathbf{x})\,. \tag{3.17}$$

With its help the transmission amplitudes can be evaluated as [36, 53–56]

$$t_{nm}(E_F, B) = -\frac{i}{4\sqrt{\theta_n \theta_m}} \int_{-W/2}^{W/2} dy_2 \int_{-W/2}^{W/2} dy_1' \, \chi_n^*(y_2) e^{-ik_n x_2} \, (\overleftrightarrow{\mathbf{D}} \cdot \hat{\mathbf{x}}_2)^* \\ G^+(\mathbf{x}_2, \mathbf{x}_1', E_F, B) \, (\overleftrightarrow{\mathbf{D}}' \cdot \hat{\mathbf{x}}_1') \chi_m(y_1') e^{ik_m x_1'} \, . \tag{3.18}$$

The unit vectors $\hat{\mathbf{x}}_n$ are assumed to be pointing in outward direction of the n-th lead and θ_m denotes the outgoing particle flux carried by $\chi_n(y_1')e^{ik_n x_1'}$ through the lead cross section.

Determination of transverse states $\chi_m(y_i)$ and of the corresponding longitudinal momentum k_m as well as the normalization factors θ_m will be discussed below. For the reflection amplitudes r_{nm}, a relation similar to (3.18) holds [36]. From t_{nm} and r_{nm} the conductance can be calculated by means of the Landauer formula [Eq. (2.12)].

3.3 Calculation of modules

This section is dedicated to the evaluation of the Green's functions for those modules which we need to assemble a wire with surface disorder: the semi-infinite leads and the rectangle. For these modules Eq. (3.4) is not applicable. This is due to the non-separability for confined geometries as discussed above. Moreover the spectrum in open structures like the semi-infinite lead is continuous rather than discrete. Unlike in the field-free case [57], the resulting integrals cannot be calculated analytically. However, both problems can be overcome by applying the matrix Dyson equation in a non-standard way.

3.3.1 Rectangular module

As illustrated above for the semi-infinite wave guide, the Dirichlet boundary condition for the confined structure of a rectangle with magnetic field is not separable, no matter which gauge is chosen. The separability can however be restored by imposing periodic boundary conditions on two opposing sides of the rectangle. Topologically, this corresponds to folding the rectangle to the surface of a cylinder (Fig. 3.2). In this case we connect the first (P) and the last (Q) transverse grid slice of a rectangular grid by a hopping potential $|V_{PQ}^x| = |V_{QP}^x| = \frac{-1}{2\Delta x^2}$. The Green's function of this "cylinder surface" (cs) will be denoted by G^{cs} in the following. The calculation of the rectangle Green's function G^{r} will be obtained out of G^{cs} by a Dyson equation used here in "reversed" mode, i.e. for *disconnecting* tb grids. This method for calculating the rectangular module may seem like a detour, but it is numerically more efficient than a strip-by-strip recursion. For completeness we mention that an alternative way to calculate G^{r} was proposed in Ref. [58].

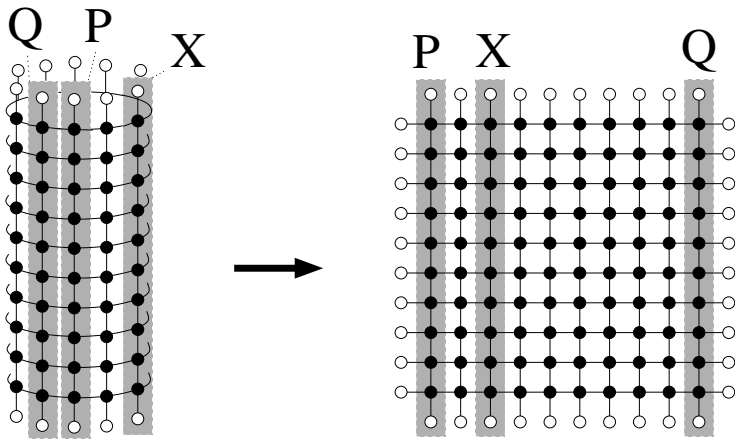

Figure 3.2: *Applying a Dyson equation in "reversed mode" to construct Green's functions for a rectangle out of a cylinder surface. The periodic boundary conditions are transformed into hard wall boundary conditions. The gray shaded areas P, Q and X are those grid slices at which the Green's functions are evaluated (see text).*

The Green's function for the cylinder surface G^{cs} can be constructed from separable eigenfunctions, $|E_m\rangle = |E_k^x\rangle \otimes |E_{kn}^y\rangle$, according to Eq. (3.4). Solving the tight-binding Schrödinger equation for the cylinder surface, we obtain for the longitudinal eigenstates $\langle x_j|E_k^x\rangle = (N_x \Delta x)^{-1/2} \exp(i2\pi kj/N_x)$, which results in a tridiagonal, symmetric matrix-eigenproblem of size $N_y \times N_y$ for the transverse modes [59],

$$\begin{aligned} E_{kn}\langle y_l|E_{kn}^y\rangle = \frac{-1}{\Delta x^2}\left[\cos\left(\frac{2\pi k}{N_x} + \frac{B}{c} y_l \Delta x\right) - 1\right] \times \langle y_l|E_{kn}^y\rangle \\ -\frac{1}{2\Delta y^2}\big(\langle y_{l-1}|E_{kn}^y\rangle - 2\langle y_l|E_{kn}^y\rangle + \langle y_{l+1}|E_{kn}^y\rangle\big) \end{aligned} \tag{3.19}$$

By "cutting the cylinder surface open" along a line of constant x, we obtain from G^{cs} the desired Green's function G^{r} for the rectangle (Fig. 3.2). We demonstrate this for the rectangle Green's function G_{PX}^{r} from the first transverse slice P to any other slice X. To determine G_{PX}^{r} we solve the following system of Dyson equations,

$$G_{PX}^{\mathrm{r}} = G_{PX}^{\mathrm{cs}} - G_{PQ}^{\mathrm{r}} \bar{V}_{QP} G_{PX}^{\mathrm{cs}} - G_{PP}^{\mathrm{r}} \bar{V}_{PQ} G_{QX}^{\mathrm{cs}} \tag{3.20}$$

$$G_{PQ}^{\mathrm{cs}} = G_{PQ}^{\mathrm{r}} + G_{PQ}^{\mathrm{r}} \bar{V}_{QP} G_{PQ}^{\mathrm{cs}} + G_{PP}^{\mathrm{r}} \bar{V}_{PQ} G_{QQ}^{\mathrm{cs}} \tag{3.21}$$

$$G_{PP}^{\mathrm{cs}} = G_{PP}^{\mathrm{r}} + G_{PQ}^{\mathrm{r}} \bar{V}_{QP} G_{PP}^{\mathrm{cs}} + G_{PP}^{\mathrm{r}} \bar{V}_{PQ} G_{QP}^{\mathrm{cs}}\,, \tag{3.22}$$

where the first line is the "reversed" Dyson equation. The three unknowns in the above equations are the Green's functions connecting the slices $(P, X), (P, Q)$ and (P, P), $G_{PX}^{\mathrm{r}}, G_{PQ}^{\mathrm{r}}, G_{PP}^{\mathrm{r}}$. By solving these three equations, the unknowns can be uniquely determined.

3.3.2 Semi-infinite lead

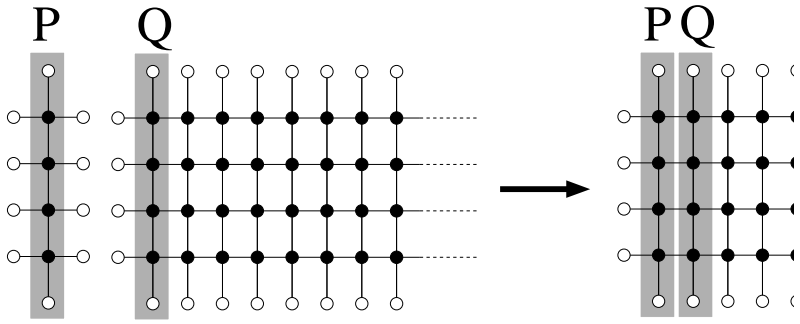

Figure 3.3: *Applying a Dyson equation to construct Green's functions for a semi-infinite lead out of "modules". Joining a transverse slice with a semi-infinite lead schematically leaves the Green's function of the lead invariant [for details see Ref. [29]]. Notation as in Figs. 3.1 and 3.2.*

Because of its continuous spectrum, the Green's function for the semi-infinite lead poses an additional challenge beyond that of the non-separability of the wavefunction discussed above. We therefore apply one further "trick" to bypass this problem. Our approach is based on the observation that adding a slice to a semi-infinite quantum wire leaves this wire (up to irrelevant phases) invariant (see Fig. 3.3). We assume a semi-infinite lead with $x \in [\Delta x, \infty)$ and hard-wall boundary conditions at $x = \Delta x$ and $y = \pm W/2$. To this object we add a slice consisting of just one transverse chain of tb grid points which we place at $x = 0$. The system of Green's functions for the propagation from the transverse chain at $x = 0$ (P) back to itself (P) or to the first transverse slice of the semi-infinite lead (Q) at Δx reads

$$G_{PP} = G^0_{PP} + G^0_{PP}\bar{V}_{PQ}G_{QP}, \tag{3.23a}$$
$$G_{QP} = G^0_{QQ}\bar{V}_{QP}G_{PP}. \tag{3.23b}$$

Each multiplication involves a matrix product with a dimension equal to the number of transverse grid points. The key point is now that the system of Eqs. (3.23) can be closed through the invariance condition (cf. Fig. 3.3) for the semi-infinite lead, i.e. $G_{PP} = G^0_{QQ}$. In Landau gauge $\mathbf{A} = (-By, 0, 0)$ the latter relation does not involve additional gauge phases since these are already contained in the hopping matrix element. We additionally note that an equivalent point of departure for the derivation of G_{PP} is the Bloch condition for states in the lead [53–56].

Setting $Z = G_{PP}\bar{V}_{QP}$ and using the hermiticity condition $\bar{V}_{QP} = \bar{V}^*_{PQ} \equiv \bar{V}^*$, Eqs. (3.23a,3.23b) can be converted to a quadratic matrix equation

$$ZZ - \bar{V}^{-1}(G^0_{PP})^{-1}Z + \bar{V}^{-1}\bar{V}^* = 0\,. \tag{3.24}$$

Solvents Z of a quadratic matrix equation $Q(Z) = 0$ can be constructed from the eigenpairs (β_i, χ_i) of the corresponding quadratic eigenvalue equation $Q(\beta_i)\chi_i = 0$, $i \in [1, \ldots, 2N]$ in the diagonal form [60],

$$Z = MBM^{-1} \quad \text{with} \quad M = [\chi_1, \ldots, \chi_N],\ B = \mathrm{diag}(\beta_i). \tag{3.25}$$

The quadratic eigenvalue equation is equivalent to a generalized eigenvalue problem $A\tilde{\chi} = \beta C\tilde{\chi}$ of twice the original dimension [59]. Its $2N$ dimensional eigenvectors $\tilde{\chi} = (\chi, \beta\chi)$ are solutions of the symmetric eigenproblem

$$\begin{pmatrix} -\bar{V}^* & 0 \\ 0 & \bar{V} \end{pmatrix} \begin{pmatrix} \chi \\ \beta\chi \end{pmatrix} = \beta \begin{pmatrix} -(G^0_{PP})^{-1} & \bar{V} \\ \bar{V} & 0 \end{pmatrix} \begin{pmatrix} \chi \\ \beta\chi \end{pmatrix}, \tag{3.26}$$

where $(G^0_{PP})^{-1} = E_F - \hat{H}^{\mathrm{tb}}_{\mathrm{1D}}$ and $\hat{H}^{\mathrm{tb}}_{\mathrm{1D}}$ is the Hamiltonian of the one-dimensional transverse tb strip at $x = 0$. The Fermi energy E_F and the magnetic field B enter (3.26) as independent parameters at which the eigenstates $\tilde{\chi}_m$ and eigenvalues β_m are evaluated. The longitudinal momenta of the lead states $\phi_m(x, y) = \chi_m(y)e^{ik_m x}/\sqrt{\theta_m}$ are related to the eigenvalues by the relation $\beta = \exp(ik\Delta x)$. The orthonormalization and the completeness relations of the $2N$ eigenvectors $\tilde{\chi}_m$ can be formulated in terms of matrix relations, for the generalized eigenproblem,

$$\frac{1}{\sqrt{\theta_m\theta_n}}\tilde{\chi}^T_m C\tilde{\chi}_n = 2i\frac{k_m}{|k_m|}\delta_{mn} \quad \text{and} \quad \sum_m^{2N} \frac{\tilde{\chi}_m\tilde{\chi}^T_m}{\theta_m} = 2i\frac{k_m}{|k_m|}C^{-1}. \tag{3.27}$$

With this specific choice of normalization the norm factors θ_m are determined such that every propagating state carries unit flux. We note parenthetically that the quadratic eigenvalue equation could also be applied to the semi-infinite lead at zero B field. However, in that case, the Green's function for quantum wires can be calculated analytically [29, 57] by complex contour integration.

Chapter 4

Quantum wires with surface disorder

Using the MRGM described in chapter 3, we construct a wire with surface disorder by modeling the disordered region as a series of rectangular slices (or modules), to which perfect semi-infinite leads are attached on both sides (see Fig. 4.1). Each of the slices can be described by three parameters: Its width l, which we choose to be the same for all the slices, and the vertical positions y_l and y_u of the lower and upper boundary, respectively. These are chosen to fall into the ranges

$$y_l \in \left[-\frac{\delta_l}{2}, \frac{\delta_l}{2}\right] \tag{4.1}$$

$$y_u \in \left[W - \frac{\delta_u}{2}, W + \frac{\delta_u}{2}\right], \tag{4.2}$$

such that the average width of the wire is given by the lead width W. δ_l and δ_u control the variations of the boundary positions, and thus govern the strength of the disorder. To describe wires with one-sided disorder, δ_l is simply set to zero, which leads to a flat lower boundary, as shown in Fig. 4.2. The height of each module is given by $y_u - y_l$. We choose the module heights to be uniformly distributed between $W-(\delta_l+\delta_u)/2$ and $W+(\delta_l+\delta_u)/2$. This enables us to calculate a set of rectangular modules and use them by shifting their positions up and down randomly within the bounds given by δ_l and δ_u.

We proceed as follows: The Green's functions of N_m rectangular modules with differing heights h_i are calculated, with the heights given by

$$h_i = W - \frac{\delta_u + \delta_l}{2} + \frac{i-1}{N_m - 1}(\delta_u + \delta_l) \qquad i \in [1, N_m]. \tag{4.3}$$

In this way we get N_m modules with equidistantly spaced heights spanning the

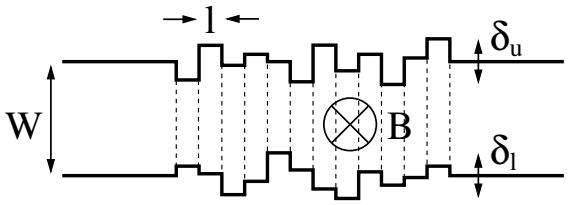

Figure 4.1: *Quantum wire with two-sided surface disorder (TSD)*

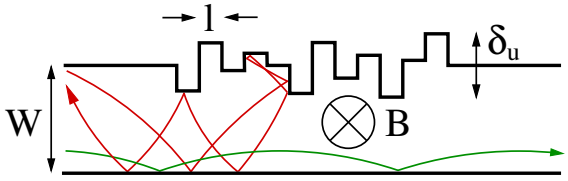

Figure 4.2: *Quantum wire with one-sided surface disorder (OSD)*

range from

$$h_1 = W - \frac{\delta_u + \delta_l}{2} \tag{4.4}$$

to

$$h_{N_m} = W + \frac{\delta_u + \delta_l}{2}. \tag{4.5}$$

We then connect these N_m modules in a random sequence to form a wire. The exact way in which this is done depends on which of the two algorithms we developed for this purpose is used.

4.1 Algorithms

To be able to cover a wide range of possible systems, we developed two algorithms to simulate surface disordered wires, which we term *single module* method and *supermodule* method, respectively. The former is better suited for short lengths of the disordered region and was thus mainly employed for the cases with two-sided surface disorder, were the localization lengths are only moderately large. The latter algorithm allows to calculate very long wires and was applied to wires with one-sided surface disorder, where the localization length ξ can become prohibitively large for the single module method.

4.1.1 Single module method

Within the framework of the *single module* method we calculate the Green's function for a quantum wire by connecting modules one at a time. Each of the modules is chosen randomly out of the N_m existing modules, with equal probability for each module. In the case of two-sided surface disorder, the module is randomly shifted up or down within the bounds given by δ_l and δ_u before being connected to the wire.

After having connected a few modules (typically between 2 and 10, but this can be chosen freely), two leads are connected to the system (while keeping the Green's function for the cavity without leads in the computer memory) and the scattering matrix for the completed system is calculated. This procedure of connecting a few modules to the scattering region and then calculating the scattering matrix is repeated until the desired length is reached. The time needed to calculate long wires increases linearly with L, at least as soon as the time spent connecting the modules to each other and then to the leads (which has to done at each desired length) is larger than the time spent calculating the Green's functions of the basis modules.

4.1.2 Supermodule method

Instead of connecting single modules one by one to form a long wire, the basic idea is to calculate ever longer wires by creating *supermodules* out of random permutations of the original modules. These *supermodules* are, in turn, used as the building blocks for the next step, creating the second generation of supermodules out of permutations of the first. Repeating this process leads to an exponential growth of the wire length. The idea of using this "exponentiation" technique to achieve the desired wire lengths was inspired by [58], where it is used for the single slices of standard RGM.

We proceed in the following way: As in the single module case, N_m basic modules with uniformly distributed heights are created. Thereafter, these modules are used to create N_m new modules, each consisting of a random permutation of the original modules, as shown in Fig. 4.3 for the case of $N_m = 4$. Thus, after one step we have N_m new supermodules consisting of N_m original modules each. Even though they represent longer systems, each of the supermodules only requires as much computer memory as one of the original modules. This is because we only need to keep that part of the Green's function available for further processing that connects the left edge of the module to the right edge.

After n steps with this method, we have N_m supermodules, each built out of $(N_m)^n$ original modules, i.e. the length of the supermodules (and thus the disordered region) grows exponentially with each step. In this way, the time required to calculate a wire with length L is proportional to $\log(L)$. Additionally, we have N_m

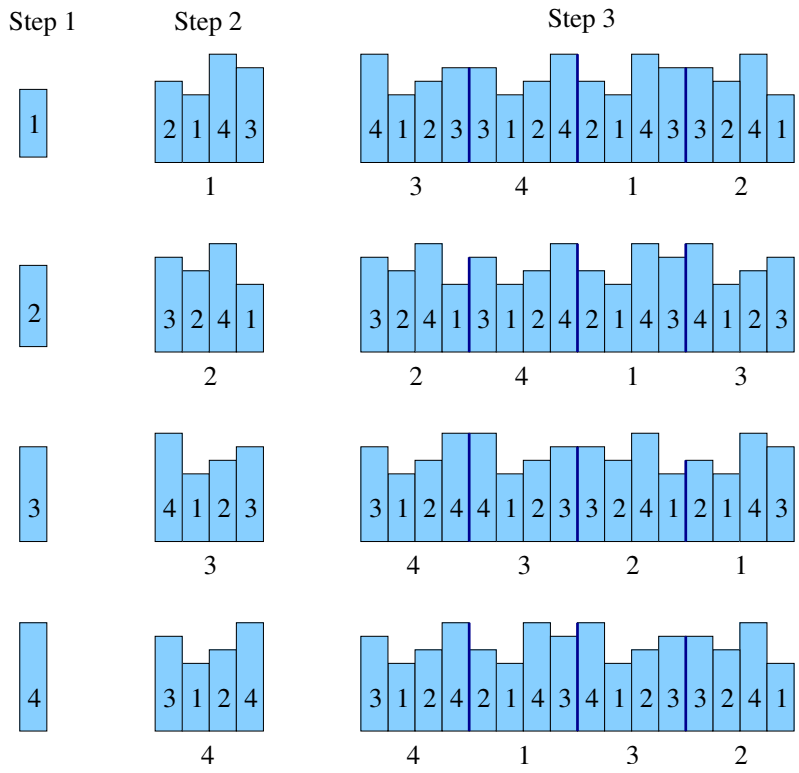

Figure 4.3: *Illustration of the first 3 steps of the supermodule method, with* $N_m = 4$.

different wires of the same length at our disposal, which can be used for averaging over configurations.

After each of the steps in the procedure, leads are connected to both sides of the system and the transmission (reflection) matrix t (r) is calculated. One problem that arises is that this algorithm only produces results for those wires that consist of a number of modules that is a power of N_m. For the typical value $N_m = 20$, we would only have the scattering matrix for 8 different lengths of the wire before we have created a system with a total number of $20^8 = 2.5 \cdot 10^{10}$ modules.

To counteract this problem, we also calculate the scattering matrix at intermediate stages while combining the modules with each other. Consider the following example: If $N_m = 20$, the modules for each step are assembled out of 20 modules from the previous step. Instead of only calculating t and r when the new supermodules are fully assembled, we connect leads and calculate t and r whenever the new supermodules consist of $4, 8, 12, 16$, and 20 modules from the previous step.

The ultimate limit on the wire length which we can still describe with our approach is fixed by a numerical inaccuracy which reveals itself in terms of a loss of unitarity (i.e. $T_m + R_m \neq 1$). Within the MRGM, there are two main sources of

unitarity errors:

(1) First there is the calculation of the eigenfunctions in the lead. This error is independent of the length of the disordered region in between the leads. We find, however, that this error increases with increasing magnetic field. Optimization work that went into this routine lead to a decrease of the error by two orders of magnitude (with the error being smaller than 10^{-5} for typical parameter values before optimization).

(2) The second source of error can be considered as a combination of two different error sources that both exhibit the same behavior with increasing system size. One is the calculation of the Green's functions of the modules themselves and the other is the "welding together" of the modules. Both of these lead to the same behavior of the unitarity error, which grows with increasing wire lengths. Optimizing our code, we were able to suppress this error source well enough that it gives rise to much smaller inaccuracies than the error introduced by the calculation of the lead for typical parameter values. Still, it increases exponentially with the wire length, thereby setting an effective upper limit for the maximum length of the disordered region that can be calculated with our method.

For the parameter values used in this report, the error is typically below 10^{-5} even for the longest wires we calculate, where the disordered region consists of about 10^{11} modules. Only for high energies and magnetic fields does the loss of unitarity indeed become a problem. We find that at the upper limit of accessible energies and wire lengths unitarity deficiencies differ strongly from sample to sample.

4.1.3 Comparison of the single module and the supermodule method

Since the supermodule method works by using permutations of modules to create supermodules, etc., we tested whether the results would be the same as for choosing blocks in a truly random fashion (as in the single module version of the program). To investigate this, we used the same wire parameters for both the single module as well as the supermodule methods to get directly comparable results. As can be seen in Fig. 4.4, the agreement is excellent.

As a further test we investigated whether the results obtained would still accurately represent a random wire once the supermodules are longer than the localization length (enabling the same localized state to exist many times in the wire). To test this, a wire with one-sided surface disorder with 2 open modes was calculated with the single module method up to a length of 10000 modules and compared with a system with the same parameters calculated with the supermodule method. Only 2 open modes were used because of two reasons: First, the localization length is lower at lower energies (i.e. fewer open modes), as will be shown in section 5.2. The wire then does not have to be as long to enter the localized regime as at a higher

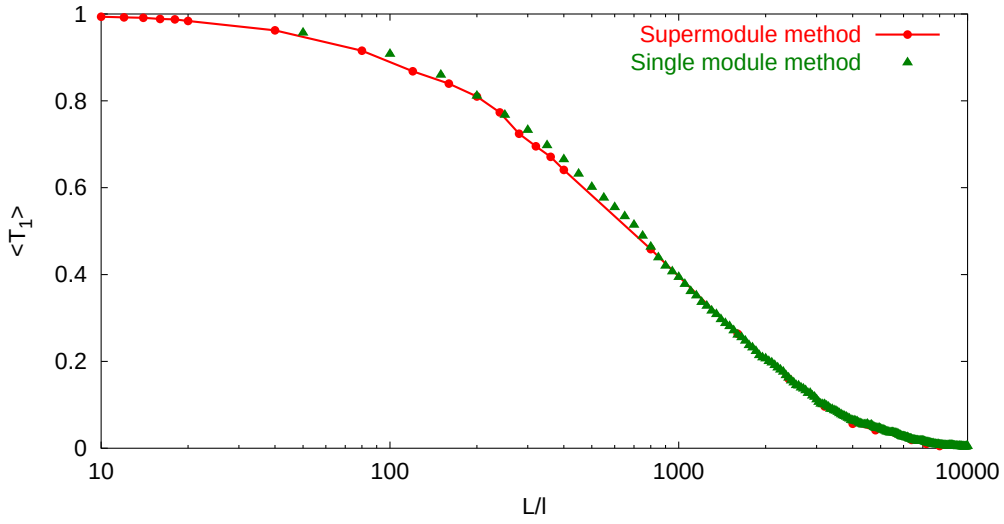

Figure 4.4: *Total transmission probability* $\langle T_1 \rangle$ *of mode 1, plotted against* $L/l \in [10, 10^4]$. *Note the excellent agreement between the supermodule method and the single module method, which is equally good for the transmission probabilities* T_{mn} *from mode* n *to mode* m *(not shown). The following values were chosen:* $W = 1$, $l = 0.2$, $r_c = 3$, $\eta \in [5.1001, 5.1901]$ *(10 equidistant steps),* $N_m = 20$, $\delta_u = 2/3$, $\delta_l = 0$. *The averaging* $\langle \ldots \rangle$ *was done over 10 energies and 20 different configurations for each of the methods.*

number of open modes. The second reason is that fewer open modes require much less computational effort, making it possible to calculate the required lengths even with the single module method. Fig. 4.5 shows that the results of the supermodule method are in excellent agreement with those of the single module method over many orders of magnitude. We conclude that the quasi-randomness invoked by employing supermodules longer than the localization length does not prevent the results from reflecting those of a truly random wire.

4.1.4 Two leads of different widths

To complement the analytical calculations in chapter 6, we implement the scattering problem of two leads of different widths w_L, w_R attached to each other, as shown in Fig. 4.6. The relevant parameters are the two widths w_L and w_R, the Fermi momentum k_F and the magnetic field B (or, equivalently, cyclotron radius r_c).

This simple geometry can be used to investigate the behavior of the wave function at the junction of two modules in a rough wire in more detail. Specifically, we employ it to numerically calculate the transmission and reflection matrices for the

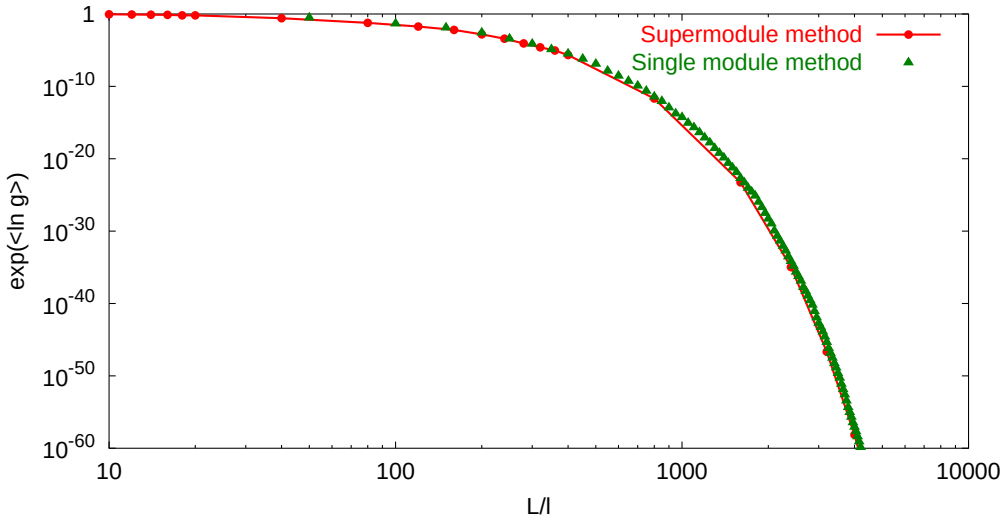

Figure 4.5: $\langle \ln g \rangle$ *plotted against* $L/l \in [10 : 10^4]$. *Again, the agreement between the results of the single module method and the supermodule method is excellent. Parameters used:* $W = 1$, $l = 0.2$, $r_c = 3$, $\eta \in [2.3101, 2.4001]$ *(10 equidistant steps),* $N_m = 20$, $\delta_u = 2/3$, $\delta_l = 0$. *These were chosen such that the localization length* ξ *is small enough that a wire of length* $L \gg \xi$ *can still be calculated with the single module method. The averaging was done over 10 energies and 20 configurations.*

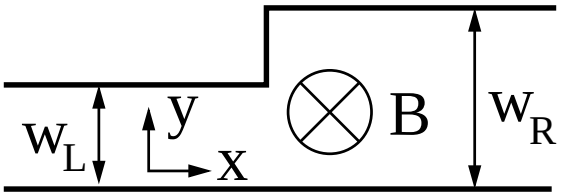

Figure 4.6: *Two leads*

junction of two modules, as discussed in chapter 6 and use the numerical results to complement and justify our analytical approximations.

4.2 Parameter values

There are a number of parameters that determine the properties of our quantum wire with surface disorder. In this section we discuss these parameters and the values chosen for them. The first group of parameters describe the geometry of the

wire. These are the average width W of the wire, the ranges of variation δ_u and δ_l of the wire boundary at the upper and lower side, respectively, and the length l of each slice. Additionally, we have the total length of the wire L, which we normally express by the number of modules, i.e. L/l. The Fermi momentum k_F is specified by $\eta = k_F W/\pi$, where $[\eta]$ gives the number of open modes in the leads if there is no magnetic field. Although increasing the magnetic field while keeping k_F fixed decreases the number of open modes, we always stay in a parameter regime where $N = [\eta]$.

The strength of the magnetic field is determined in our units by B/c, with c the speed of light. Since the classical dynamics is determined by the cyclotron radius $r_c = ck_F/B$, we normally list r_c instead of specifying B directly. The classical dynamics is invariant under a change of the Fermi momentum k_F as long as B is changed in parallel such that r_c is constant. Any effects we see by changing k_F must then be purely quantum mechanical.

For reasons of simplicity, we always choose $W = 1$ for the width of the wire. For the one-sided rough wire, we fix the disorder amplitude as $\delta_u = 2/3$ (with $\delta_l = 0$) and choose a cyclotron radius $r_c = 3$ significantly larger than the width of the wire $W = 1$ to ensure that we are not in the quantum Hall regime. As the classical dynamics then does not depend on the Fermi momentum k_F, this determines the size of the regular island in phase space. With $r_c = 3$, we are far away from the regime of the quantum Hall effect [10], as classical paths have a radius of curvature $r_c = 3$ much larger than the width of the wire $W = 1$. In the case of the wire with two-sided surface disorder, we choose $\delta_u = \delta_l = 1/3$, so that $\delta_l + \delta_u$ for two-sided surface disorder equals δ_u for one-sided surface disorder. Unless otherwise stated, we always use these parameter from now on.

The length l of each slice does not have any effect on the classical phase space, but introduces a new scale $k_F \cdot l$ for quantum mechanics. As we later argue, this scale does not significantly influence the dynamics for the wire with OSD, so we choose $l = 0.2$.

Chapter 5

Results

Using the single module method and the supermodule method as described above, we now analyze the behavior of wires with one-sided (OSD) and two-sided surface disorder (TSD). In the first part of this chapter, we study wires with TSD and compare our findings to existing results and predictions [12, 14–17, 46–48]. In the second part, we study one-sided surface disorder and highlight the new effects that arise.

5.1 Two-sided surface disorder

For wires with TSD, we expect that some of the predictions made for bulk disorder (see section 2.3) are still valid, especially in the presence of a large disorder strength ($\delta_l = \delta_u = 1/3$, with $W = 1$), which gives rise to strong intermode mixing. In that case, the isotropy assumption from random matrix theory is almost fulfilled and we expect to find clearly distinct diffusive and localized regimes. As we are dealing with two-sided disorder here, the mean free paths and localization lengths are quite small, so that we can use the single module method for simulating the systems involved.

For wire lengths L less than the localization length, we expect to be in the diffusive regime, which is characterized by an Ohmic behavior (i.e. linear increase) of the resistance $R \equiv 1/g$ [38–40],

$$\left\langle \frac{1}{g} \right\rangle = \frac{1}{N} + \frac{L}{Nl^e} \qquad l^e \ll L \ll \xi. \tag{5.1}$$

In Fig. 5.1, we show $\langle 1/g \rangle$ for a wire with TSD and see very good agreement with the expected result. The average resistance increases linearly with wire length up to a certain length, where localization sets in and the resistance increases exponentially. This localized regime is characterized by the following behavior

$$\langle \ln g \rangle \propto -\frac{L}{\xi} \qquad L \gg \xi. \tag{5.2}$$

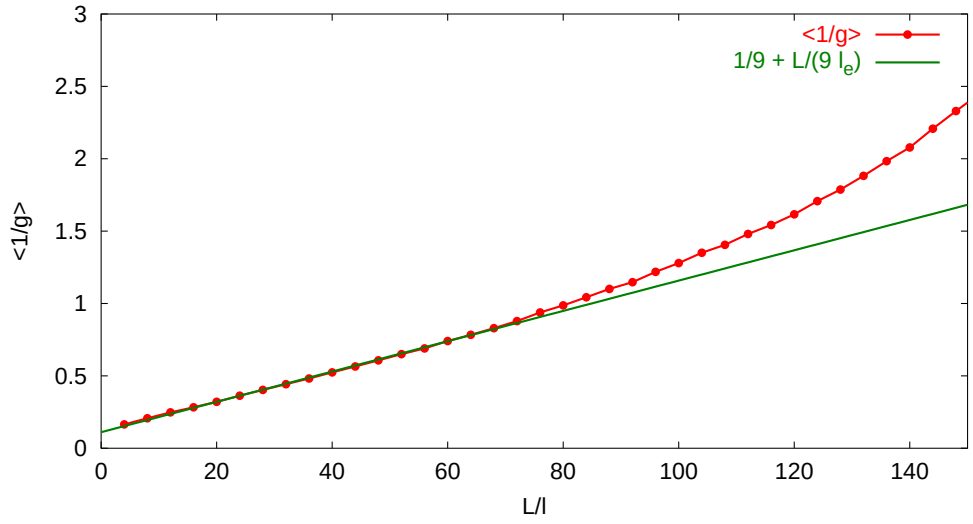

Figure 5.1: $\langle 1/g \rangle$ *for a wire with TSD in the diffusive regime, plotted against* L/l*. The wire has* 9 *open modes,* $\eta \in [9.6001, 9.6901]$ *(10 equidistant steps),* $N_m = 20$*. The averaging was done over 10 energies and 100 configurations. Note that the resistance does indeed approach* $\langle 1/g \rangle = 1/N$ *for* $L \to 0$*, as predicted by Eq. (5.1).*

As can be seen in Fig. 5.2, this expectation is again very well fulfilled. We might conclude from these results that the wire with TSD behaves like a wire with *bulk* disorder. However, in contrast to bulk disorder, we expect some mode dependence of the transmission [12].

The higher modes, which correspond to injection of the electron at a steeper angle, should suffer more scattering than the lower modes. To verify this, we study the total transmission probabilities T_m of the individual modes (Fig. 5.3). We see that the high modes indeed have transmission probabilities that are significantly smaller than those of the low modes. Still, all modes enter the localized regime at about the same length $L \approx \xi$ and then decay exponentially according to

$$\langle \ln T_m \rangle \propto -\frac{L}{\xi}, \tag{5.3}$$

as is nicely corroborated by the numerical data shown in Fig. 5.3.

5.1.1 Relation between mean free path l^e and localization length ξ

Since we are able to define a mean free path l^e through Eq. (5.1) and a localization length ξ through Eq. (5.2), we can now investigate whether these two quantities

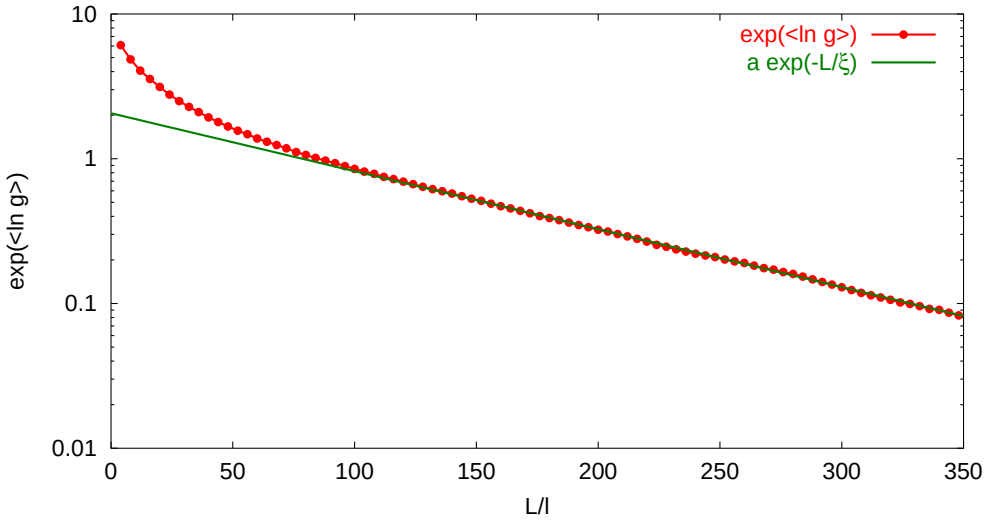

Figure 5.2: $\langle \ln g \rangle$ *for a wire with TSD in the localized regime, plotted against* L/l. *The wire has* 9 *open modes,* $\eta \in [9.6001, 9.6901]$ *(10 equidistant steps),* $N_m = 20$. *The averaging was done over 10 energies and 100 configurations.*

are related to each other as predicted by random matrix theory [11]

$$2\xi \approx (\beta N + 2 - \beta) l^e, \tag{5.4}$$

where N is the number of open modes and $\beta \in \{1, 2, 4\}$ is a symmetry index. $\beta = 4$ only occurs when there is spin-orbit scattering, which is not included in our simulation. In systems without time reversal symmetry (when $B \neq 0$), $\beta = 2$, while $\beta = 1$ if time reversal symmetry is preserved (no magnetic field). The number of open modes N directly depends on the Fermi momentum k_F. We thus calculate the mean free path and the localization length for a range of energies and compare with the predictions.

We show the ratio $2\xi/l^e$ for the case of a weak magnetic field (red) and no magnetic field (green) in Fig. 5.4 and find that our results do satisfy the prediction from RMT for bulk disorder in the respect that $2\xi/l^e$ does increase linearly. Fig. 5.4 also shows fits to

$$2\xi = (\beta N + \alpha) l^e. \tag{5.5}$$

The results obtained by fitting do not agree with the predictions very well. The offset α obtained by fitting is not $2 - \beta$, and the factor β is not found to be equal to one for the case of no magnetic field. Additionally, β does not double after turning on the magnetic field, although it the results do fit to $\beta \approx 2$. An explanation for this surprising result remains a future challenge.

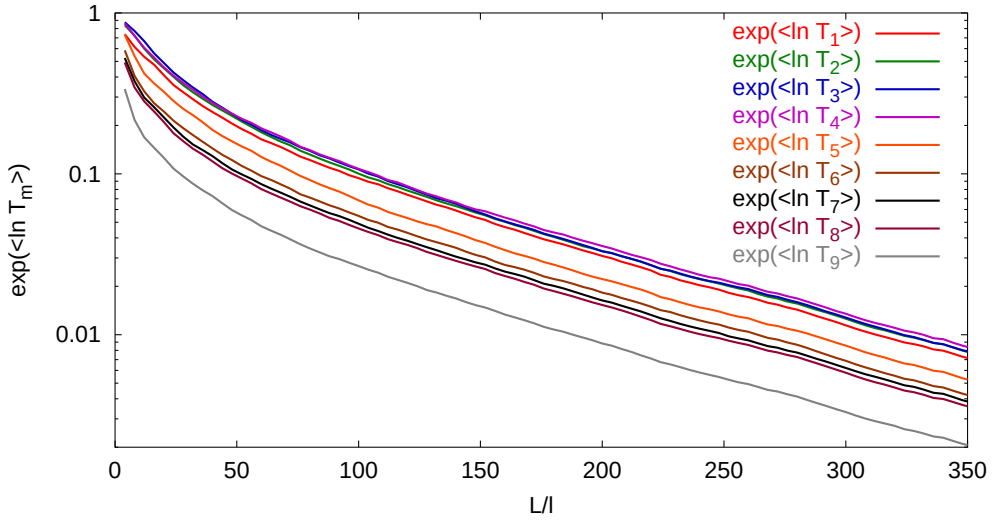

Figure 5.3: *Total transmission probabilities T_m of the individual modes m for a wire with TSD plotted against L/l. The wire has 9 open modes, $\eta \in [9.6001, 9.6901]$ (10 equidistant steps), $N_m = 20$. The averaging was done over 10 energies and 100 configurations.*

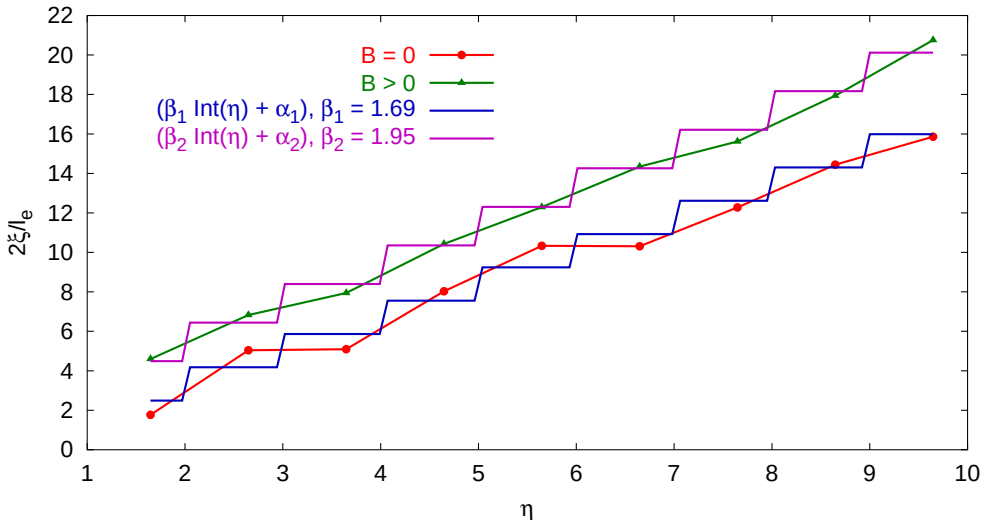

Figure 5.4: *Ratio of 2ξ to l^e, plotted against η, for a wire with TSD with a magnetic field (red) and without a magnetic field (green). Also shown are fits to $2\xi/l^e = \beta N + \alpha$ for both cases.*

5.2 One-sided surface disorder with a magnetic field

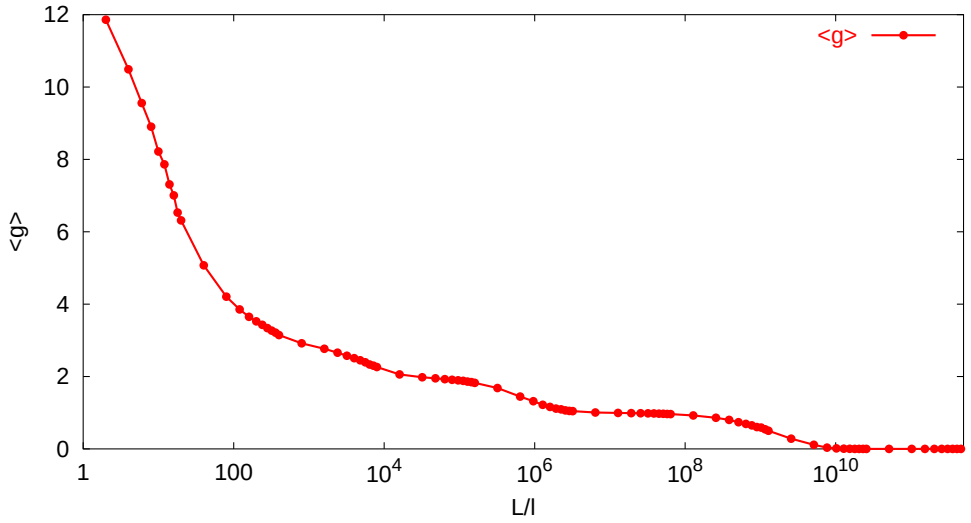

Figure 5.5: $\langle g \rangle$ *for a wire with one-sided surface disorder in a magnetic field, plotted against* L/l. *The wire has 14 open modes,* $\eta \in [14.5932, 14.6282]$ *(6 steps),* $N_m = 20$. *The averaging was done over 6 energies and 20 configurations.*

We now turn our attention to wires with one-sided surface disorder in the presence of a magnetic field. Fig. 5.5 shows the average transmission $\langle g \rangle$ for such a wire. Instead of localized behavior after a few hundred modules, which we saw for two-sided surface disorder, we now observe transmission for extremely long wires, on the order of 10^{10} modules (note the logarithmic scale in Fig. 5.5!)

The non-vanishing conductance through long wires can be understood by studying the classical phase space of our system, which we do by evaluating the classical Poincaré surface of section at the interface between the incoming lead and the disordered region[1] (see Fig. 5.6). As the Poincaré surface of section is located in the interior of the wire, it is not necessary to employ normal derivatives. as is otherwise often done [61, 62].

The phase space of the system is calculated using the concept of Poincaré scattering maps, which amounts to using periodic boundary conditions for the classical electron trajectories, i.e. the electrons re-enter the wire at the left side at the same position and with the same momentum as they leave it at the right side. Every time a trajectory crosses the Poincaré surface of section, its transverse position y

[1] Many thanks to Arnd Bäcker for writing the classical simulation.

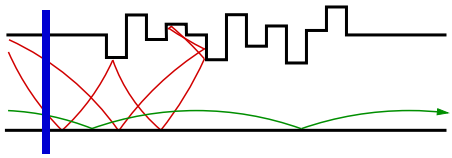

Figure 5.6: *Rough wire with the position of the Poincaré surface of section in blue.*

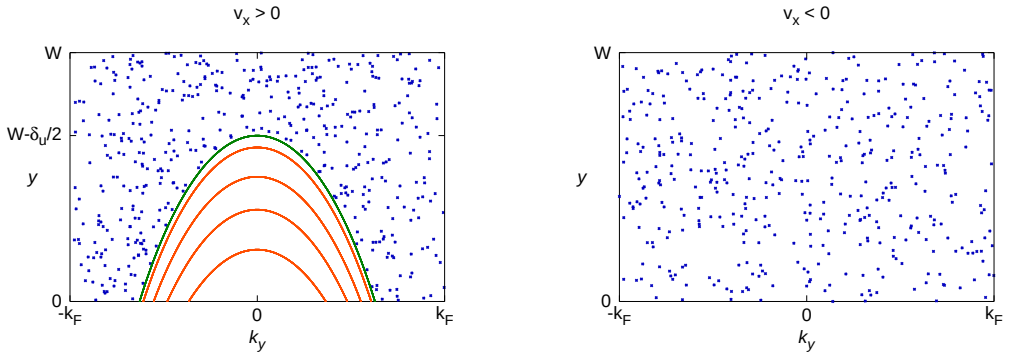

Figure 5.7: *Poincaré surface of section (PSS) of phase space for a wire with one-sided surface disorder in a magnetic field. Left: PSS for right-moving electrons ($v_x > 0$), right: PSS for left-moving electrons ($v_x < 0$). The tori in the regular island (orange) are those given by the semiclassical quantization condition (5.12), determined for $\eta = 14.6$.*

and momentum p_y are recorded. This map can be shown to be the classical analog of the quantum mechanical scattering matrix S [20, 63, 64]. A phase space portrait obtained in this way is shown in Fig. 5.7.

The tori in the regular island correspond to classical paths that never hit the upper boundary, i.e. the surface with disorder, as shown in Fig. 2.5. Because of the regular motion the canonical momentum in the x-direction p_x of these "skipping orbits" is conserved, in addition to the energy, which is conserved for all trajectories. Choosing the Landau gauge, the electromagnetic potential $\mathbf{A}$ corresponding to a magnetic field $\mathbf{B} = \nabla \times \mathbf{A} = -B\,\hat{\mathbf{z}}$ is given by (cf. Eq. (3.11))

$$\mathbf{A} = By\,\hat{\mathbf{x}} \tag{5.6}$$

We employ energy conservation to derive the relationship between k_y and y for the classical skipping orbits,

$$E = \frac{1}{2}\left(\mathbf{p} + \frac{1}{c}\mathbf{A}\right)^2, \tag{5.7}$$

inserting $E = k_F^2/2$ and $r_c = ck_F/B$ and solving for y, we get

$$y = r_c \left(\sqrt{1 - \left(\frac{k_y}{k_F}\right)^2} - \frac{k_x}{k_F} \right). \tag{5.8}$$

In order for a skipping orbit not to reach the disordered region at the top of the wire, the highest point of the orbit (at which $k_y = 0$) has to be lower than $W - \delta_u/2$, which determines the position of the outermost torus seen in Fig. 5.7. It follows that states on the regular island must satisfy

$$\frac{k_x}{k_F} \geq 1 - \frac{\Delta}{\zeta}, \tag{5.9}$$

where we have introduced the dimensionless parameters $\Delta = 1 - \delta_u/(2W)$ and $\zeta = r_c/W$. For the parameter values used throughout this thesis, we have $\Delta = 2/3$ and $\zeta = 3$, such that for states in the regular island we must have

$$\frac{k_x}{k_F} \geq \frac{7}{9} \tag{5.10}$$

As noted before, the classical dynamics is completely determined by the cyclotron radius, which determines the shape of the trajectories (circular segments with radius r_c).

Quantum mechanically, we expect to find states that live on this regular island and suffer very little scattering. These states should traverse the disordered region relatively undisturbed, explaining why we find transport even for very large wire lengths. To verify our assumption, we study the transverse wave functions in the wire and calculate the corresponding Husimi distributions. The Husimi distribution is one possible quantum mechanical analog to the classical phase space density and is given by the projection of the wave function onto coherent minimum uncertainty states $\psi_{[y,k_y]}(y')$, which are Gaussian wave packets with $\langle \hat{y} \rangle = y$ and $\langle \hat{k}_y \rangle = k_y$. The Husimi distribution $H(y, k_y)$ is given by

$$H(y, k_y) = \left| \int_0^W \phi(y') \psi_{[y,k_y]}(y') \mathrm{d}y \right|^2 \tag{5.11}$$

for a transverse wave function $\phi(y)$. By using a semiclassical (Bohr-Sommerfeld) quantization condition for the magnetic flux enclosed by a segment of the skipping orbit, we obtain a semiclassical condition for the allowed modes, [65]

$$\frac{A}{h} = \frac{B\mathcal{A}}{hc} = m - 1/4 \quad \text{with } m = 1, 2, \dots \ , \tag{5.12}$$

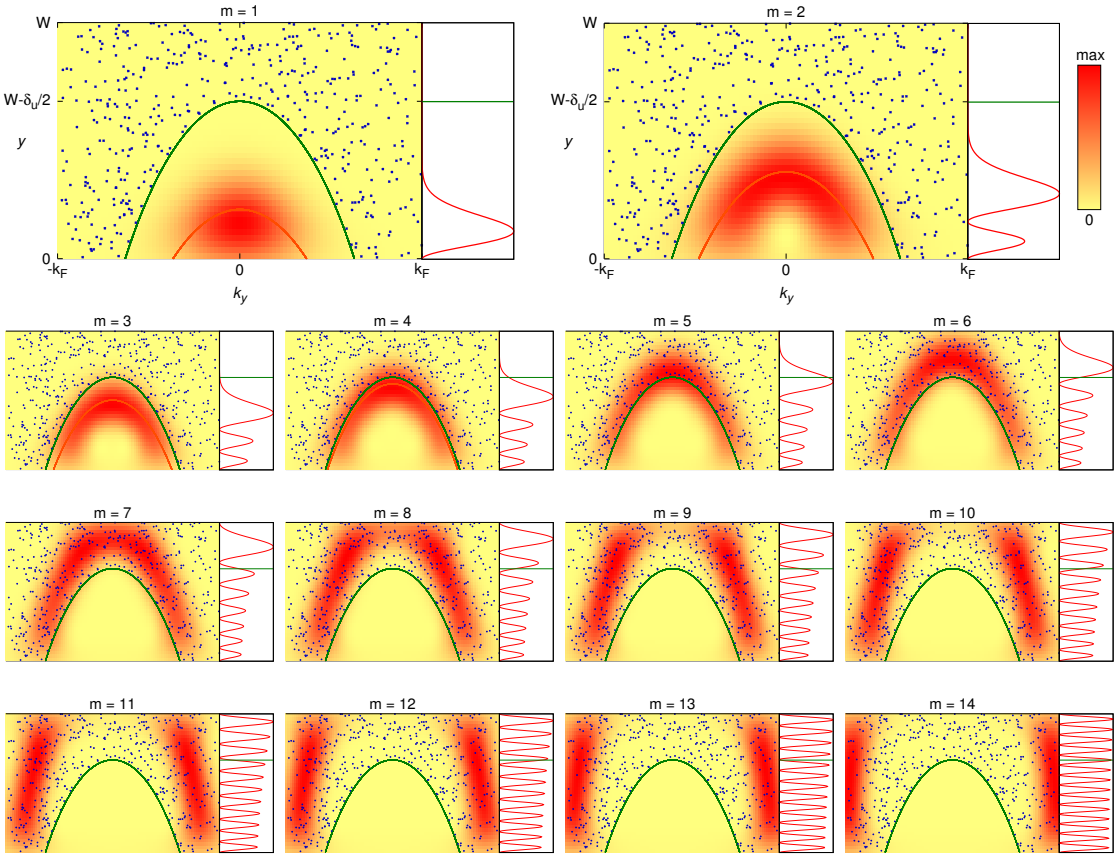

Figure 5.8: *Husimi distributions of the modes in the leads, where the classical phase space has been overlaid. For the four lowest modes, the quantized torus determined by Eq. (5.12) is also shown for comparison (orange line). To the right of the Husimi distributions, the wave functions in position space are plotted.*

where A is the area enclosed by the torus in the Poincaré surface of section and $\mathcal{A}$ is the area enclosed by one segment of the skipping orbit.

Fig. 5.8 shows that the transverse modes χ_m^+ with low quantum numbers m live on the regular island, thus confirming our expectations. Since the classical trajectories corresponding to these states would not suffer scattering, their eventual scattering must be explained by a purely quantum mechanical effect, which we find to be *tunneling*. The tail of the wave function extends into the disordered region, so that there is a finite, albeit small, probability of scattering.

Tunneling out of the first mode leads to localized behavior: If a small fraction ε of the flux tunnels out of the first mode at every transition from module to module,

the resulting transmission will be

$$|t_{11}|^2 \approx (1-\varepsilon)^{2N} \approx \exp(-2N\varepsilon), \tag{5.13}$$

where $N = L/l$ is the number of modules in the disordered region. This implies localized behavior with localization length $\xi = l/(2\varepsilon)$. As shown in Fig. 5.9, the conductance, which for long wires is dominated by the transmission of the first mode, does indeed decrease exponentially with L.

The obtained localization length ξ is of the order of $\sim 10^{10}$ modules. This very high value indicates that we are approaching the classical limit where quantum mechanical wave packets behave like classical particles. To investigate this more closely, we study the behavior of the localization length ξ as we perform this limit.

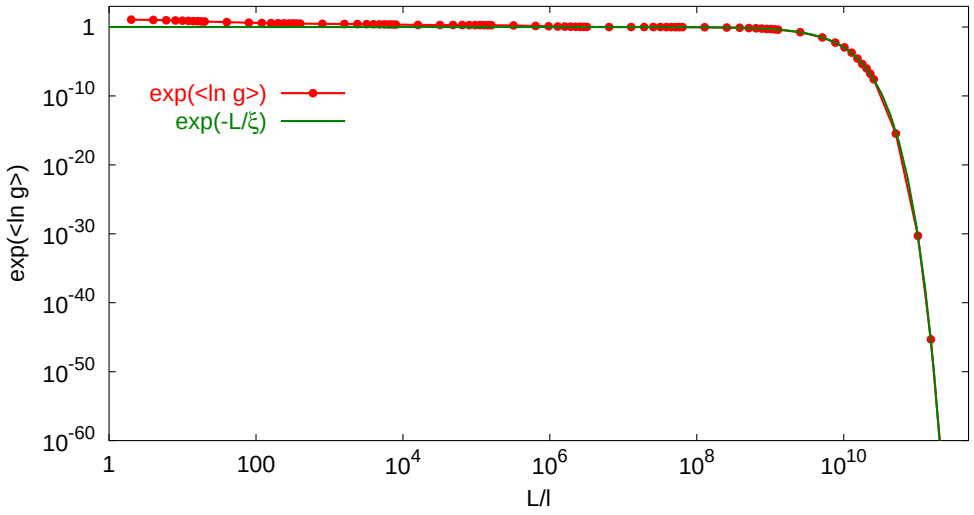

Figure 5.9: $\langle \ln g \rangle$ *for a wire with one-sided surface disorder in a magnetic field, plotted against* L/l*. The wire has 14 open modes,* $\eta \in [14.5932, 14.6282]$ *(6 steps),* $N_m = 20$*. The averaging was done over 6 energies and 20 configurations.*

5.2.1 Quantum-to-classical crossover

Since tunneling is a quantum mechanical effect, it should vanish in the classical limit $k_F \to \infty$ of high energies. This limit is often symbolically written $\hbar \to 0$, meaning that all involved actions become large compared to $\hbar$, or, correspondingly, that all length scales become large compared to the de Broglie wavelength of the electron. In this limit, quantum mechanical wave packets should follow classical trajectories and generally behave like classical particles according to the Ehrenfest theorem [66, chapter 3].

Note that due to the sharp edges at every junction of two modules, we have a length scale that is effectively zero and thus does not become negligibly small compared to the de Broglie wavelength even in the limit of large k_F. At these sharp edges, the wave function undergoes diffractive scattering, which should lead to a deviation from the classical behavior that does not vanish in the classical limit. In our specific system, the properties of motion in a magnetic field come to our rescue, though. As we shall see, the gauge potential effectively shields the modes that are responsible for the localized behavior from the sharp edges.

We thus proceed with studying the behavior of the localization length ξ as we increase the Fermi momentum k_F. The localization length is obtained by fitting according to Eq. (2.15),

$$\langle \ln g \rangle \propto -\frac{L}{\xi} \qquad L \gg \xi. \tag{5.14}$$

To keep the classical dynamics unchanged, we keep $r_c = ck_F/B$ constant while taking the limit $k_F \to \infty$, so that B increases along with k_F. The phase space then does not change apart from a trivial linear scaling with k_F. The corresponding classical trajectories of the electrons are exactly the same at each energy (circular segments with radius of curvature r_c). Thus, our limit is a pure quantum-to-classical crossover, where the quantum dynamics corresponds to the same classical dynamics for all k_F. As we see in Fig. 5.10, the localization length for wires with one-sided disorder in a magnetic field drastically increases with growing k_F, in striking contrast to the cases of OSD with $B = 0$ and TSD (with or without a magnetic field).

A general prediction for tunneling from a regular island in phase space in the classical limit states that the tunneling rate from the innermost state in a regular island to the chaotic sea outside (which is inversely proportional to the localization length in our case) should exponentially depend on the ratio of the area A_{reg} of the regular island in phase space (which corresponds to an action) and Planck's constant h [23–28]

$$\gamma_1 \propto \exp\left(-C \cdot \frac{A_{\mathrm{reg}}}{h}\right), \tag{5.15}$$

$$\xi \propto \exp\left(C \cdot \frac{A_{\mathrm{reg}}}{h}\right). \tag{5.16}$$

This prediction was made in connection with *dynamical tunneling*, which is a term used to signify that the tunneling process does not take place through a classically forbidden potential. Instead, the tunneling connects two regions that are separated by the dynamics of the system in a classical description [19].

Each quantum mode occupies one Planck cell in phase space, i.e. an area of h, so that A_{reg}/h corresponds to the number of modes that can live on the island. Consequently, the above prediction is only valid if $A_{\mathrm{reg}} > h$, such that at least one

mode can live on the island. We note in passing that the predictions from random matrix theory (RMT) given in subsection 5.1.1 for two-sided surface disorder are not applicable, since fundamental assumptions of RMT, such as the isotropy of transmission into all outgoing channels, are violated. Additionally, because the scattering proceeds very differently for the individual modes, it is not possible to properly define a mean free path l^e, rendering any prediction that connects ξ and l^e (such as Eq. (5.4)) essentially meaningless[2].

Since the relative area of the regular island stays the same for all k_F when we keep the cyclotron radius r_c constant, its absolute area scales in the same way as the total area of the phase space in our Poincaré surface of section. Therefore, we do not actually have to calculate the area of the regular island in phase space to determine its scaling with k_F. The total phase space area is given by $A_{\text{tot}} = 2p_F \cdot W$, which in our case (atomic units, $W = 1$) becomes $A_{\text{tot}} = 2k_F$. With $A_{\text{reg}}/A_{\text{tot}} = \text{const}$, we thus find that the localization length should increase exponentially with k_F,

$$\xi \propto \exp\left(C' \cdot k_F\right). \tag{5.17}$$

We will find (see below) that this simple estimate already provides a good approximation to the behavior observed numerically. A detailed analytical calculation performed in chapter 6 yields (cf. Eq. (6.81))

$$\frac{\xi}{l} \approx (\alpha_1 \eta^{2/3} + \alpha_2) \exp\left[\alpha_3 \eta (1 - \alpha_4 \eta^{-2/3})^{3/2}\right] \propto \exp\left(\alpha_3 \eta\right), \tag{5.18}$$

where $\eta = k_F W/\pi$ and the α_i are dimensionless parameters. We thus find exactly the predicted exponential increase with k_F (for details refer to chapter 6).

This result agrees with Eq. (5.17) for asymptotically large k_F. The prediction made from general results about tunneling in a mixed regular-chaotic phase space is thus found to be valid. The appeal of Eq. (5.17) is that it predicts a purely quantum mechanical quantity (the tunneling rate) from a simple classical quantity (the area A_{reg} of a regular island in phase space).

We have thus demonstrated that our quantum wire with one-sided surface disorder in a magnetic field is very well suited to study the quantum-to-classical crossover of transport in a cavity with regular-chaotic motion. As we show, the mixed phase space leads to an exponential divergence of the localization length in the classical limit. We stress that in the case of a wire with OSD, but without a magnetic field, or a wire with TSD regardless of the magnetic field, we do not find this behavior, since the underlying phase space does not include a regular island in that case. The fact that the giant localization length vanishes if we include two-sided surface disorder proves that the system is not in the parameter regime of the quantum Hall effect.

[2]Note that this reasoning also applies in the case of TSD. But since we chose a large disorder strength, which enhances intermode mixing, the deviation from the RMT result for wires with TSD is small enough to justify calculating an elastic mean free path by fitting.

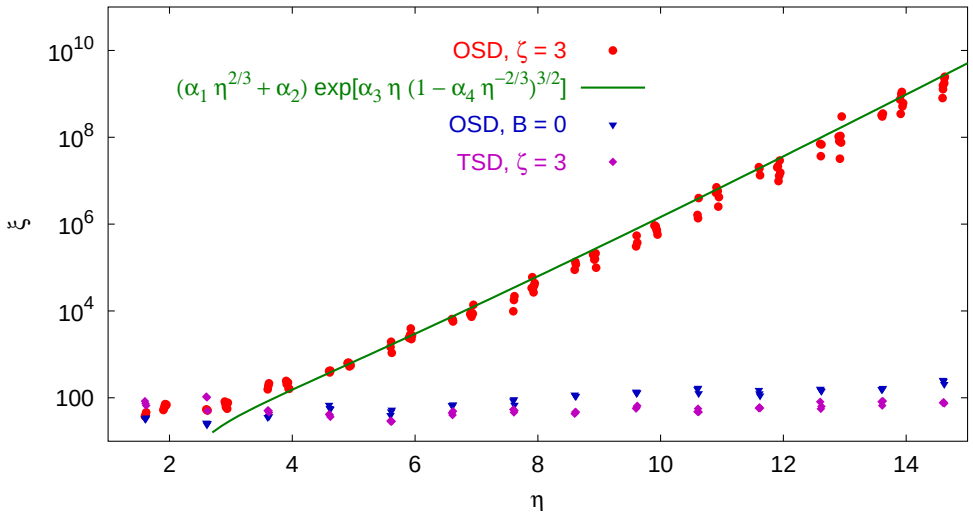

Figure 5.10: *Localization length ξ for a wire with one-sided surface disorder in a magnetic field (red), plotted against η. Here, the cyclotron radius $r_c = 3$ is constant for all energies. For comparison, ξ for wires with OSD without a magnetic field (blue) and for wires with TSD (magenta) are shown. We also show the prediction Eq. (5.18) for ξ from the analytical calculation in chapter 6 (green).*

5.2.2 Crossover at constant magnetic field B

If we again increase the Fermi momentum k_F, but now keep the magnetic field strength B constant instead of the cyclotron radius r_c, the limit we are taking is not a pure quantum-to-classical crossover anymore, as the classical dynamics then depends on the Fermi wavenumber k_F. The relative size of the regular island in phase space shrinks with growing k_F as the cyclotron radius increases and trajectories become more like straight lines. Contrary to the case of constant cyclotron radius, we now have to calculate the area of the regular island to know how it scales with k_F. To do so, we simply integrate the relation (5.8) over the allowed values for k_y in the regular island, inserting the condition for the outermost stable orbit for k_x. The integral corresponds to a classical action $S = \int p\mathrm{d}q$ and is found to be

$$A_{\mathrm{reg}} = k_F r_c \left[\arccos(1-\nu) - (1-\nu)\sqrt{1-(1-\nu)^2}\right] \tag{5.19a}$$

$$\nu = \frac{1}{r_c}\left(W - \frac{\delta_u}{2}\right). \tag{5.19b}$$

Since we are again interested in the limit of large Fermi momentum k_F, but now for constant B, we insert $r_c = ck_F/B$ in Eq. (5.19) and expand it to leading order in k_F. We find that in the limit of large k_F the area of the regular island now

increases with the square root of k_F,

$$A_{\text{reg}} \propto \sqrt{k_F}. \tag{5.20}$$

Combining this result with Eq. (5.15), the localization length should then increase as

$$\xi \propto \exp\left(C'' \cdot \sqrt{k_F}\right). \tag{5.21}$$

Accordingly, our result from the analytical calculation in chapter 6 predicts the same behavior in the limit of large k_F (cf. Eq. (6.84)):

$$\frac{\xi}{l} \approx \left(\beta_1 \eta^{1/3} + \beta_2\right) \exp\left[\beta_3 \sqrt{\eta}(1 - \beta_4 \eta^{-1/3})^{3/2}\right] \propto \exp\left(\beta_3 \eta^{1/2}\right) \tag{5.22}$$

where the β_i are dimensionless parameters. As we see in Fig. 5.11, the localization length indeed shows the behavior predicted in Eq. (5.22).

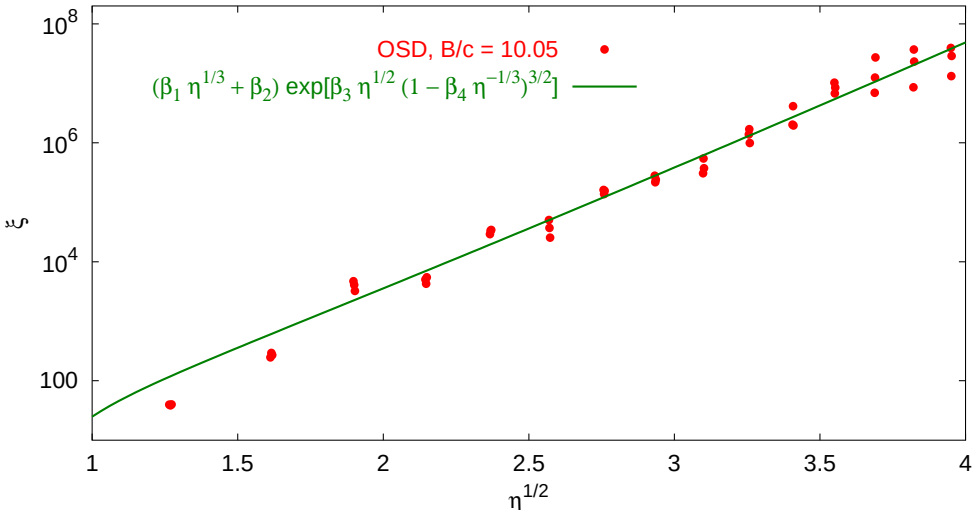

Figure 5.11: *ξ for a wire with one-sided surface disorder in a magnetic field, plotted against $\sqrt{\eta}$. In this figure, the magnetic field B is held constant. We also show the prediction Eq. (5.22) for ξ from the analytical calculation in chapter 6.*

5.2.3 T_m

We now turn our attention to the conductance for wires shorter than the localization length ξ. In Fig. 5.5, three distinct steps can be seen in the average conductance $\langle g \rangle$, following a drastic decrease for short wire lengths. We attribute this decrease to those high modes which lie in the chaotic sea outside the regular island. The

steps we observe for longer wires should then correspond to the modes which tunnel away from the island one after the other, with the tunneling rate getting bigger the closer a state lives to the chaotic sea. To verify these assumptions, we study the transmission probabilities T_m of the individual modes. Since we expect the modes to tunnel out of the island and thus decay exponentially, we investigate $\exp(\langle \ln T_m \rangle)$ in Fig. 5.12. Since the modes on the regular island only couple weakly to other modes, we expect the total transmissions T_m of each of the modes to behave as the conductance g of a one-mode wire, which implies a log-normal distribution of T_m for $\langle T_m \rangle \ll 1$. Therefore, $\exp(\langle \ln T_m \rangle)$ is the correct average.

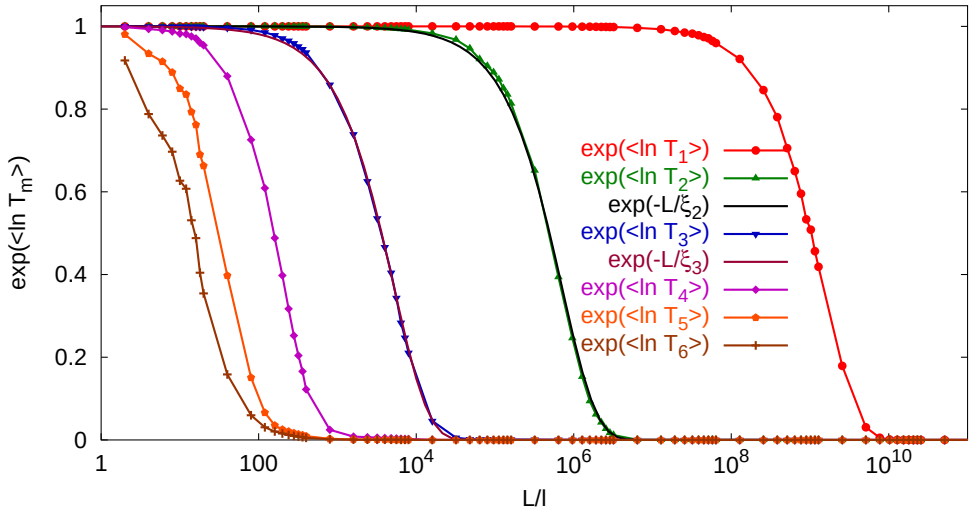

Figure 5.12: *Total transmission probabilities T_m of the individual modes m for a wire with OSD, plotted against L/l. $\eta \in [14.5932, 14.6282]$ (6 steps). The averaging was done over 6 energies and 20 configurations.*

We indeed find that the low modes tunnel out of the regular island one after the other. Additionally, we can perform a fitting procedure analogous to the one for the localization length ξ above and define a *mode localization length* ξ_m for the modes on the island,

$$\langle \ln T_m \rangle \propto -\frac{L}{\xi_m}, \tag{5.23}$$

which corresponds to the inverse tunneling rate of mode m out of the island. The mode localization lengths decrease for higher modes, $\xi_m < \xi_{m-1}$, as the coupling of the mode to the chaotic sea increases. In position space, we see that the exponential tail of the wave function reaches farther into the forbidden region the higher the mode number m (cf. Fig. 5.8). The fits are shown along with the numerical results in Fig. 5.12, demonstrating that the decay of the transmission probabilities T_m is

indeed exponential for the low modes in the island. For the parameters shown in the figure, this fit is good for $m \leq 4$. As there is a finite probability of tunneling into a lower mode, the exponential decrease of the transmission probability of a mode does not continue to arbitrary wire lengths for $m \neq 1$. A small fraction of the incoming flux in mode m tunnels to the lower mode $m-1$. Once in the lower mode, this fraction of the incoming flux will also decay exponentially with increasing wire length, but with a localization length $\xi_{m-1} > \xi_m$. For some length scale the transmission into mode $m-1$ is then the dominant contribution to the transport of mode m, until this part itself becomes smaller than the transmission into mode $m-2$, etc. until finally only transmission into mode 1 is left.

Fig. 5.13 shows the stepwise decrease of the transmission of the higher modes. Since the tunneling probabilities between the modes are very small, we have to use a logarithmic scale to see this behavior. In Fig. 5.14 the transmission probabilities T_{m4} from the fourth mode into the m-th mode are shown to further verify the above description. The transmission of the fourth mode is indeed dominated by T_{44} for short wire lengths, while for increasing lengths, the dominating parts of T_4 are successively T_{34}, T_{24}, and T_{14}.

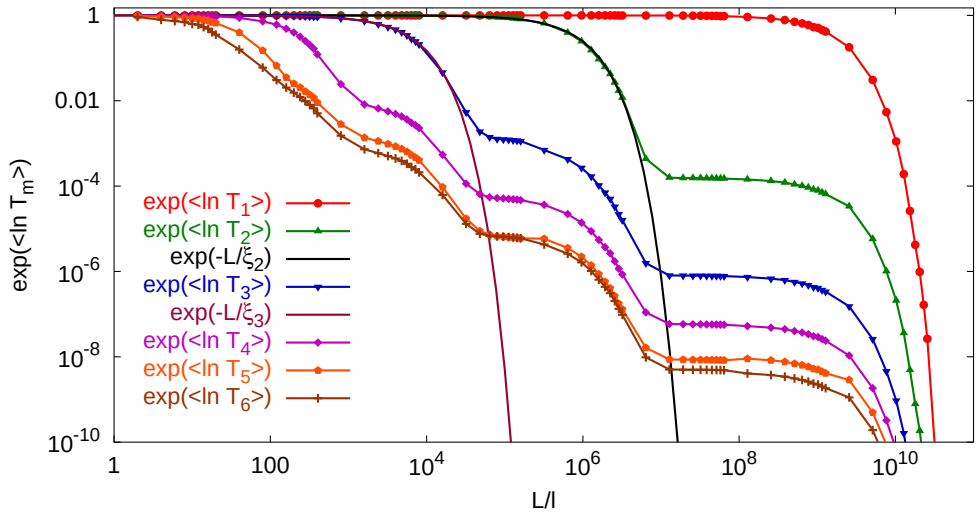

Figure 5.13: *Total transmission probabilities T_m of the individual modes m for a wire with OSD on a logarithmic scale, plotted against L/l. $\eta \in [14.5932, 14.6282]$ (6 steps). The averaging was done over 6 energies and 20 configurations.*

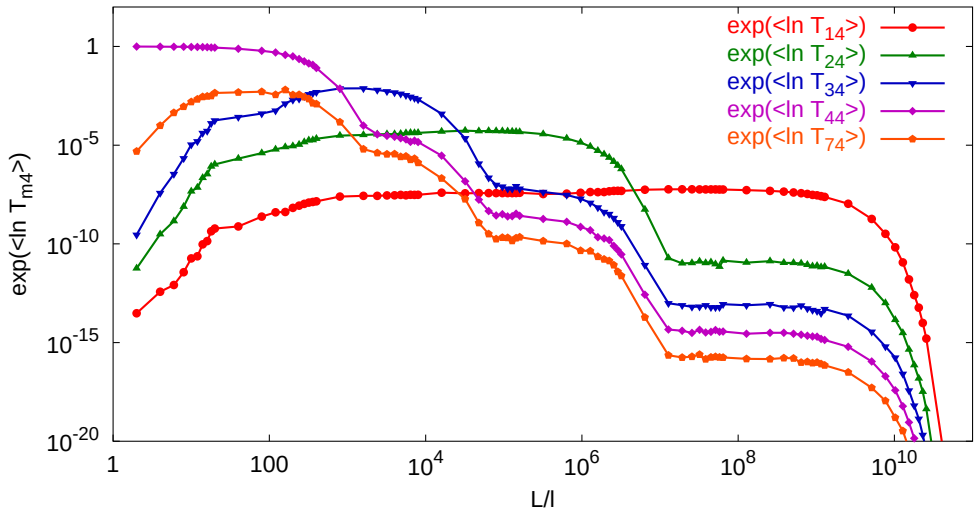

Figure 5.14: *Transmission probabilities T_{m4} from mode 4 to mode m for a wire with OSD, plotted against L/l. $\eta \in [14.5932, 14.6282]$ (6 steps). The averaging was done over 6 energies and 20 configurations.*

5.2.4 T_{m1}

All modes (apart from the first mode) decay in steps, where the decay takes place with the localization length ξ_m of the mode dominating transmission at each length scale. In contrast, the transmission of the first mode is always dominated by T_{11}, but there is of course some transmission into the higher modes. Fig. 5.15 shows the transmission probabilities T_{m1} from the first mode to mode m (for mode m still on the regular island). In this section, we explain the intricate pattern seen in these transmission probabilities with a simplified model proposed by R. Ketzmerick that captures the essential features surprisingly well. This model predicts the transmission probability T_{m1} for transmission from the first mode in the left lead to mode m in the right lead, under the condition that mode m is still on the regular island, by employing ideas from *chaos-assisted tunneling* [24].

To find the flux transmitted into outgoing mode m in the right lead under the assumption that the incoming flux in the left lead was in mode 1, we start out with the realization that there are two possible ways of coupling between the first and the m-th mode that are of the same order. The first is the direct coupling between the two modes, while the second is the two-step process of first tunneling to the chaotic sea and then, after some propagation in the chaotic sea, tunneling to mode m. The direct intermode coupling between the modes on the regular island is of order $\xi_1^{-1}\xi_m^{-1}$. This can be understood by a simple argument: The coupling between modes is induced by the disorder at the top of the wire. Modes on the

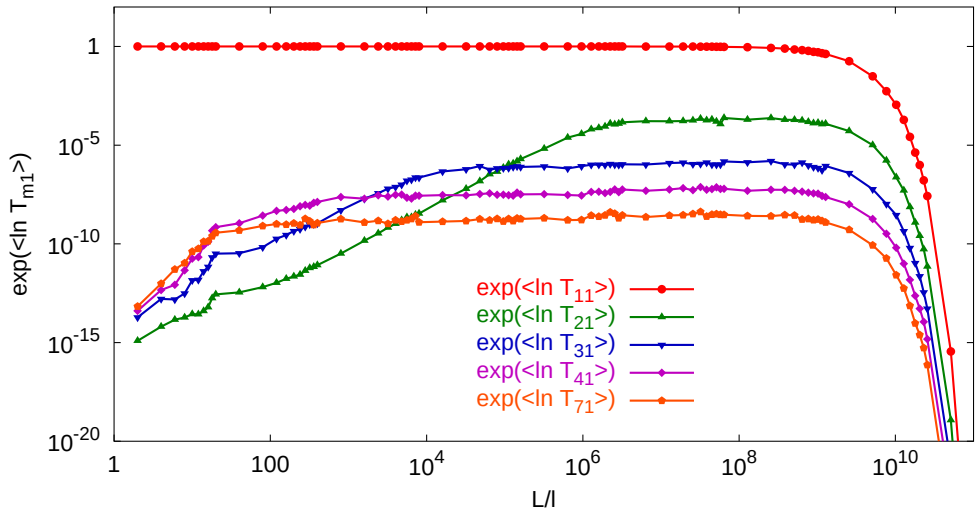

Figure 5.15: *Transmission probabilities T_{m1} from mode* 1 *to mode* m *for a wire with OSD, plotted against* L/l. $\eta \in [14.5932, 14.6282]$ *(6 steps). The averaging was done over 6 energies and 20 configurations.*

regular island only have an exponential tail that reaches into the disordered region, with the amount of flux in the tail roughly given by ξ_m^{-1}. The direct coupling between the first mode and another mode on the regular island is therefore on the order of $\xi_1^{-1}\xi_m^{-1}$. On the other hand, modes in the chaotic sea are not suppressed at the upper boundary, so that coupling between island modes and chaotic modes is of order ξ_m^{-1}. This leads to the same order of coupling for the two-step process of first tunneling to the chaotic sea (order ξ_1^{-1}) and then tunneling to mode m (order ξ_m^{-1}) as for direct coupling between island modes (order $\xi_1^{-1}\xi_m^{-1}$).

For the second process, the coupling between the first mode and the other modes actually proceeds in three steps: (1) Part of the right-moving island mode tunnels into the phase space region of the left-moving states at the upper side of the wire. (2) That part stays in the left-moving modes, propagating along the rough surface at the top of the wire. As the classical motion of the left-moving modes is purely chaotic (as seen in Fig. 5.7 for $v_x < 0$), there is strong intermode mixing. (3) The left-moving modes then couple to the right-moving modes on the bottom side of the wire. This coupling into the regular island should proceed with the same tunneling rate as the coupling from the island to the chaotic sea, i.e. directly proportional to ξ_m^{-1}.

Even though these two processes can interfere, the relative phase is random because of the chaoticity of phase space outside the regular island, so that we can simply perform an incoherent sum to obtain our result. Additionally, the

two processes are physically distinguishable. For example, the second (three-step) process could be observed by measuring the charge density at the rough side of the wire.

As long as the wire is shorter than the total localization length $\xi = \xi_1$, the transmission probability within the first mode will be almost one, $T_{11} \approx 1$. We are then interested in the flux within the chaotic region of phase space. As a first approximation, we assume that all flux in the chaotic region moves to the left without being scattered into a right-moving mode. This approximation can be justified by the fact that in the chaotic region of phase space we must have *directed chaos* [18]. The term "directed chaos" is used to refer to systems in which the time-averaged velocity of almost all chaotic trajectories approaches a non-zero constant v_{ch} for long times, which will be negative (i.e. directed to the left) in our system [18]. Another possibility to see this is that flux in the chaotic region will, on average, fill the chaotic region of phase space uniformly. A significant part of the right-moving part of phase space is occupied by the regular island, into which the chaotic modes can only enter by tunneling. This leads to an overall diffusion to the left for flux in the chaotic sea. In our simple model, we assume that all flux in the chaotic region moves to the left.

The total flux in the chaotic sea in module n (where n counts the number of modules from the left lead) is then given by the sum of the flux contributions that were reflected at a module position $n' > n$. For a given wire length L this is (with all lengths in units of l in this section, such that L is equal to the number of total modules in the wire)

$$P_{\mathrm{left}}(n) \approx \sum_{n'>n}^{L} \frac{1}{\xi_1} = \frac{L-n}{\xi_1}, \tag{5.24}$$

where we use that ξ_m^{-1} corresponds to the tunneling rate of the m-th mode out of the island (cf. Eq. (5.13)).

The fraction of the flux that tunnels into the right-moving mode m in the regular island at each module is then approximately $P_{\mathrm{left}}(n)/\xi_m + 1/(\xi_1\xi_m)$, where the second factor describes the direct coupling between the modes. To find the flux that arrives at the right lead, we have to sum over all fractions that tunnel into mode m at some point, weighted with the probability of transmission from n to L, which we just take as an exponential decay with ξ_m.

$$T_{m1} \approx \sum_{n=0}^{L} \frac{L-n+1}{\xi_1\xi_m} \exp\left(-\frac{L-n}{\xi_m}\right) \tag{5.25}$$

We can now distinguish between two cases: (1) If the wire length L is much smaller than the localization length ξ_m of the mode in question, we can set the

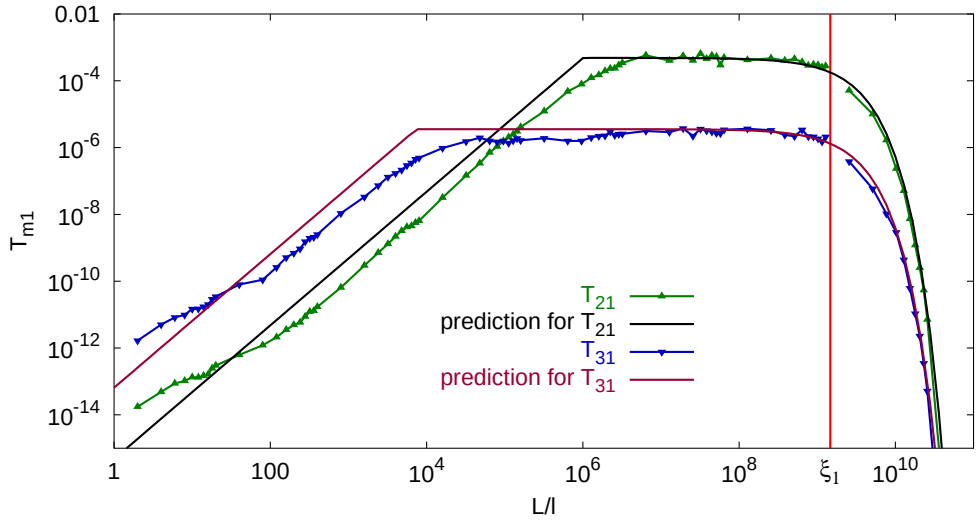

Figure 5.16: *T_{m1} together with predictions (Eqs. 5.26 and 5.28) from the model proposed by R. Ketzmerick. For wires in the localized regime ($L > \xi_1$), we show $\exp(\langle \ln T_{m1} \rangle)$, while for $L < \xi_1$, we show $\langle T_{m1} \rangle$. For $L \gg \xi_m$, the agreement of the data with the prediction (5.28) is excellent, for shorter wires the agreement with (5.26) is good. The only parameters that enter as fits are the ξ_m.*

exponential term in the sum to one and get (to highest order in L)

$$T_{m1} \approx \frac{L^2}{2\xi_1 \xi_m} \qquad L \ll \xi_m, \tag{5.26}$$

(2) alternatively, when the length L of the wire is much larger than ξ_m, we extend the sum to start at minus infinity, which will only add exponentially small terms. This leads to

$$T_{m1} \approx \frac{\xi_m}{\xi_1} \qquad \xi_m \ll L \ll \xi_1, \tag{5.27}$$

where we have assumed that $\xi_m \gg 1$, so that we only keep the leading term of the series expansion of our full result (not shown). For wires longer than the total localization length $\xi = \xi_1$, we realize that all the relevant dynamics takes place in a section of the wire of length $\approx \xi_m$. Since the localization length of mode $m > 1$ is much smaller than the localization length of the first mode, $\xi_m \ll \xi_1$, we expect that the transmission probabilities into higher modes just follow T_{11}, such that

$$T_{m1} \approx \frac{\xi_m}{\xi_1} \cdot T_{11} \approx \frac{\xi_m}{\xi_1} \cdot \exp\left(-\frac{L}{\xi_1}\right) \qquad L \gg \xi_m, \tag{5.28}$$

As the transmission probability of the first mode into itself is almost one for wires shorter than the localization length, $T_{11} \approx 1$, Eq. (5.28) can be used instead of Eq. (5.27) for all wire lengths $L \gg \xi_m$.

Our simple model predicts that the transmission probability from the first mode to the m-th mode on the regular island will at first increase quadratically with the length of the wire until the wire is as long as the localization length ξ_m of the m-th mode. At that point, the transmission is predicted to saturate at a value given by the ratio of the two localization lengths ξ_m and ξ_1, until the wire is long enough that the localized regime is entered, where T_{m1} follows the exponential decrease of T_{11}.

Note that this model does not include any separate fit parameters. The localization lengths ξ_m are obtained by fitting to the exponential decay of the transmission probabilities T_m of the individual modes, which have no direct connection to the model discussed here.

For comparison of the predictions to the numerical results, it is important which average is taken. Since T_{m1} is closely coupled to T_{11}, we assume that its distribution is the same as that for T_{11}. For wires in the localized regime ($L \gg \xi_1$), the T_{m1} should then be log-normally distributed, such that $\exp(\langle \ln T_{m1} \rangle)$ is the correct average. For shorter wires, the T_{m1} should follow a Rayleigh distribution [12], such that $\langle T_{m1} \rangle$ is the more appropriate average.

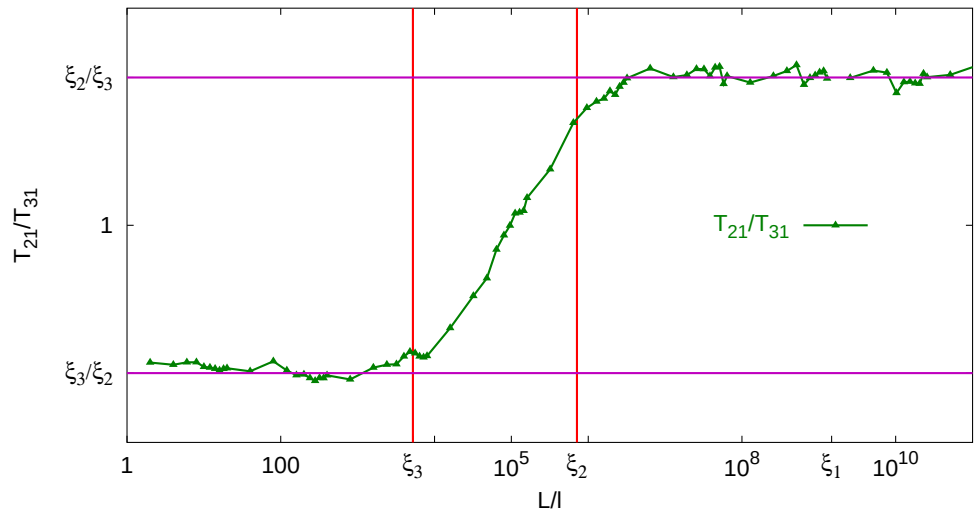

Figure 5.17: *Ratio T_{21}/T_{31} compared to the predictions Eq. (5.29) and Eq. (5.30). The agreement is excellent. As before, we use $\langle T_{m1} \rangle$ for wires shorter than the localization length and $\exp(\langle \ln T_{m1} \rangle)$ for longer wires. As in Fig. 5.16, the only parameters that enter as fits are the ξ_m.*

In Fig. 5.16, our fit-parameter free prediction is compared to the numerical results for the probabilities T_{21} (T_{31}) for transmission from the first to the second (third) mode, which are still well inside the regular island for the parameters used (cf. Fig. 5.8). As can clearly be observed, our simple model captures the essential dynamics and predicts the correct behavior for the T_{m1}.

In particular, the ratio of transmission into two different modes on the regular island is predicted to behave in the following way,

$$\frac{T_{n1}}{T_{m1}} = \frac{\xi_m}{\xi_n} \qquad L \ll \xi_m, \xi_n, \tag{5.29}$$

$$\frac{T_{n1}}{T_{m1}} = \frac{\xi_n}{\xi_m} \qquad L \gg \xi_m, \xi_n. \tag{5.30}$$

In Fig. 5.17, we show that the ratio between the transmission probabilities T_{21} and T_{31} does indeed display the behavior predicted by our model. The agreement is remarkably good. Compared to Fig. 5.16, the quantitative agreement is improved since any common prefactors that we neglected in our simple model drop out.

Chapter 6

Analytical calculations

In this chapter we perform some analytical calculations with the aim of deriving an expression for the localization length ξ in the quasi-classical regime, i.e. for large Fermi momentum k_F. Since we will extensively use the properties of the transverse modes in a perfect lead, we first discuss these modes and their properties in some detail[1]. Following that, we employ their properties, together with a WKB approximation, in the derivation of the analytical expression Eq. (5.18) [Eq. (5.22)] for the localization length ξ in the limit of large k_F with constant cyclotron radius r_c [constant magnetic field strength B].

6.1 Transverse modes in a perfect lead

To investigate the properties of the transverse modes in an infinitely long perfect lead subject to a perpendicular magnetic field in the negative z-direction ($\mathbf{B} = -B\,\hat{\mathbf{z}}$), we derive the effective Hamiltonian H^y that, together with the boundary conditions, determines their properties. We start from the Hamiltonian of a free particle in the lead, using the Landau gauge as in Eq. (3.11) ($\mathbf{A} = By\,\hat{\mathbf{x}}$),

$$H = \frac{1}{2}\left(\mathbf{p} + \frac{1}{c}\mathbf{A}\right)^2, \tag{6.1a}$$

$$H = \frac{1}{2}\left(p_x^2 + p_y^2 + 2\frac{B}{c}yp_x + \frac{B^2}{c^2}y^2\right). \tag{6.1b}$$

The Hamiltonian H still commutes with the longitudinal momentum p_x, $[H, p_x] = 0$, irrespective of the term containing a product of y and p_x, as $[y, p_x] = 0$. This means that the wave function can be separated into a transverse and a longitudinal part even in the presence of a magnetic field,

$$\phi(x, y) = \chi(y)\exp(ik_x x). \tag{6.2}$$

[1] Where we repeat some parts of section 3.2 for clarity.

Note that the separability of the Hamiltonian depends on the specific gauge. By choosing the Landau gauge we ensure that k_x remains a constant of motion in the disorder-free lead.

For clarity we mention that $\mathbf{p}$ is the *canonical* momentum, which in this case does not correspond to the *kinetic* momentum $\mathbf{p}_{\text{kin}} = \mathbf{p} + \mathbf{A}/c$. Note that the energy of a free particle does not depend on the magnetic field, such that only the kinetic momentum enters into the energy, i.e. $E_{\text{kin}} = \mathbf{p}_{\text{kin}}^2/2$. On the other hand, the quantum mechanical commutation rules (and therefore the correspondence principles) are valid for the canonical, not for the kinetic momentum.

Inserting the factorized wave function (6.2) into the Schrödinger equation $H\phi = E_F\phi$ and dividing by $\exp(ik_x x)$, we obtain

$$\frac{1}{2}\left[k_x^2 + p_y^2 + 2\frac{B}{c}yk_x + \frac{B^2}{c^2}y^2\right]\chi(y) = E_F\chi(y), \tag{6.3}$$

$$\left[\frac{p_y^2}{2} + \frac{B^2}{2c^2}\left(\frac{ck_x}{B} + y\right)^2 - E_F\right]\chi(y) = 0. \tag{6.4}$$

Inserting the cyclotron radius $r_c = ck_F/B$,

$$\left[\frac{p_y^2}{2} + \frac{k_F^2}{2r_c^2}\left(\frac{r_c k_x}{k_F} + y\right)^2 - E_F\right]\chi(y) = 0. \tag{6.5}$$

Using $E_F = k_F^2/2$ and defining $y_0 = -r_c k_x/k_F$, we finally arrive at

$$\left[\frac{p_y^2}{2} + E_F\left(\left(\frac{y - y_0}{r_c}\right)^2 - 1\right)\right]\chi(y) = 0, \tag{6.6}$$

$$H^y_{(E_F,y_0)}\chi(y) = 0. \tag{6.7}$$

The transverse wave function satisfies an effective Schrödinger equation for a particle at energy $E = 0$ in a quadratic potential that has a minimum at $y_0 = -r_c k_x/k_F$. In other words, the longitudinal canonical momentum determines the potential that the transverse wave function is subject to. By imposing boundary conditions, $\chi(y=0) = \chi(y=w) = 0$, we find that solutions only exist for certain values $k_{x,n}$, or equivalently, $y_{0,n}$.

From the mirror symmetry of the system around $y = w/2$ follows that for each $y_{0,n}^+ < w/2$, there must also be a solution at the same energy with $y_{0,n}^- = w - y_{0,n}^+$. If we rewrite this condition for the $k_{x,n}$, we find that $k_{x,n}^- = -k_F w/r_c - k_{x,n}^+$. If we had chosen our wire to be symmetric around $y = 0$, this condition would have simplified to $k_{x,n}^- = -k_{x,n}^+$. However, since we later want to connect two leads with different widths but smooth lower boundary (see Fig. 6.2), this choice of coordinates would only be convenient for one of the two leads.

6.1.1 Orthogonality condition

Because of the magnetic field, the transverse eigenstates in the leads *do not* satisfy the usual orthogonality relation

$$\int_0^w \chi_n^*(y)\chi_m(y)\mathrm{d}y = \delta_{nm}. \tag{6.8}$$

Instead, they satisfy a relation that can be derived from current conservation for the flux-carrying modes [36], but also follows from application of Sturm-Liouville analysis to Eq. (6.7) [51],

$$(k_{x,n}^{\pm} - k_{x,m}^{\pm})I_{n\pm,m\pm} = 0, \tag{6.9a}$$

$$I_{n\pm,m\pm} \equiv \int_0^w \left(k_{x,n}^{\pm} + k_{x,m}^{\pm} + 2k_F\frac{y}{r_c}\right)\chi_n^{\pm}(y)\chi_m^{\pm}(y)\mathrm{d}y. \tag{6.9b}$$

From this follows that the integral $I_{n\pm,m\pm}$ satisfies

$$I_{n\pm,m\pm} = \pm\delta_{nm}, \tag{6.10}$$

assuming that the wave functions are normalized such that each flux-carrying mode carries unit flux, which was the requirement to have a unitary scattering matrix. For notational simplicity, we have absorbed the normalization factors θ used in earlier chapters into the wave functions χ and normalize these to unit flux directly.

6.2 Calculation of the localization length ξ

Our goal in this chapter is to find an analytical expression for the localization length ξ for the case of the one-sided rough wire. As we have seen, the total localization length ξ is identical to the localization length ξ_1 of the lowest mode. We proceed by calculating the coefficients for transport by the first mode at each junction of two modules and then connect these scattering amplitudes to get the total transmission of the first mode.

The total transmission matrix t^c of a system created by connecting two subsystems (1 and 2) can be calculated from the transmission and reflection matrices t^1, t^2, r'^1, r^2 of the two subsystems, where t^i is the transmission matrix from left to right and r^i (r'^i) is the reflection matrix for a particle incident from the left (right) (cf. Fig. 6.1). The transmission matrix of the combined system is given by $t^c = t^2(1 - r'^1 r^2)^{-1}t^1$, which we rewrite to

$$t^c = t^2\left[\sum_{n=0}^{\infty}\left(r'^1 r^2\right)^n\right]t^1 = t^2t^1 + t^2r'^1r^2t^1 + \dots . \tag{6.11}$$

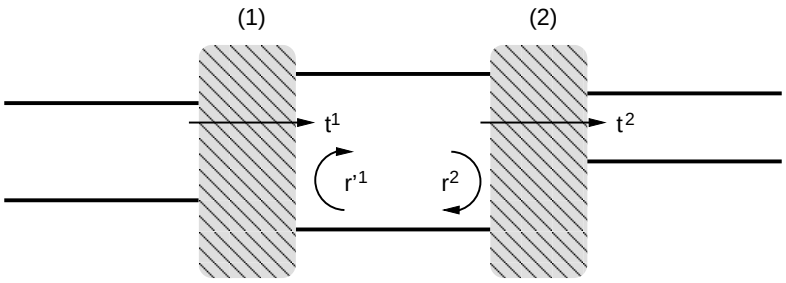

Figure 6.1: *Connecting two systems. Transmission proceeds by transmission through the first system (t^1), an arbitrary number of reflections between the two systems (each of which gives a term $r'^1 r^2$) and then transmission through the second system (t^2). This leads to Eq. (6.11).*

The transmission of the whole system is now given by the coherent sum of an infinite number of terms, where each term can be given a simple physical interpretation. We have to read each term right to left: The first term corresponds to direct transmission through both subsystems. In the second term, the wave is transmitted through the first system, then reflected in the second system, again reflected in the first system, and then finally makes its way out through the second system. The additional terms describe the same process with an increasing number of reflections inside the system. For the transmission of the first mode, we neglect all terms featuring reflection coefficients since they involve two tunneling processes – out of the regular island for the first reflection and then back into the regular island. This leaves us with

$$t^c_{11} \approx t^2 t^1 = \sum_{m=1}^{N_2} t^2_{1m} t^1_{m1}, \tag{6.12}$$

where N_2 is the number of modes at the junction of the two systems. The m-th term describes transmission from the first mode to the m-th mode at the first junction and then transmission from the m-th mode to the first mode at the second junction. We drop all but the first term, which amounts to neglecting contributions from tunneling to another mode and then back to the first mode. These contributions will be very small for those modes m that are on the regular island, while for modes in the chaotic part of phase space the contributions will be of order $O(\varepsilon)$ (with $t_{11} = 1 - \varepsilon$ as defined below). Since their phases are random, though, they tend to average out, so that we neglect them.

Thus, we find that for transmission across two module junctions the transmission of the first mode into itself is

$$t^c_{11} \approx t^2_{11} t^1_{11}, \tag{6.13}$$

This implies that t_{11} of the whole wire composed of N modules will be approximately

$$t_{11} \approx \prod_{i=0}^{N} t_{11}^{(i,i+1)}, \tag{6.14}$$

where $t^{(i,i+1)}$ is the transmission matrix from module i to module $i+1$, with $i = 0$ and $i = N+1$ labeling the left and right leads, respectively. Since the transverse wave functions of the first mode only have an exponential tail that reaches the upper boundary, we expect that $t_{11}^{(i,i+1)}$ will be almost one, so that we write (neglecting phases)

$$t_{11}^{(i,i+1)} = 1 - \varepsilon_{(i,i+1)}. \tag{6.15}$$

Additionally, from the Onsager-Casimir symmetry relations follows that the transmission t_{11} only depends on the two heights h_i and h_{i+1}, but not on their ordering, i.e. it does not matter whether the first or the second module has the greater height. Using this fact and recognizing that $t_{11}^{(i,i+1)}$ will depend mostly on the height of the lower of the two modules, we have

$$t_{11}^{(i,i+1)} \approx t_{11}^{\min(h_i,h_{i+1})}. \tag{6.16}$$

In this equation we have neglected the case that both modules are of equal height (where $t_{11} = 1$), and Eq. (6.14) becomes

$$t_{11} \approx \prod_{i=0}^{N} t_{11}^{(i,i+1)} \approx \prod_{j=1}^{M} \left(t_{11}^{h_j}\right)^{NP_j}, \tag{6.17}$$

where M is the number of distinct modules we use and P_j is the probability that a module with height h_j occurs as the lower of two adjacent modules. Rearranging terms, we get the following expression for t_{11}:

$$t_{11} \approx \prod_{j=1}^{M} \left(1 - \varepsilon_{h_j}\right)^{NP_j} \approx \exp(-N \sum_{j=1}^{M} P_j \varepsilon_{h_j}). \tag{6.18}$$

Considering that in our system the modules are always arranged in permutations, i.e. that the same module never occurs twice in a row, the probability $P_{i,j}$ of finding modules with height h_i and h_j in sequence is

$$P_{i,j} = \frac{1}{M(M-1)}. \tag{6.19}$$

With the supermodule method, the modules indeed only occur in permutations, with the exception of the boundaries of the supermodules, where it is possible that the same module appears twice in a row. The small correction to $P_{i,j}$ caused by this can be safely neglected, though.

The probability that a module with height h_i is the lower of a pair of modules is then given by

$$P_j = \sum_{i=j+1}^{M} 2P_{i,j} = \frac{2(M-j)}{M(M-1)}, \tag{6.20}$$

where the factor 2 occurs because we do not distinguish which module comes first.

We use again that the first mode is exponentially suppressed at the upper boundary, from which follows that ε_{h_1} belonging to the module with the lowest height is the dominant contribution in the above sum. Neglecting all other contributions and inserting the explicit expression (6.20) for P_j, t_{11} is simply given by

$$t_{11} \approx \exp\left(-2NP_1\varepsilon_{h_1}\right) = \exp\left(-\frac{2L}{Ml}\varepsilon_{h_1}\right). \tag{6.21}$$

For very long one-sided rough wires the conductance $g \approx |t_{11}|^2$ decays according to $g \propto \exp(-L/\xi)$, allowing us to extract the localization length ξ as

$$\xi \approx \frac{Ml}{4\varepsilon_{h_1}}. \tag{6.22}$$

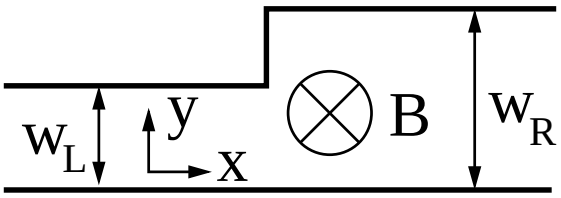

Figure 6.2: *Two leads*

To determine ε_{h_1} we require an expression for the transmission amplitude t_{11} from one module to the next. To calculate this quantity, we consider the simple system of two leads of different width w_L, w_R shown in Fig. 6.2, with a wave coming in from the left in the first mode. The wave functions Ψ^L in the left lead and Ψ^R in the right lead are given by

$$\Psi^L(x,y) = \phi_1^{L+}(x,y) + \sum_{m=1}^{\infty} r_{m1}\phi_m^{L-}(x,y), \tag{6.23}$$

$$\Psi^R(x,y) = \sum_{m=1}^{\infty} t_{m1}\phi_m^{R+}(x,y), \tag{6.24}$$

where

$$\phi_m^{S\pm}(x,y) = \chi_n^{S\pm}(y)\exp\left(ik_{x,n}^{S\pm}x\right). \tag{6.25}$$

We now continue our calculation of t_{11} by matching wave functions at $x = 0$. This demands that

$$\begin{aligned} \Psi^L(x{=}0, y) &= \Psi^R(x{=}0, y), \\ \chi_1^{L+}(y) + \sum_{m=1}^{\infty} r_{m1}\chi_m^{L-}(y) &= \sum_{m=1}^{\infty} t_{m1}\chi_m^{R+}(y), \end{aligned} \tag{6.26}$$

and

$$\begin{aligned} \frac{\partial\Psi^L}{\partial x}(x{=}0, y) &= \frac{\partial\Psi^R}{\partial x}(x{=}0, y), \\ k_{x,1}^{L+}\chi_1^{L+}(y) + \sum_{m=1}^{\infty} r_{m1}k_{x,m}^{L-}\chi_m^{L-}(y) &= \sum_{m=1}^{\infty} t_{m1}k_{x,m}^{R+}\chi_m^{R+}(y). \end{aligned} \tag{6.27}$$

In order to extract t_{11}, we multiply Eq. (6.26) by $(k_{x,1}^{R+} + 2k_F y/r_c)$ and add it to Eq. (6.27). This then gives

$$\begin{aligned} \left(k_{x,1}^{L+} + k_{x,1}^{R+} + 2k_F\frac{y}{r_c}\right)\chi_1^{L+}(y) + \sum_{m=1}^{\infty} r_{m1}\left(k_{x,m}^{L-} + k_{x,1}^{R+} + 2k_F\frac{y}{r_c}\right)\chi_m^{L-}(y) = \\ = \sum_{m=1}^{\infty} t_{m1}\left(k_{x,m}^{R+} + k_{x,1}^{R+} + 2k_F\frac{y}{r_c}\right)\chi_m^{R+}(y). \end{aligned} \tag{6.28}$$

We multiply this equation by $\chi_1^{R+}(y)$ and integrate from $y = 0$ to $y = \infty$. In this way, the right hand side reduces to the generalized orthogonality relation (6.9) for the transverse wave functions in the lead. Therefore, the right hand side simplifies to t_{11} after evaluation of the integral and we find

$$\begin{aligned} t_{11} &= t_{11}^A + t_{11}^B, \\ t_{11}^A &= \int_0^{w_<} \left(k_{x,1}^{L+} + k_{x,1}^{R+} + 2k_F\frac{y}{r_c}\right)\chi_1^{L+}(y)\chi_1^{R+}(y)\mathrm{d}y, \\ t_{11}^B &= \int_0^{w_<} \sum_{m=1}^{\infty} r_{m1}\left(k_{x,m}^{L-} + k_{x,1}^{R+} + 2k_F\frac{y}{r_c}\right)\chi_m^{L-}(y)\chi_1^{R+}(y)\mathrm{d}y. \end{aligned} \tag{6.29}$$

where $w_<$ is the smaller of the two lead widths w_L, w_R. For sufficiently high magnetic field B and Fermi energy k_F, the wave functions in the first mode are almost equal, so that we expect t_{11}^A to be almost one and define

$$t_{11}^A \equiv 1 - \varepsilon_A. \tag{6.30}$$

The second term (t_{11}^B) can be estimated to be of order $O(\varepsilon_A)$ by realizing that the unitarity constraint fixes the r_{m1} to be of $O(\sqrt{\varepsilon})$ for the flux-carrying modes. We insert $t_{11} = 1 - \varepsilon$ into the unitarity condition

$$1 = \sum_{m=1}^{N} \left(|t_{m1}|^2 + |r_{m1}|^2 \right), \tag{6.31}$$

$$2\varepsilon = \sum_{m=2}^{N} |t_{m1}|^2 + \sum_{m=1}^{N} |r_{m1}|^2, \tag{6.32}$$

and obtain that the r_{m1} must be $O(\sqrt{\varepsilon})$. The integrals in t_{11}^B approximately correspond to the orthogonality condition (6.9), so that they are very small. They can be estimated to be of order $O(\sqrt{\varepsilon})$ by using that the difference between the first modes on the left and right side is of order $O(\sqrt{\varepsilon})$, while the left-moving modes are of order $O(1)$ at the upper side of the wire, where $\chi_1^{R+}(y)$ differs from $\chi_1^{L+}(y)$. Utilizing that the integral and r_{m1} are both $O(\sqrt{\varepsilon})$, the whole term should be of order $O(\varepsilon)$. Still, the analytical evaluation of this term remains a challenge as it contains the factors r_{m1} for which no closed analytical solution is known. To investigate the importance of t_{11}^B as compared to t_{11}^A, the numerical simulation of the system of two leads with the MRGM was employed to calculate these two terms. We find that the magnitude of t_{11}^B is about $0.2\varepsilon_A$, quite independent of the Fermi energy E_F and the magnetic field B. We thus neglect t_{11}^B in the following, keeping in mind that this will introduce an error of about 20% in our result for the localization length.

From the Onsager-Casimir relations (2.11a) follows that the transmission amplitude t_{11} from the first mode to the first mode will be independent of whether we go from a wide lead to a narrow lead or vice versa. This follows from the fact that transmission from a lead with width w_1 to a lead with width w_2 can be described either by (1) injection from the left with magnetic field $\mathbf{B} = -B\,\hat{\mathbf{z}}$ in a system with lead widths $w_L = w_1$ and $w_R = w_2$ or by (2) injection from the right at $\mathbf{B} = B\,\hat{\mathbf{z}}$ in a system with lead widths $w_L = w_2$ and $w_R = w_1$. Since both system (1) and system (2) describe the same physical situation, it follows that t_{11} (transmission from the first mode on the left to the first mode on the right) of system (1) is equal to t'_{11} (transmission from the first mode on the right to the first mode on the left) of system (2). Eq. (2.11a) then states that for system (2),

$$t_{11}(-B\,\hat{\mathbf{z}}) = t'_{11}(B\,\hat{\mathbf{z}}), \tag{6.33}$$

so that t_{11} is proven to be the same for transmission from a wide to a narrow lead as for transmission from a narrow to a wide lead. This is illustrated in Fig. 6.3.

Since t_{11}^A just contains the product of the two first transverse modes, it is also independent of the order of the leads. From this follows that t_{11}^B is also invariant with respect to an exchange of the leads. Without loss of generality, we can therefore choose $w_L < w_R$ for the further calculation.

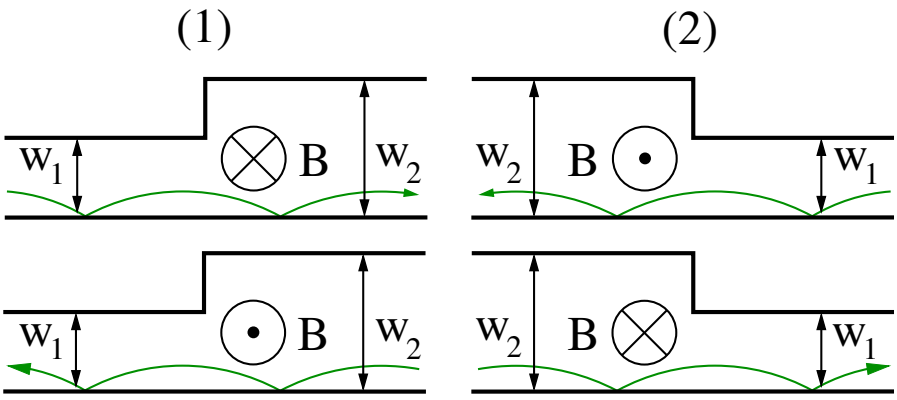

Figure 6.3: *Illustration of the Onsager-Casimir relations and symmetry considerations. Systems (1) and (2) are equivalent, $t_{mn}(1) = t'_{mn}(2)$, they just correspond to looking at the same problem from the $-z$ and z-direction, respectively. The upper row is connected to the lower row by the Onsager-Casimir relations (2.11a). This leads to t_{11} for the upper left system being equal to t_{11} for the lower right system, i.e. t_{11} is invariant whether we go from a wide to a narrow or from a narrow to a wide lead.*

Since the first mode in the (wider) right lead "feels" the upper boundary exponentially less than the first mode in the (narrower) left lead, we replace it by the wave function of the first transverse mode in an infinitely wide lead,

$$\chi_1^{R+}(y) \approx \chi_1^{\infty+}(y). \tag{6.34}$$

We then write the wave function in the left lead as

$$\chi_1^{L+}(y) = N' \left(\chi_1^{\infty+}(y) - \sigma(y) \right), \tag{6.35}$$

and the longitudinal momentum as

$$k_{x,1}^{L+} = k_{x,1}^{\infty+} + \Delta k_x, \tag{6.36}$$

where $\sigma(y)$ is negligible except near $y = w_L$ and is given by $\sigma(y) = \chi_1^{\infty+}(y)$ for $y > w_L$, such that $\chi_1^{L+}(y) = 0$ in that region. N' is a normalization factor, which will be close to one. The change in the longitudinal momentum Δk_x imposed by a change in the lead width is very small, and is numerically found to be $O(\varepsilon_A)$. In Fig. 6.4, we sketch $\chi_1^{\infty+}(y)$ and $\sigma(y)$.

Inserting (6.35) and (6.36) into Eq. (6.29) and extending the integral to $y = \infty$

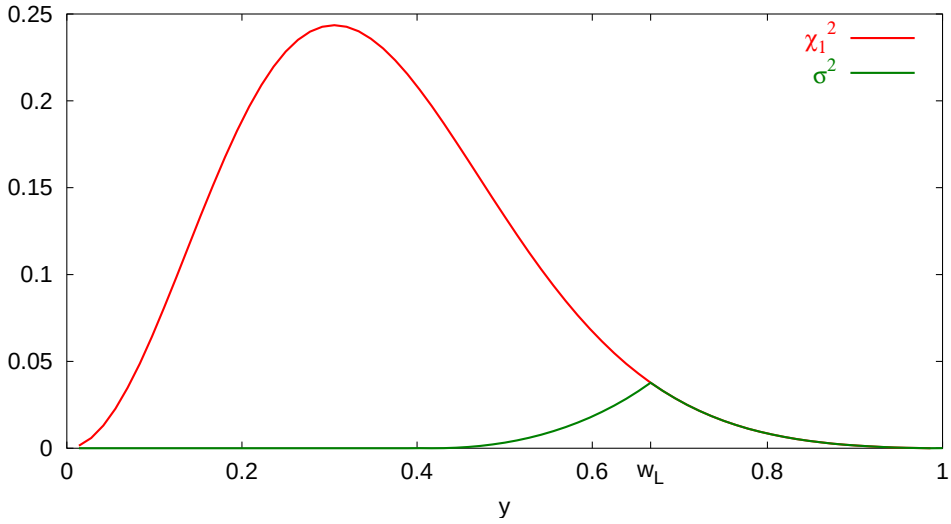

Figure 6.4: *Sketch of the wave function in an infinite lead* $\chi_1^{\infty+}(y)$ *and the correction* $\sigma(y)$ *for finite lead width* w_L*. This plot is done at sufficiently low energy to ensure that* σ *is visible with a linear scale.*

(considering that the wave function on the left is zero for $y > w_L$), we have

$$t_{11}^A = \int_0^\infty \left(2k_{x,1}^{\infty+} + \Delta k_x + 2k_F \frac{y}{r_c}\right) N' \left(\chi_1^{\infty+}(y) - \sigma(y)\right) \chi_1^{\infty+}(y) \mathrm{d}y, \tag{6.37}$$

$$\begin{aligned} t_{11}^A = N' \Bigg[1 - \underbrace{\int_0^\infty \left(2k_{x,1}^{\infty+} + 2k_F \frac{y}{r_c}\right) \sigma(y) \chi_1^{\infty+}(y) \mathrm{d}y}_{A} + \\ + \Delta k_x \underbrace{\int_0^\infty \left(\chi_1^{\infty+}(y) - \sigma(y)\right) \chi_1^{\infty+}(y) \mathrm{d}y}_{B} \Bigg]. \end{aligned} \tag{6.38}$$

For simplicity of notation, we name the two above integrals A and B, such that

$$t_{11}^A = N' \left[1 - A + \Delta k_x B\right]. \tag{6.39}$$

To calculate N', we use the flux normalization condition from Eq. (6.10),

$$1 = N'^2 \int_0^\infty \left(2k_{x,1}^{\infty+} + 2\Delta k_x + 2k_F \frac{y}{r_c}\right) \left(\chi_1^{\infty+}(y) - \sigma(y)\right)^2, \tag{6.40}$$

$$\begin{aligned} 1 = N'^2 \Bigg[1 - 2 \underbrace{\int_0^\infty \left(2k_{x,1}^{\infty+} + 2k_F \frac{y}{r_c}\right) \sigma(y)\chi_1^{\infty+}(y)\mathrm{d}y}_{A} + \\ + \underbrace{\int_0^\infty \left(2k_{x,1}^{\infty+} + 2k_F \frac{y}{r_c}\right) \sigma(y)^2 \mathrm{d}y}_{C} + \\ + 2\Delta k_x \underbrace{\int_0^\infty \left(\chi_1^{\infty+}(y) - \sigma(y)\right)^2 \mathrm{d}y}_{B'} \Bigg]. \end{aligned} \tag{6.41}$$

Introducing the short-hand notation C and B' for the two last integrals in the above equation, we can write

$$1 = N'^2 \left[1 - 2A + C + 2\Delta k_x B'\right]. \tag{6.42}$$

Inserting this into our formula for t_{11}^A, we obtain

$$t_{11}^A = \frac{1 - A + \Delta k_x B}{\sqrt{1 - 2A + 2\Delta k_x B' + C}}. \tag{6.43}$$

Since all the integrals A-C are much smaller than one, we expand the square root into a Taylor series and only keep terms to the first order,

$$t_{11}^A \approx (1 - A + \Delta k_x B)\left(1 + A - \Delta k_x B' - \frac{1}{2}C\right), \tag{6.44}$$

$$t_{11}^A \approx 1 - \frac{1}{2}C + \Delta k_x \left(B - B'\right). \tag{6.45}$$

Inserting the expressions for B and B', the second term becomes

$$\Delta k_x (B - B') = \Delta k_x \int_0^\infty \left(\chi_1^{\infty+}(y)\sigma(y) - \sigma(y)^2\right) \mathrm{d}y, \tag{6.46}$$

which is of higher order than integral C since $\sigma(y)$ is almost zero where the wave function has its maximum and Δk_x is already $O(\varepsilon_A)$. Dropping this term, we arrive

at a simple expression for t_{11}^A, or equivalently ε_A, to first order:

$$t_{11}^A \approx 1 - \int_0^\infty \left(k_{x,1}^{\infty+} + k_F \frac{y}{r_c}\right) \sigma(y)^2 \mathrm{d}y, \tag{6.47a}$$

$$\varepsilon_A \approx \int_0^\infty \left(k_{x,1}^{\infty+} + k_F \frac{y}{r_c}\right) \sigma(y)^2 \mathrm{d}y. \tag{6.47b}$$

To calculate this integral, we need an expression for $\sigma(y)$. By inserting Eq. (6.35) into Eq. (6.7) and imposing the boundary conditions $\chi_1^{L+}(y=0) = \chi_1^{L+}(y=w_L) = 0$, we find that $\sigma(y)$ has to be an eigenfunction of the same Hamiltonian H^y as $\chi_1^{L+}(y)$, but with boundary conditions $\sigma(0) = \sigma(\infty) = 0$ and $\sigma(w_L) = \chi_1^{\infty+}(w_L)$. Since the upper boundary w_L is already deep in the classically forbidden region, we use a WKB approximation (see chapter 7 in [67]) for our solution for $\sigma(y)$.

$$\sigma(y) = \chi_1^{\infty+}(w_L)\sqrt{\frac{\rho(w_L)}{\rho(y)}} \times \begin{cases} \exp\left(-\int_y^{w_L} \rho(y')\mathrm{d}y'\right) & y < w_L \\ \exp\left(-\int_{w_L}^{y} \rho(y')\mathrm{d}y'\right) & y > w_L \end{cases}, \tag{6.48}$$

$$\rho(y) = \sqrt{2[V(y) - E]} = k_F\sqrt{V(y)/E_F}, \tag{6.49}$$

where we have used that the effective 1D Schrödinger equation has eigenvalue $E = 0$ (cf. Eq. (6.7)). Inserting the above expression into Eq. (6.47a), we find

$$\varepsilon_A = \left[\chi_1^{\infty+}(w_L)\right]^2 \left[\int_0^{w_L} \left(k_{x,1}^{\infty+} + k_F \frac{y}{r_c}\right) \frac{\exp\left(-2\int_y^{w_L} \rho(y')\mathrm{d}y'\right)}{\rho(y)/\rho(w_L)} \mathrm{d}y + \right.$$
$$\left. + \int_{w_L}^\infty \left(k_{x,1}^{\infty+} + k_F \frac{y}{r_c}\right) \frac{\exp\left(-2\int_{w_L}^{y} \rho(y')\mathrm{d}y'\right)}{\rho(y)/\rho(w_L)} \mathrm{d}y \right]. \tag{6.50}$$

We extend the first integral to start at negative infinity and perform the substitutions $z' = w_L - y'$, $z = w_L - y$ in the first integral, and similar substitutions

$z' = y' - w_L$, $z = y - w_L$ in the second integral. This leads to

$$\varepsilon_A = \left(\chi_1^{\infty+}(w_L)\right)^2 \left[\int_0^\infty \left(k_{x,1}^{\infty+} + k_F \frac{w_L - z}{r_c} \right) \frac{\exp\left(-2 \int_0^z \rho(w_L - z')\mathrm{d}z' \right)}{\rho(w_L - z)/\rho(w_L)} \mathrm{d}z + \right.$$
$$\left. + \int_0^\infty \left(k_{x,1}^{\infty+} + k_F \frac{w_L + z}{r_c} \right) \frac{\exp\left(-2 \int_0^z \rho(w_L + z')\mathrm{d}z' \right)}{\rho(w_L + z)/\rho(w_L)} \mathrm{d}z \right]. \quad (6.51)$$

Since the integral will only give a significant contribution near $y = w_L$, i.e. $z = 0$, we expand $\rho(y)$ into a Taylor series to first order,

$$\rho(w_L + z) \approx \rho(w_L) + \rho'(w_L) z. \quad (6.52)$$

Defining $\rho \equiv \rho(w_L)$, $\rho' \equiv \rho'(w_L)$ and $\chi_1^{\infty+} \equiv \chi_1^{\infty+}(w_L)$, we find

$$\varepsilon_A = \left(\chi_1^{\infty+}\right)^2 \int_0^\infty \mathrm{d}z \exp\left(-2\rho z\right) \times$$
$$\left[\left(k_{x,1}^{\infty+} + k_F \frac{w_L - z}{r_c} \right) \frac{\exp\left(\rho' z^2\right)}{1 - z\rho'/\rho} + \left(k_{x,1}^{\infty+} + k_F \frac{w_L + z}{r_c} \right) \frac{\exp\left(-\rho' z^2\right)}{1 + z\rho'/\rho} \right]. \quad (6.53)$$

Expanding the term in square brackets in powers of z gives

$$[\ldots] = 2 \left(k_{x,1}^{\infty+} + \frac{k_F w_L}{r_c} \right) + O(z^2). \quad (6.54)$$

Dropping the quadratic term, the evaluation of the integral becomes trivial and leads to

$$\varepsilon_A = \frac{\left(\chi_1^{\infty+}\right)^2}{\rho} \left(k_{x,1}^{\infty+} + \frac{k_F w_L}{r_c} \right), \quad (6.55)$$

with $\chi_1^{\infty+}$ and ρ both evaluated at $y = w_L$. The next step in our calculation of ε_A, and, ultimately, of the localization length ξ, is to find an expression for the value of the transverse wave function $\chi_1^{\infty+}(w_L)$ and for the longitudinal momentum eigenvalue $k_{x,1}^{\infty+}$.

To do this, we rewrite the effective transverse Hamiltonian H^y, following from

Eq. (6.7), defining $y_z = y_0 + r_c$:

$$H^y = \frac{p_y^2}{2} + E_F \left[\left(\frac{y - y_0}{r_c} \right)^2 - 1 \right], \tag{6.56a}$$

$$H^y = \frac{p_y^2}{2} + \frac{k_F^2}{2} \left[\left(\frac{y - y_z}{r_c} \right)^2 + 2\frac{y - y_z}{r_c} \right], \tag{6.56b}$$

$$H^y = \frac{p_y^2}{2} + V(y), \tag{6.56c}$$

where $V(y_z) = 0$. Since the WKB solution diverges near the classical turning point, we linearize the potential in this region (i.e. drop the quadratic term), which makes it possible to solve the effective Schrödinger equation analytically. This is a standard procedure in WKB to connect the classically allowed and forbidden regions, which goes back to Langer [67, 68]. The complete wave function is thus constructed by connecting the solution of the linearized potential near the classical turning point to the WKB solution in the classically forbidden region.

Performing the linearization and substituting $z = (2k_F^2/r_c)^{1/3}(y - y_z)$ simplifies the Schrödinger equation $H^y\chi(y) = 0$ to

$$\left(\frac{\partial^2}{\partial z^2} - z \right) \chi(z) = 0. \tag{6.57}$$

This equation is known as Airy's differential equation and has two linearly independent solutions, $\mathrm{Ai}(z)$ and $\mathrm{Bi}(z)$. As $\mathrm{Bi}(z)$ diverges exponentially for large z, the solution satisfying our boundary conditions only contains $\mathrm{Ai}(z)$, which is shown in Fig. 6.5. It is defined by

$$\mathrm{Ai}(z) = \frac{1}{\pi} \int_0^\infty \mathrm{d}t \cos\left(\frac{1}{3}t^3 + zt \right). \tag{6.58}$$

The boundary condition at the lower wall demands that $\chi(y{=}0)$ is equal to zero, so that $z(y = 0)$ must be a zero of the Airy function $\mathrm{Ai}(z)$. Since we want the solution for the first mode, we choose the first zero at $z = Ai_0 \approx -2.338$ (indicated in Fig. 6.5), such that the wave function has no zeros apart from these at the boundaries. From this follows that

$$y_z = -\left(\frac{r_c}{2k_F^2} \right)^{1/3} Ai_0, \tag{6.59}$$

$$z = Ai_0 + \left(\frac{2k_F^2}{r_c} \right)^{1/3} y, \tag{6.60}$$

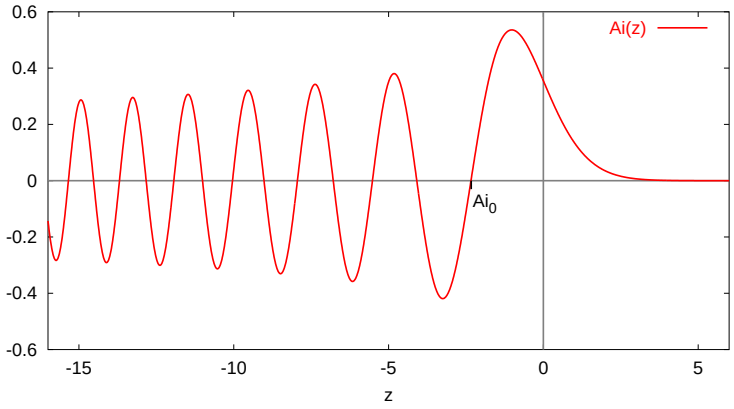

Figure 6.5: *Airy Function* $\mathrm{Ai}(z)$ *in the range* $z \in [-16; 6]$.

or, inserting $y_z = y_0 + r_c$ and then $y_0 = -r_c k_x / k_F$ into Eq. (6.59),

$$k_{x,1}^{\infty+} = k_F \left[1 + \frac{Ai_0}{2^{1/3}} \left(k_F r_c \right)^{-2/3} \right]. \tag{6.61}$$

We thus see that the longitudinal momentum of the first mode $k_{x,1}^{\infty+}$ is only marginally smaller than the Fermi momentum k_F for large k_F (remember that Ai_0 is negative). The maximum of the first transverse mode is between $z = Ai_0$ and $z = 0$ (cf. Fig. 6.5), i.e. between $y = 0$ and $y = y_z$. Since y_z approaches $y = 0$ for large k_F, the wave function stays closer and closer to the wall for increasing k_F.

The transverse wave function near the classical turning point can now be written as

$$\chi_1^{\infty+}(y) = C_1 \, \mathrm{Ai} \left(Ai_0 + \left(\frac{2k_F^2}{r_c} \right)^{1/3} y \right). \tag{6.62}$$

We will construct the full solution for the wave function by using the Airy function near the classical turning point and the WKB solution (which takes the quadratic potential into account) in the classically forbidden region. Before proceeding, we determine the prefactor C_1. Since the WKB solution is only used in describing the exponential tail for $y \gg y_z$, calculating C_1 with the wave function (6.62) of the linearized potential will only introduce a small error. Therefore, we insert Eq. (6.62)

into the flux normalization condition Eq. (6.9) and obtain

$$1 = \int_0^\infty \left(2k_{x,1}^{\infty+} + 2k_F \frac{y}{r_c}\right) \left[\chi_1^{\infty+}(y)\right]^2 \mathrm{d}y, \tag{6.63}$$

$$1 = \left(\frac{r_c}{2k_F^2}\right)^{1/3} \int_{Ai_0}^\infty \left[2k_{x,1}^{\infty+} + \frac{2k_F}{r_c}\left(\frac{r_c}{2k_F^2}\right)^{1/3}(z - Ai_0)\right] C_1^2 \,\mathrm{Ai}^2(z)\mathrm{d}z, \tag{6.64}$$

$$1 = 2^{2/3}(k_F r_c)^{1/3} C_1^2 \Bigg[\underbrace{\int_{Ai_0}^\infty \mathrm{Ai}^2(z)\mathrm{d}z}_{\gamma_0} + \frac{1}{2^{1/3}\left(k_F r_c\right)^{2/3}} \underbrace{\int_{Ai_0}^\infty z\,\mathrm{Ai}^2(z)\mathrm{d}z}_{\gamma_1}\Bigg], \tag{6.65}$$

where the two integrals in (6.65) just give constants which we call γ_0 and γ_1. We therefore find that

$$C_1 = \left[2^{2/3}(k_F r_c)^{1/3}\left(\gamma_0 + \frac{\gamma_1}{2^{1/3}\left(k_F r_c\right)^{2/3}}\right)\right]^{-1/2}, \tag{6.66}$$

which in the limit of large k_F simplifies to

$$C_1 \approx \left[2^{2/3}(k_F r_c)^{1/3}\gamma_0\right]^{-1/2}. \tag{6.67}$$

Since we need to evaluate the transverse wave function $\chi_1^{\infty+}$ at $y = w_L$, which is deep in the classically forbidden region, we proceed by connecting the Airy function (valid near the classical turning point) to the WKB solution (valid in the classically forbidden region). We write the WKB solution as

$$\chi_1^{\infty+}(y) \approx \frac{C_2}{\sqrt{\rho(y)}} \exp\left(-\int_{y_z}^{y} \rho(y')\mathrm{d}y'\right) \qquad y \gg y_z, \tag{6.68}$$

and from a short calculation (cf. Appendix A) we obtain that the two constants C_1 and C_2 are related by

$$C_2 = \left(\frac{2k_F^2}{r_c}\right)^{1/6} \frac{C_1}{2\sqrt{\pi}}. \tag{6.69}$$

For evaluating the integral in Eq. (6.68), we insert the explicit form of the potential. We take $y = w_L$ as the upper limit of integration since we need the wave

function at that point for evaluation of Eq. (6.55),

$$\begin{aligned} \rho(y) &= k_F\sqrt{V(y)/E_F}, \\ \rho(y) &= k_F\sqrt{2\frac{y-y_z}{r_c}+\left(\frac{y-y_z}{r_c}\right)^2}, \end{aligned} \tag{6.70}$$

$$\int_{y_z}^{w_L}\rho(y')\mathrm{d}y' = k_F r_c\int_0^z\sqrt{2z'+z'^2}\mathrm{d}z' \qquad z=\frac{w_L-y_z}{r_c}, \tag{6.71}$$

and evaluate the integral by expanding the integrand in powers of z'

$$\int_{y_z}^{w_L}\rho(y')\mathrm{d}y' = \sqrt{2}k_F r_c\int_0^z\left(z'^{1/2}+\frac{z'^{3/2}}{4}+O(z^{5/2})\right)\mathrm{d}z', \tag{6.72}$$

$$\int_{y_z}^{w_L}\rho(y')\mathrm{d}y' \approx \frac{2\sqrt{2}}{3}k_F r_c z^{3/2}\left(1+\frac{3}{20}z\right). \tag{6.73}$$

Inserting this into Eq. (6.68), we obtain

$$\chi_1^{\infty+}(w_L) \approx \frac{C_2}{\sqrt{\rho(w_L)}}\exp\left(-\frac{2\sqrt{2}}{3}k_F r_c\left(\frac{w_L-y_z}{r_c}\right)^{3/2}\left(1+\frac{3}{20}\frac{w_L-y_z}{r_c}\right)\right), \tag{6.74}$$

$$y_z = -\left(\frac{r_c}{2k_F^2}\right)^{1/3}Ai_0. \tag{6.75}$$

Since $y_z \ll r_c$ in the limit of large k_F, we rewrite this as

$$\chi_1^{\infty+}(w_L) \approx \frac{C_2}{\sqrt{\rho(w_L)}}\exp\left(-\frac{2\sqrt{2}}{3}k_F r_c\left(\frac{w_L}{r_c}\right)^{3/2}\left(1+\frac{3}{20}\frac{w_L}{r_c}\right)\left(1-\frac{y_z}{w_L}\right)^{3/2}\right), \tag{6.76}$$

where we have omitted the term

$$1-\frac{3}{20\left(1+\frac{3}{20}\frac{w_L}{r_c}\right)}\frac{y_z}{r_c} \approx 1, \tag{6.77}$$

which represents a small correction of higher order in inverse powers of k_F.

To get our almost final expression for ε_A, we insert Eq. (6.76) into Eq. (6.55) and obtain

$$\varepsilon_A = C_3\exp\left(-\frac{4\sqrt{2}}{3}k_F r_c\left(\frac{w_L}{r_c}\right)^{3/2}\left(1+\frac{3}{20}\frac{w_L}{r_c}\right)\left(1-\frac{y_z}{w_L}\right)^{3/2}\right), \tag{6.78a}$$

$$C_3 = \frac{C_2^2}{\rho(w_L)^2}\left(k_{x,1}^{\infty+}+\frac{k_F w_L}{r_c}\right). \tag{6.78b}$$

We insert ρ from Eq. (6.49), C_2 from Eq. (6.69) and then C_1 from Eq. (6.67) to determine C_3,

$$C_3 = \frac{(k_F r_c)^{-2/3}}{2^{1/3} 4\pi\gamma_0} \frac{k_{x,1}^{\infty+}/k_F + w_L/r_c}{2(w_L - y_z)/r_c + ((w_L - y_z)/r_c)^2}. \tag{6.79}$$

6.2.1 Localization length ξ in the quasi-classical limit

To obtain our final result for the localization length ξ in the quasi-classical limit of large k_F, we insert Eq. (6.79) and Eq. (6.78) into the expression Eq. (6.22) for the localization length ξ. To perform a true quasi-classical limit, we keep the cyclotron radius r_c constant, such that the classical dynamics is independent of k_F. This leads to

$$\frac{\xi}{l} \approx \frac{M}{4C_3} \exp[\ldots]. \tag{6.80}$$

We expand the prefactor $M/(4C_3)$ in powers of k_F for $k_F \to \infty$, keeping the first two terms in the expansion since they are of similar magnitude for the parameter values used, and finally obtain

$$\frac{\xi}{l} = \left(\alpha_1 \eta^{2/3} + \alpha_2\right) \exp\left[\alpha_3 \eta (1 - \alpha_4 \eta^{-2/3})^{3/2}\right], \tag{6.81}$$

where $\eta = k_F W/\pi$ and the dimensionless parameters α_1, α_2, α_3 are given by

$$\alpha_1 = 2^{1/3}\pi^{5/3} M\gamma_0 \frac{\Delta}{\zeta^{1/3}} \left(\frac{2 + \Delta/\zeta}{1 + \Delta/\zeta}\right), \tag{6.82a}$$

$$\alpha_2 = \pi A i_0 M\gamma_0 \left(1 + \frac{\zeta^2}{(\Delta + \zeta)^2}\right), \tag{6.82b}$$

$$\alpha_3 = \frac{4\sqrt{2}\pi}{3} \frac{\Delta^{3/2}}{\zeta^{1/2}} \left(1 + \frac{3}{20}\frac{\Delta}{\zeta}\right), \tag{6.82c}$$

$$\alpha_4 = -\frac{Ai_0}{2^{1/3}\pi^{2/3}} \frac{\zeta^{1/3}}{\Delta}, \tag{6.82d}$$

where we have introduced the dimensionless parameters $\Delta = w_L/W = 1 - (\delta_u/2W)$ and $\zeta = r_c/W$. As we predicted by general arguments about phase space and tunneling probabilities in the quasi-classical limit in section 5.2, we see an exponential increase of the localization length with $\eta \propto k_F$.

With our parameter values of $\Delta = 2/3$, $\zeta = 3$ and $M = 20$, and inserting the numerical values $Ai_0 \approx -2.33811$ and $\gamma_0 \approx 0.49170$, the three parameters have the following values:

$$\alpha_1 = 70.17, \tag{6.83a}$$

$$\alpha_2 = -120.59, \tag{6.83b}$$

$$\alpha_3 = 1.924, \tag{6.83c}$$

$$\alpha_4 = 1.872. \tag{6.83d}$$

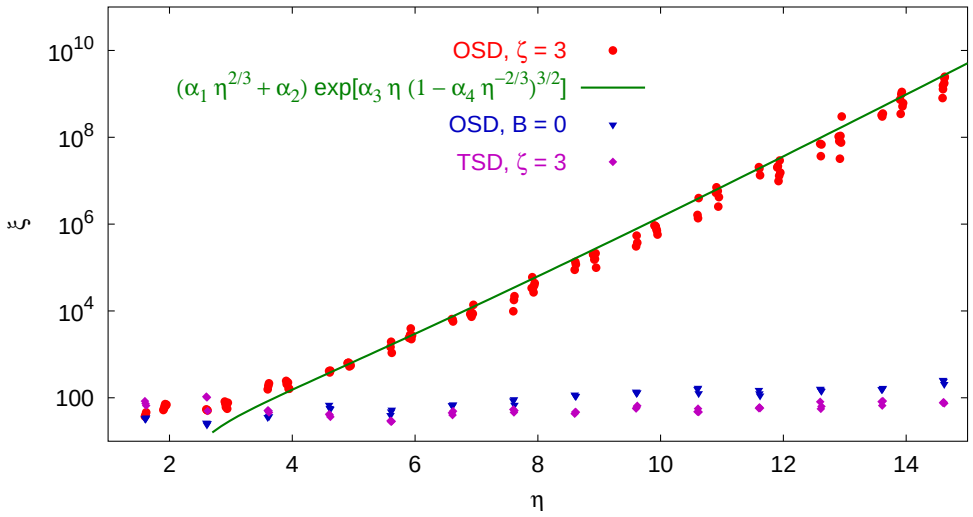

Figure 6.6: *Localization length ξ for a wire with one-sided surface disorder in a magnetic field, plotted against η. For comparison, ξ for wires with TSD and for OSD without a magnetic field are shown. The analytical result for ξ from Eq. (6.81) is also shown and reproduces the observed behavior very well.*

The agreement of the numerical results in section 5.2 with the present calculation is excellent, especially considering the numerous approximations made in the calculation. This was shown in Fig. 5.10, repeated here (Fig. 6.6) for clarity. We stress that no fit parameters were used.

6.2.2 Localization length ξ for high Fermi momentum k_F and constant magnetic field B

We can also perform the limit of $k_F \to \infty$ at constant magnetic field B instead of constant cyclotron radius $r_c = ck_F/B$. In that case, the limit does not correspond to a pure quantum-to-classical crossover, as the classical dynamics is not independent of k_F. To obtain dimensionless parameters, we introduce the magnetic length λ through $B/c = 1/\lambda^2$ and the dimensionless parameter $\Lambda = \lambda/W$. As above, we use $\Delta = w_L/W$ and obtain

$$\frac{\xi}{l} = \left(\beta_1 \eta^{1/3} + \beta_2\right) \exp(\beta_3 \eta^{1/2}(1 - \beta_4 \eta^{-1/3})^{3/2}), \tag{6.84}$$

with the dimensionless parameters β_1, β_2, β_3, β_4 given by

$$\beta_1 = (2\pi)^{4/3} M\gamma_0 \frac{\Delta}{\Lambda^{2/3}}, \tag{6.85a}$$

$$\beta_2 = 2\pi A i_0 M\gamma_0, \tag{6.85b}$$

$$\beta_3 = \frac{4\sqrt{2\pi}}{3} \frac{\Delta^{3/2}}{\Lambda}, \tag{6.85c}$$

$$\beta_4 = -\frac{Ai_0}{(2\pi)^{1/3}} \frac{\Lambda^{2/3}}{\Delta}, \tag{6.85d}$$

The leading factor in the exponent of Eq. (6.84) is the square root of the Fermi momentum k_F. As discussed in subsection 5.2.2, the square root enters because the relative size of the regular island in phase space shrinks when we keep the magnetic field strength B constant while increasing k_F.

As for the case of constant cyclotron radius, we find excellent agreement of the numerical result for ξ with the predicted behavior: An exponential increase of the localization length, but with the square root of k_F in the exponent. This was shown in Fig. 5.11, and is repeated here (Fig. 6.7) for clarity.

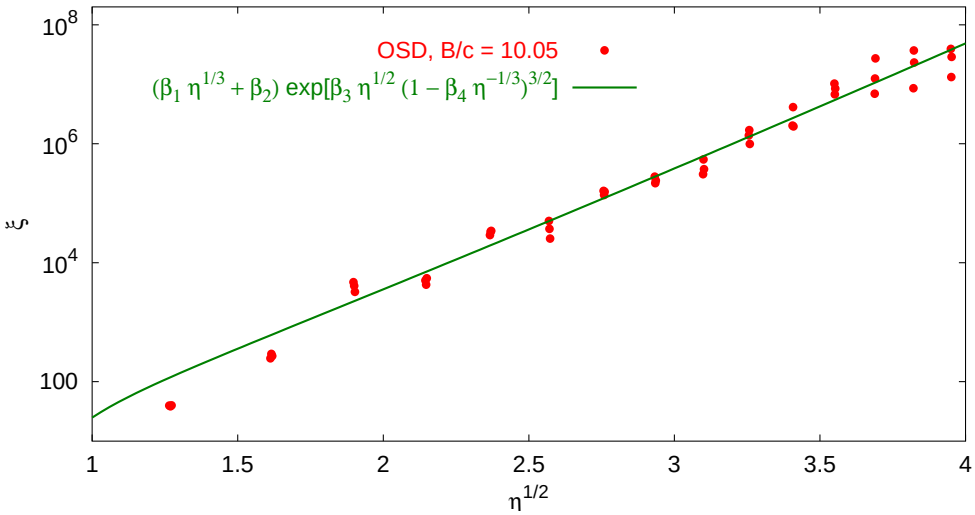

Figure 6.7: *ξ for a wire with one-sided surface disorder in a magnetic field, plotted against $\sqrt{\eta}$. In this figure, the magnetic field B is held constant. We also show the prediction Eq. (6.84) for ξ from the analytical calculation. The prediction reproduces the observed behaviour very well.*

It is worth listing the approximations used in our derivation of the above expressions (6.81) and (6.84). First, we neglected all non-direct paths for transmission

of the first mode into itself. We can estimate these paths to contribute on the same order of magnitude as the direct path. Including them would considerably complicate our derivation, but should only change the prefactors α_1, α_2 and β_1, β_2 in our result, since the order of the contribution is the same as that of the direct path.

Similarly, we neglected a term in our wave function matching that contains products of r_{m1} and an integral over the product of $\chi_m^{L-}(y)$ and $\chi_1^{R+}(y)$, where both r_{m1} and the integral can be shown to be of order $O(\sqrt{\varepsilon})$. This sum was also analyzed numerically by employing the implementation of the system of two leads of different width connected to each other and found to correspond to a correction of about 20% to the localization length ξ. Neglecting this term left us with an integral over the product of the first transverse modes in the left and right lead to determine ξ, which we evaluated by replacing the first mode in the wider lead by that of an infinitely wide lead and expressing the first mode in the narrower lead as a sum of the mode in the infinitely wide lead and a small correction.

We then employed a combined approach of linearizing the potential near the classical turning point and using a WKB approximation in the classically forbidden region to calculate the remaining integral. Finally, we expanded the obtained result for the case of high Fermi momentum k_F and constant cyclotron radius r_c [constant magnetic field B] to arrive at the simple expression (6.81) [(6.84)].

We have thus shown that in our system the existence of a regular island in phase space leads to a giant localization length in the limit of large Fermi momentum k_F, when the classical dynamics can be fully resolved by the quantum dynamics. In that case, the coupling between the regular island and the chaotic sea proceeds only by tunneling, which is exponentially suppressed in the quasi-classical limit. We are able to perform this limit by keeping the cyclotron radius constant, such that the classical dynamics stays unchanged as we increase the Fermi momentum.

Chapter 7

Summary and Outlook

Prediction is very difficult, especially about the future.
Niels Bohr

In this work we investigate electron transport in ballistic wires with surface disorder. Utilizing the Modular Recursive Green's Function Method, we develop an algorithm to simulate quantum transport up to extremely long wire lengths.

We place a particular emphasis on wires with one-sided surface disorder subject to a perpendicular magnetic field B. For this system, the classical phase space splits up into a regular island inhabited by skipping orbits and a chaotic sea. This mixed phase space induces diverging localization lengths in the quantum calculation if the quasi-classical limit of high Fermi momentum k_F is taken.

By employing the fact that the classical dynamics only depends on the cyclotron radius $r_c = ck_F/B$ and not on k_F or B separately, we are able to perform a true quasi-classical limit in which the localization length ξ, which corresponds to an inverse tunneling rate, increases exponentially with k_F. We additionally perform an analytical calculation to derive the localization length by calculating the transmission of the first mode through wave function matching. This calculation reproduces the scaling of the localization length without any adjustable parameters, although there is an error of order one in the absolute amplitude, which we can attribute to the approximations performed.

We explain the intermode coupling for modes on the regular island by chaos-assisted tunneling through a simple model that only utilizes the localization lengths ξ_m of the individual modes. These localization lengths correspond to the inverse tunneling rates off the island. Our model leads to a prediction for the values of the transmission probabilities T_{m1} from the first mode in the left lead to a mode m in the right lead that is found to be very accurate. The model employed for deriving these probabilities does not include any additional fit parameters apart from the localization lengths of the individual modes, which are determined independently.

A further topic that could be studied using the methods and algorithms pre-

sented here is the distribution of transmission eigenvalues. For example, deep in the localized regime, where the conductance is much smaller than one, $g \ll 1$, the distribution of the conductance should be log-normal, i.e. the distribution of the *logarithm* of the conductance should be Gaussian [11]. For shorter wires at the onset of localization, where the conductance is only slightly smaller than one, this distribution has been predicted to change to a one-sided log-normal distribution with a sharp cutoff above $g = 1$ [13, 69].

Another possible topic for further study could be the behavior of the modes that live in the chaotic sea, outside the regular island. In very recent work, this has been investigated classically [70] for a system similar to ours.

There is also the possibility of using not only rectangular modules to simulate wires with surface disorder. For example, a rectangle with a half-circle on top can be easily calculated using the MRGM. This could be an interesting alternative to the current system with only rectangular modules.

A further possibility would be to include bulk disorder into the system by adding random site energies in our tight-binding Hamiltonian. In this way, a crossover from exponentially large localization lengths to the RMT predictions for bulk disorder could be studied. This would also give the possibility to model the experimental situation of low but not completely vanishing bulk disorder. Another way of incorporating bulk disorder would be by the inclusion of hard point-like scatterers, which could be realized by setting the hopping potential from one module to the next to zero at some points.

Finally, our algorithms could be easily adapted to study the properties of a series of quantum point contacts, created by connecting a number of ballistic cavities to each other via point contacts, i.e. constrictions or shutters. Such systems have been investigated both experimentally and theoretically, with an emphasis on the study of *shot noise* [71].

Appendix A

Connection of WKB solution to the solution for the linearized potential

In this section we derive how we can smoothly connect the WKB solution for the classically forbidden region with the solution for the linearized potential near the classical turning point. We can do this generally without using the specific properties of our potential.

We write the Schrödinger equation for a 1-dimensional system with potential $V(y)$ as

$$\left(-\frac{\partial^2}{\partial y^2} + V(y)\right)\chi(y) = E\chi(y), \tag{A.1}$$

where we assume that the potential increases monotonously with y, such that there is some classical turning point y_z for which $V(y_z) = E$ and $V(y > y_z) > E$. The region $y > y_z$ is the classically forbidden region, where we can write the WKB solution as [67]

$$\chi_1^{\infty+}(y) \approx \frac{C_2}{\sqrt{\rho(y)}} \exp(-\kappa(y)) \qquad y \gg y_z, \tag{A.2}$$

$$\kappa(y) = \int_{y_z}^{y} \rho(y')\mathrm{d}y', \tag{A.3}$$

where $\rho(y) = \sqrt{2[V(y) - E]}$. Near the classical turning point y_z, where $\rho(y_z) = 0$, this WKB solution diverges. To obtain a solution in that region, we linearize the potential around y_z, such that

$$V(y) \approx V(y_z) + V'(y_z) \cdot (y - y_z). \tag{A.4}$$

Inserting this into the Schrödinger equation (A.1) and using $V(y_z) = E$, we obtain

$$\left(-\frac{\partial^2}{\partial y^2} + V'(y) \cdot (y - y_Z)\right) \chi(y) = 0, \tag{A.5}$$

which we can simplify by substituting

$$z = c \cdot (y - y_z), \tag{A.6}$$

$$c = (2V'(y_z))^{1/3}, \tag{A.7}$$

such that the Schrödinger equation becomes

$$\left(\frac{\partial^2}{\partial z^2} - z\right) \chi(z) = 0. \tag{A.8}$$

This has the two general solutions $\mathrm{Ai}(z)$, shown in Fig. 6.5, and $\mathrm{Bi}(z)$, which diverges for large z. In our case we only keep $\mathrm{Ai}(z)$ and write the solution near the classical turning point as

$$\chi(z) = C_1 \,\mathrm{Ai}(z). \tag{A.9}$$

To connect this with the WKB solution in the classically forbidden region, we use the asymptotic expansion of the Airy function $\mathrm{Ai}(z)$ for large z,

$$\mathrm{Ai}(z) \approx \frac{1}{2\sqrt{\pi} z^{1/4}} \exp\left(-\frac{2}{3} z^{3/2}\right) \qquad z \gg 0. \tag{A.10}$$

For $y > y_z$, we thus have two solutions for the wave function, the first coming from the linearization of the potential,

$$\chi^{\mathrm{lin}}(y) = \frac{C_1}{2\sqrt{\pi} z^{1/4}} \exp\left(-\frac{2}{3} z^{3/2}\right), \tag{A.11}$$

and the other from WKB,

$$\chi^{\mathrm{WKB}}(y) = \frac{C_2}{\sqrt{\rho(y)}} \exp(-\kappa(y)) \tag{A.12}$$

Close to the classical turning point, we can expand $\rho(y)$ as

$$\rho(y) \approx \sqrt{2V'(y_z)(y - y_z)} = b z^{1/2}, \tag{A.13}$$

and consequently,

$$\kappa(y) = \int_{y_z}^{y} \rho(y')\mathrm{d}y' \approx \int_{0}^{z} z'^{1/2}\mathrm{d}z' = \frac{2}{3} z^{3/2}. \tag{A.14}$$

Inserting the last two expressions into Eq. (A.12) and comparing to Eq. (A.11) shows that the two solutions agree for

$$C_2 = C_1 \cdot \frac{\sqrt{b}}{2\sqrt{\pi}}. \tag{A.15}$$

We use this result in Eq. (6.69), with

$$b = \left(\frac{2k_F^2}{r_c}\right)^{1/3} \tag{A.16}$$

for the specific system discussed in chapter 6.

Acknowledgements

No act of kindness, no matter how small, is ever wasted.
Aesop

Finally, I would like to thank all the people who helped and encouraged me while working on this thesis. A very special thanks is due to my co-advisor Dr. Stefan Rotter, who always found time to discuss any questions and served as an example of how to stay calm even in stressful times. Many thanks to my advisor Dr. Joachim Burgdörfer for many fruitful discussions, guidance and support. I would also like to thank Dr. Arnd Bäcker and Dr. Roland Ketzmerick, who proposed the project and provided many helpful ideas. I would especially like to thank Arnd for implementing the classical simulation of electron transport used to calculate the phase space pictures and Roland for inventing the model in subsection 5.2.4 and many insights regarding the analytical calculations.

Furthermore, I thank DI Florian Libisch for his help in understanding and optimizing the program code and his advice and help with many small things. I also thank DI Florian Aigner for fruitful discussions and for sharing his code for calculating Husimi distributions with me. Fig. 2.1 is also adapted from a figure provided by him.

I am grateful to all the members of our group at the Institute for Theoretical Physics for enjoyable coffee breaks and interesting discussions, and also for cultivating the habit of eating chocolate during the coffee breaks.

Last but certainly not least, I would like to thank my family and friends for always supporting me and encouraging me on my way. Without you I'm nothing.

Bibliography

[1] P. Sheng. *Introduction to Wave Scattering, Localization and Mesoscopic Phenomena*. Academic, New York (1995).

[2] P. A. Lee and T. V. Ramakrishnan. *Disordered electronic systems*. Rev. Mod. Phys. **57**, 287 (1985).

[3] M. Nieto-Vesperinas and J. C. Dainty (eds.). *Scattering in Volumes and Surfaces*. North-Holland, Amsterdam (1990).

[4] B. L. Altshuler, P. A. Lee, and R. A. Webb (eds.). *Mesoscopic Phenomena in Solids*. North-Holland, Amsterdam (1991).

[5] J. P. Fouque (ed.). *Diffuse Waves in Complex Media*, volume 531. NATO Advanced Studies Institute, Series C, Kluwer, Dordrecht (1999).

[6] P. W. Anderson. *Absence of Diffusion in Certain Random Lattices*. Phys. Rev. **109**, 1492 (1958).

[7] D. K. Ferry and S. M. Goodnick. *Transport in Nanostructures*. Cambridge University Press (1997).

[8] S. Datta. *Electronic Transport in Mesoscopic Systems*. Cambridge University Press (1995).

[9] J. H. Davies. *The Physics of Low-Dimensional Semiconductors*. Cambridge University Press, Cambridge (1998).

[10] K. v. Klitzing, G. Dorda, and M. Pepper. *New method for high-accuracy determination of the fine-structure constant based on quantized Hall resistance*. Phys. Rev. Lett. **45**, 494 (1980).

[11] C. Beenakker. *Random-matrix theory of quantum transport*. Reviews of Modern Physics **69**, 731 (1997).

[12] J. Sánchez-Gil, V. Freilikher, I. Yurkevich, and A. Maradudin. *Coexistence of Ballistic Transport, Diffusion, and Localization in Surface Disordered Waveguides*. Phys. Rev. Lett. **80**, 948 (1998).

[13] A. Garcia-Martin and J. J. Saenz. *Universal Conductance Distributions in the Crossover between Diffusive and Localization Regimes.* Phys. Rev. Lett. **87**, 116603 (2001).

[14] J. Sánchez-Gil, V. Freilikher, A. Maradudin, and I. Yurkevich. *Reflection and transmission of waves in surface-disordered waveguides.* Phys. Rev. B **59**, 5915 (1999).

[15] M. Leadbeater, V. I. Falko, and C. J. Lambert. *Lévy Flights in Quantum Transport in Quasiballistic Wires.* Phys. Rev. Lett. **81**, 1274 (1998).

[16] F. M. Izrailev, J. A. Mendez-Bermudez, and G. A. Luna-Acosta. *Ballistic localization in quasi-one-dimensional waveguides with rough surfaces.* Phys. Rev. E **68**, 066201 (2003).

[17] E. I. Chaikina, S. Stepanov, A. G. Navarrete, E. R. Mendez, and T. A. Leskova. *Formation of angular power profile via ballistic light transport in multimode optical fibers with corrugated surfaces.* Phys. Rev. B **71**, 085419 (2005).

[18] H. Schanz and M. Prusty. *Directed chaos in a billiard chain with transversal magnetic field.* J. Phys. A **38**, 10085 (2005).

[19] M. J. Davis and E. J. Heller. *Quantum dynamical tunnelling in bound states.* J. Chem. Phys. **75**, 246 (1981).

[20] E. Ott and T. Tél. *Chaotic scattering: An introduction.* Chaos: An Interdisciplinary Journal of Nonlinear Science **3**, 417 (1993).

[21] H. Schanz, M. F. Otto, R. Ketzmerick, and T. Dittrich. *Classical and quantum hamiltonian ratchets.* Phys. Rev. Lett. **87**, 070601 (2001).

[22] H. Schanz, T. Dittrich, and R. Ketzmerick. *Directed chaotic transport in Hamiltonian ratchets.* Phys. Rev. E **71**, 026228 (2005).

[23] J. D. Hanson, E. Ott, and T. M. Antonsen. *Influence of finite wavelength on the quantum kicked rotator in the semiclassical regime.* Phys. Rev. A **29**, 819 (1984).

[24] V. A. Podolskiy and E. E. Narimanov. *Semiclassical description of chaos-assisted tunneling.* Phys. Rev. Lett. **91**, 263601 (2003).

[25] C. Eltschka and P. Schlagheck. *Resonance- and Chaos-Assisted Tunneling in Mixed Regular-Chaotic Systems.* Phys. Rev. Lett. **94**, 014101 (2005).

[26] O. Brodier, P. Schlagheck, and D. Ullmo. *Resonance-Assisted Tunneling.* Ann. Phys. **300**, 88 (2002).

[27] M. Sheinman, S. Fishman, I. Guarneri, and L. Rebuzzini. *Decay of Quantum Accelerator Modes.* arXiv.org:quant-ph/0512072 (2005).

[28] L. Hufnagel, R. Ketzmerick, M.-F. Otto, and H. Schanz. *Eigenstates Ignoring Regular and Chaotic Phase-Space Structures.* Physical Review Letters **89**, 154101 (2002).

[29] S. Rotter, J.-Z. Tang, L. Wirtz, J. Trost, and J. Burgdörfer. *Modular recursive Green's function method for ballistic quantum transport.* Phys. Rev. B **62**, 1950 (2000).

[30] S. Rotter, B. Weingartner, N. Rohringer, and J. Burgdörfer. *Ballistic quantum transport at high energies and high magnetic fields.* Phys. Rev. B **68**, 165302 (2003).

[31] L. Onsager. *Reciprocal Relations in Irreversible Processes. II.* Phys. Rev. **38**, 2265 (1931).

[32] H. B. G. Casimir. *On Onsager's Principle of Microscopic Reversibility.* Reviews of Modern Physics **17**, 343 (1945).

[33] M. Büttiker. *Four-Terminal Phase-Coherent Conductance.* Phys. Rev. Lett. **57**, 1761 (1986).

[34] R. Landauer. *Spatial Variation of Currents and Fields Due to Localized Scatterers in Metallic Conduction.* IBM J. Res. Develop. **1**, 233 (1957).

[35] D. S. Fisher and P. A. Lee. *Relation between conductivity and transmission matrix.* Phys. Rev. B **23**, 6851 (1981).

[36] H. U. Baranger and A. D. Stone. *Electrical linear-response theory in an arbitrary magnetic field: A new Fermi-surface formation.* Phys. Rev. B **40**, 8169 (1989).

[37] L. Kouwenhoven and C. Marcus. *Quantum Dots.* Physics World p. 35 (June 1998).

[38] P. W. Anderson, D. J. Thouless, E. Abrahams, and D. S. Fisher. *New method for a scaling theory of localization.* Phys. Rev. B **22**, 3519 (1980).

[39] P. W. Anderson. *New method for scaling theory of localization. II. Multichannel theory of a "wire" and possible extension to higher dimensionality.* Phys. Rev. B **23**, 4828 (1981).

[40] E. Abrahams, P. W. Anderson, D. C. Licciardello, and T. V. Ramakrishnan. *Scaling theory of localization: Absence of quantum diffusion in two dimensions.* Phys. Rev. Lett. **42**, 673 (1979).

[41] T. Guhr, A. Müller-Groeling, and H. A. Weidenmüller. *Random-matrix theories in quantum physics: common concepts.* Physics Reports **299**, 189 (1998).

[42] A. D. Mirlin. *Statistics of energy levels and eigenfunctions in disordered systems.* Physics Reports **326**, 259 (2000).

[43] C. E. Porter. *Statistical Theories of Spectra: Fluctuations.* Academic Press, New York (1965).

[44] T. Ericson. *Fluctuations of Nuclear Cross Sections in the "Continuum" Region.* Phys. Rev. Lett. **5**, 430 (1960).

[45] R. de Picciotto, H. L. Stormer, L. N. Pfeiffer, K. W. Baldwin, and K. W. West. *Four-terminal resistance of a ballistic quantum wire.* Nature **411**, 51 (2001).

[46] A. García-Martín, J. A. Torres, J. J. Sáenz, and M. Nieto-Vesperinas. *Transition from diffusive to localized regimes in surface corrugated optical waveguides.* App. Phys. Lett. **71**, 1912 (1997).

[47] A. García-Martín, J. J. Sáenz, and M. Nieto-Vesperinas. *Spatial Field Distributions in the Transition from Ballistic to Diffusive Transport in Randomly Corrugated Waveguides.* Phys. Rev. Lett. **84**, 3578 (2000).

[48] N. Zhu, H. Guo, and R. Harris. *Destruction of Conductance Fluctuations in a Dirty Wire.* Phys. Rev. Lett. **77**, 1825 (1996).

[49] A. García-Martín, M. Governale, and P. Wölfle. *Magnetic field effects on the transport properties of one-sided rough wires.* Phys. Rev. B **66**, 233307 (2002).

[50] F. M. Peeters. *Quantum Hall Resistance in the Quasi-One-Dimensional Electron Gas.* Phys. Rev. Lett. **61**, 589 (1988).

[51] R. L. Schult, H. W. Wyld, and D. G. Ravenhall. *Quantum Hall effect and general narrow-wire circuits.* Phys. Rev. B **41**, 12760 (1990).

[52] R. E. Peierls. *Zur Theorie des Diamagnetismus von Leitungselektronen.* Zeits. f. Physik **80**, 763 (1933).

[53] T. Ando. *Quantum point contacts in magnetic fields.* Phys. Rev. B **44**, 8017 (1991).

[54] I. V. Zozoulenko, F. A. Maaø and E. H. Hauge. *Coherent magnetotransport in confined arrays of antidots. I. Dispersion relations and current densities.* Phys. Rev. B **53**, 7975 (1996).

[55] I. V. Zozoulenko, F. A. Maaø and E. H. Hauge. *Coherent magnetotransport in confined arrays of antidots. II. Two-terminal conductance.* Phys. Rev. B **53**, 7987 (1996).

[56] I. V. Zozoulenko, F. A. Maaø and E. H. Hauge. *Coherent magnetotransport in confined arrays of antidots. III. Origin of the commensurate peaks.* Phys. Rev. B **56**, 4710 (1997).

[57] E. N. Economou. *Green's Functions in Quantum Physics.* Springer Berlin (1979).

[58] J. Skjånes, E. H. Hauge, and G. Schön. *Magnetotransport in a two-dimensional tight-binding model.* Phys. Rev. B **50**, 8636 (1994).

[59] W. H. Press, S. A. Teukolsky, W. T. Vetterling, and B. P. Flannery. *Numerical Recipes in Fortran 77.* Cambridge University Press (1986).

[60] N. J. Higham and H.-M. Kim. *Numerical analysis of a quadratic matrix equation.* IMA Journal of Numerical Analysis **20**, 499 (2000).

[61] A. Bäcker, A. Manze, B. Huckestein, and R. Ketzmerick. *Isolated resonances in conductance fluctuations and hierarchical states.* Phys. Rev. E **66**, 016211 (2002).

[62] A. Bäcker, S. Fürstberger, and R. Schubert. *Poincaré Husimi representation of eigenstates in quantum billiards.* Phys. Rev. E **70**, 036204 (2004).

[63] C. Jung. *Poincaré map for scattering states.* J. Phys. A **19**, 1345 (1986).

[64] R. Blümel and U. Smilansky. *Random-matrix description of chaotic scattering: Semiclassical approach.* Phys. Rev. Lett. **64**, 241 (1990).

[65] C. W. J. Beenakker and H. van Houten. *Quenching of the Hall effect.* Phys. Rev. Lett. **60**, 2406 (1988).

[66] A. Messiah. *Quantum Mechanics.* Dover Publications (2000).

[67] L. D. Landau and E. M. Lifshitz. *Course of Theoretical Physics, Vol.3 : Quantum Mechanics (Non-Relativistic Theory).* Butterworth-Heinemann (1997).

[68] R. E. Langer. *On the Connection Formulas and the Solutions of the Wave Equation.* Phys. Rev. **51**, 669 (1937).

[69] K. A. Muttalib and P. Wölfle. *"One-Sided" Log-Normal Distribution of Conductances for a Disordered Quantum Wire.* Phys. Rev. Lett. **83**, 3013 (1999).

[70] M. Prusty and H. Schanz. *Signature of Directed Chaos in the Conductance of a Nanowire.* Phys. Rev. Lett. **96**, 130601 (2006).

[71] S. Oberholzer, E. V. Sukhorukov, C. Strunk, and C. Schonenberger. *Shot noise of series quantum point contacts intercalating chaotic cavities.* Phys. Rev. B **66**, 233304 (2002).